Abstract of "Numerical Methods for Multi-Scale Modeling of Non-Newtonian Flows," by Vasileios Symeonidis, Ph.D., Brown University, May 2006

This work presents numerical methods for the simulation of Non-Newtonian fluids in the continuum as well as the mesoscopic level. The former is achieved with Direct Numerical Simulation (DNS) spectral h/p methods, while the latter employs the Dissipative Particle Dynamics (DPD) technique. Physical results are also presented as a motivation for a clear understanding of the underlying numerical approaches.

The macroscopic simulations employ two non-Newtonian models, namely the Reiner-Rivlin (RR) and the viscoelastic FENE-P model.

- A spectral viscosity method defined by two parameters ε, M is used to stabilize the FENE-P conformation tensor $\mathbf{c}$. Convergence studies are presented for different combinations of these parameters. Two boundary conditions for the tensor $\mathbf{c}$ are also investigated.
- Agreement is achieved with other works for Stokes flow of a two-dimensional cylinder in a channel. Comparison of the axial normal stress and drag coefficient on the cylinder is presented. Further, similar results from unsteady two- and three-dimensional turbulent flows past a flat plate in a channel are shown.
- The RR problem is formulated for nearly incompressible flows, with the introduction of a mathematically equivalent tensor formulation. A spectral viscosity method and polynomial over-integration are studied. Convergence studies, including a three-dimensional channel flow with a parallel slot, investigate numerical problems arising from elemental boundaries and sharp corners.
- The round hole pressure problem is presented for Newtonian and RR fluids in geometries with different hole sizes. Comparison with experimental data is made for the Newtonian case. The flaw in the experimental assumptions of undisturbed pressure opposite the hole is revealed, while good agreement with the data is shown. The Higashitani-Pritchard kinematical theory for RR fluids is recovered for round holes and an approximate formula for the RR Stokes hole pressure is presented.

The mesoscopic simulations assume bead-spring representations of polymer chains and investigate different integrating schemes of the DPD equations and different intra-polymer force combinations.

- A novel family of time-staggered integrators is presented, taking advantage of the time-scale disparity between polymer-solvent and solvent-solvent interactions. Convergence tests for relaxation parameters for the velocity-Verlet and Lowe's schemes are presented.
- Wormlike chains simulating $\lambda-$DNA molecules subject to constant shear are studied, and direct comparison with Brownian Dynamics and experimental results is made. The effect of the number of beads per chain is examined through the extension autocorrelation function.
- The Schmidt number (Sc) for each numerical scheme is investigated and the dependence on the scheme's parameters is shown. Re-visiting the wormlike chain problem under shear, we recover a better agreement with the experimental data through proper adjustment of Sc.

Numerical Methods for Multi-Scale Modeling of Non-Newtonian Flows

by

Vasileios Symeonidis

Sc.M. in Applied Mathematics, Brown University, 2001
M.Math. in Mathematics, University of Oxford, 1999

Thesis

Submitted in partial fulfillment of the requirements for
the Degree of Doctor of Philosophy
in the Division of Applied Mathematics at Brown University

May 2006

This dissertation by Vasileios Symeonidis is accepted in its present form by
the Division of Applied Mathematics as satisfying the
dissertation requirement for the degree of
Doctor of Philosophy

Date____________________ ______________________________________

Professor George Em Karniadakis, Director

Date____________________ ______________________________________

Professor Bruce Caswell, Co-Director

Recommended to the Graduate Council

Date____________________ ______________________________________

Professor Robert A. Pelcovits, Dissertation Reader

Date____________________ ______________________________________

Professor Robert G. Owens, Dissertation Reader

Approved by the Graduate Council

Date____________________ ______________________________________

Sheila Bonde
Dean of the Graduate School

The Vita of Vasileios Symeonidis

Vasileios Symeonidis was born on November 9^{th}, 1976, in Athens, Greece. He graduated from Athens College (the Hellenic-American Educational Foundation) with a high-school diploma in 1995. He pursued his undergraduate education at the University of Oxford, United Kingdom, as a member of St.John's College. Having fulfilled the Part I (1998) and Part II (1999) requirements of the final honor school, he earned a M.Math. in Mathematics in 1999. In August 1999 he joined the Division of Applied Mathematics at Brown University. He earned a Sc.M. in Applied Mathematics in 2001.

Education

Ph.D., Brown University, U.S.A., 2005

Sc.M., Brown University, U.S.A., 2001

M.Math., University of Oxford, U.K., 1999

Awards and Distinctions

- Keen Fellowship, Brown University, Semester I, 2004-2005
- The Stella Dafermos Award, Division of Applied Mathematics, Brown University, 2005
- Distinction in British G.C.E. A-Level examinations with two special papers in advanced mathematics and physics, 1994

Patent

G.E. Karniadakis, K. Breuer, V. Symeonidis, *"Method and apparatus for reducing turbulent drag"*, U.S. Patent 6,520,455 (February 18, 2003).

Peer-Reviewed Journal Publications

1. V. Symeonidis, G.E. Karniadakis, B. Caswell, *"Simulation of λ-phage DNA in microchannels using Dissipative Particle Dynamics"*, Bulletin of the Polish Academy of Sciences (accepted, 2005).

2. V. Symeonidis, G.E. Karniadakis, *"A family of time-staggered schemes for integrating hybrid DPD models for polymers: Algorithms and applications"*, Journal of Computational Physics (submitted, 2005).

3. V. Symeonidis, B. Caswell, *"The Limiting Hole Pressure in Three Dimensions"*, Journal of Non-Newtonian Fluid Mechanics (submitted, 2005).

4. V. Symeonidis, G.E. Karniadakis, B. Caswell, *"Dissipative Particle Dynamics Simulations of Polymer Chains: Scaling Laws and Shearing Response Compared to DNA Experiments"*, Virtual Journal of Biological Physics Research, v.10, issue 4 (15 August 2005).

5. V. Symeonidis, G.E. Karniadakis, B. Caswell, *"Dissipative Particle Dynamics Simulations of Polymer Chains: Scaling Laws and Shearing Response Compared to DNA Experiments"*, Physical Review Letters, v.95, issue 7, p. 076001 (12 August 2005).

6. V. Symeonidis, G.E. Karniadakis, B. Caswell, *"A seamless approach to multiscale simulation of complex fluids"*, IEEE Computing in Science and Engineering, v.7, issue 3, pp. 39-46 (May/June 2005).

7. X. Ma, V. Symeonidis and G.E. Karniadakis, *"A spectral vanishing viscosity method for stabilizing viscoelastic flows"*, Journal of non-Newtonian Fluid Mechanics, v.115, pp.125-155 (2003).

8. Y. Du, V. Symeonidis, G.E. Karniadakis, *"Drag reduction in wall-bounded turbulence via a transverse traveling wave"*, Journal of Fluid Mechanics, v.457, pp.1-34 (2002).

Conference Presentations

1. 14^{th} International Workshop on Numerical Methods for non-Newtonian Flows, *"The hole pressure in 3 dimensions"* (June 12-15, Santa Fe, NM, 2005).

2. 14^{th} International Workshop on Numerical Methods for non-Newtonian Flows, *"Scaling laws for polymers using mesoscopic simulations"* (June 12-15, Santa Fe, NM, 2005).

3. 76^{th} Annual Meeting of the Society of Rheology, *"Slow flow hole pressure for a tube on one wall of a plane channel"* (February 13-17, 2005, Lubbock, TX, 2005).

4. 76^{th} Annual Meeting of the Society of Rheology, *"Scaling laws for polymers using mesoscopic simulations"* (February 13-17, 2005, Lubbock, TX, 2005).

5. American Institute of Chemical Engineers, *"The hole pressure due to a tube on one wall of a plane channel"* (Annual Meeting, November 7-12, Austin, TX, 2004).

6. Transport Phenomena in Micro and Nano-devices, *"Stochastic MD simulations of complex fluids in microdomains"* (October 17-21, Kona Coast, Island of Hawaii, HI, 2004).

7. 13^{th} International Conference on the Discrete Simulation of Fluid Dynamics, *"Stochastic MD simulations of complex fluids in microdomains"* (August 16-20, Cambridge, MA, 2004).

8. 6^{th} International Conference On Spectral and High Order Methods (ICOSAHOM) 2004, *"Stabilization methods for non-Newtonian models in complex geometries"* (June 21-25, Providence, RI, 2004).

9. 7^{th} U.S. National Congress on Computational Mechanics, *"A spectral vanishing viscosity method for stabilizing viscoelastic flows"* (July 28-30, Albuquerque, NM, 2003).

10. 13^{th} International Workshop on Numerical Methods for non-Newtonian Flows, *"A spectral vanishing viscosity method for stabilizing viscoelastic flows"* (June 4-7, EPFL Lausanne, Switzerland, 2003).

11. 55^{th} Annual Meeting, Division of Fluid Dynamics, American Physical Society, *"A new method for stabilizing non-Newtonian flows"* (November 24-26, Dallas, TX, 2002).

12. 53$^{\text{rd}}$ Annual Meeting, Division of Fluid Dynamics, American Physical Society, *"Turbulent drag reduction by traveling waves"* (November 19-21, Washington, DC, 2000).

Seminar Talk

1. Technische Universität Dresden, Center for High Performance Computing / Inst. of Aviation and Astronautics Technology, *"Electromagnetic turbulence control using traveling waves and oscillations"* (June 10, Dresden, Germany, 2003).

Training Workshops Attended

1. Pittsburgh Supercomputing Center, *"New Methods for Developing Peta-scalable Codes"* (May 3-4, Pittsburgh, PA, 2004).

2. Pointwise, Inc, *"Gridgen User Group Meeting"* (April 5-6, Fort Worth, TX, 2004).

To my parents, $E\lambda\acute{\epsilon}\nu\eta$ and $\Theta\epsilon\acute{o}\phi\iota\lambda o\varsigma$,

my sister, $E\upsilon\gamma\epsilon\nu\acute{\iota}\alpha$,

and my grandmother, $E\acute{\upsilon}\eta$.

Acknowledgments

It is a great pleasure for me to begin this short personal preface by thanking my primary dissertation supervisor, George Karniadakis. George has provided me with constant help, advice and motivation during my graduate student life here at Brown. I feel privileged for being given the opportunity to work and interact with him and his research group, and gain a fraction of his tremendous insight in many areas of mathematics, numerical analysis, physics and engineering. He contributed in major ways in my present scientific maturity, as an advisor but also as a close friend. I really hope we preserve this sincere and strong friendship in the future.

I also feel honored that I had the chance to work with Bruce Caswell, my other dissertation supervisor. For the last three years of my doctoral work he has been constantly by my side, giving me expert advice on academic and non-academic matters and providing me with his vast numerical and physical experience in numerous areas of engineering and physics. I owe him a lot for trusting me with his time and knowledge, and I hope that time will bring us closer in research and in life.

I would like to thank Robert Owens, not only for being in my thesis committee but also for many helpful discussions during meetings and conferences; he has been a great colleague. I also feel the need to thank Robert Pelcovits for agreeing to be a reader for my dissertation and devote time for suggestions, comments and corrections. In the Division of Applied Mathematics, here at Brown, I have also had the pleasure to meet and interact with Constantine Dafermos. I want to thank him for being there when I needed someone to talk to, and for being such an excellent example of an academic and scholar for all of us younger scientists. Jan Hesthaven deserves a big "thank you" as well.

I would not have studied mathematics or embarked on a Ph.D. program if it wasn't for my high school professor and friend, Alexandros Fourikis. I owe all of the enthusiasm for the field to him; he was the most inspiring professor in my high school years in many aspects. He was the first to show me how to think of a problem mathematically and organize my thoughts to work out the solution; most of all he showed me that mathematics can be part of life. I will never forget the numerous times I bothered him over the phone, late in the evening, seeking a hint for exercises I could not easily solve. I will always be grateful to him.

Words are too small to express the gratitude I feel towards my Brown and Providence friends. I feel fortunate for having co-existed with so many spectacular people that completely changed my character and made me what I am today. I thank "$\delta\epsilon\ \tau\sigma\iota\phi$" Katsoulis for being nothing less than a true friend, Kotis for being often crazy but always right and Elsa for being a second mother but also a first class friend at the same time. Dimitris, Socrates, Panagiotis, Vergad and Aris formed "the gang" of close friends that helped me in various circumstances and made me feel at home. I was destined to start and end my graduate life with my friends Harsh and the Dude, while other close friends like Polina, Angelika, Christina and Frederic left earlier but will always be in my heart. George Karamanos showed me the ropes from my first day here at Brown and I am grateful to him. I will always value my friendship with Mohan and admire Ruta, although they are both far away; I hope we meet again soon. I am also grateful that Ryan, Ammar, Aine and Amanda let me in their lives and were there whenever I needed them. I thank Mary Tsangarakis and Christopher for their amazing friendship and mageiritsa and Dimitris Livanios for being the best combination of friend and mentor. I also want to thank Constantinos and Asimina for their help, support and advice; they deserve the best and I am truly lucky to be one of their friends. As far as Elias and "The Jesus" George are concerned, I hope they make their advisor proud.

Although I have been away from home for exactly ten years now (nearly one third of my life and half of my productive life!), some friends in Greece have always been and will always be my "alter ego". Raphael and Orestes, my closest friends from high school, have helped me and supported me on various occasions and I thank them for it. Panos has proved to be the brother

I never had; he has always been supportive of my decisions but was there when I needed some of his street-wise advice. I cannot imagine my life without him. I am also grateful to Miltos, who I met in Oxford so randomly but has been one of my best and most valued friends ever since. I thank Costianna for listening to me when I most needed it, Myrto for our sunny and relaxing vacation conversations, Patsas and Costas for nights out all over Athens, Dorothy and Simos for complementing the Oxonian crazy company, Leda for adding an erudite Cantab-touch in my life, Chryssos for our long friendship, Anastasia and Thalia for their constant in-and-out-of-my-life friendship, and Ted and Stag for crazy souvlaki references in summertime. I would not have been a complete Oxonian without my lovely fellow Oxonian mathmo and non-mathmo mates Emma, Neil, Claire, Liz, Ian, Simon and Simeon (yes, I am doing maaars again!).

I am also grateful to my fellow CRUNCH group members for a great research environment. I will miss my good friends Dong Liu and Didi. I found great help in the faces of Suchuan Dong, Xia Ma, Mike Kirby and Dongbin Xiu. Good luck to Dmitry if he continues my project. I hope all of my fellow CRUNCH-ers succeed in their future plans. Charles Henoch will be one of the colleagues I will also miss. Of course, my thesis work would not have been possible without the expert help of our computer wizards Melih, Sam and Jie. Madeline, Laura and Rose also deserve a big "thanks" for their constant support. Also, I thank Jean for helping me many times with bureaucratic problems and for being such a pleasant departmental presence.

Last, but certainly not least, I am dedicating this dissertation and all the hard work I have put in it during the past six years to my lovely parents, *Ελένη* and *Θεόφιλος* who have been constantly helping, advising and supporting me, my sister *Ευγενία* who has been a great example for me since I was born, and, of course, my grandmother, *Εύη*, for being the most inspiring person in my life.

The author would like to acknowledge the following grant numbers, whose support has made this work possible:

- ONR: N00014-04-1-0007
- DOE: DE-FG02-95ER25239
- NSF/ITR: EIA-01218142
- NSF/ITR: CCR-0086065
- DARPA/ONR: N00014-01-1-0177
- ONR: N00014-95-1-0256

Contents

List of Tables

List of Figures

Chapter 1

Introduction

1.1 Non-Newtonian fluids

Most common fluids (both liquids and gases) around us can be classified as *Newtonian fluids*. Gases, low-molecular weight liquids, salted and unsalted water, most motor and mineral oils, high viscosity fuel, gasoline, kerosene are some examples. Such fluids are characterized by a linear dependence of shear stress on shear rate. In order to visualize this dependence, we consider the schematic unidirectional shear flow shown in Figure 1.1. In this case, the shear rate $\dot{\gamma}$ can be expressed as the velocity gradient in the $y-$direction (the direction perpendicular to the shearing). The shear stress τ_{xy} is then

$$\tau_{xy} = \sigma = \mu \left(\frac{dV_x}{dy} \right) = \mu \dot{\gamma} \tag{1.1}$$

The slope μ is constant and is often referred to as the Newtonian viscosity. It completely characterizes the behavior of the fluid and is (by definition) independent of the shear rate $\dot{\gamma}$ or stress τ_{xy}, although it may vary according to temperature and pressure. In short, a Newtonian fluid is defined by the equation $\mu = \frac{\sigma}{\dot{\gamma}}$.

A *non-Newtonian fluid* is one whose flow curve (shear stress versus shear rate) is either non-linear or does not pass through the origin. Examples of such fluids abound, with egg white,

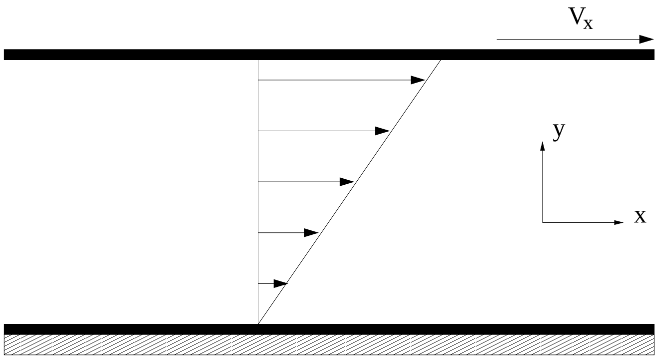

Figure 1.1: Unidirectional shear flow.

printer ink, toothpaste, the "bouncing putty" (flows at low stretch rates but bounces at high ones) being popular ones. Blood is a good example of a liquid that can exhibit both Newtonian and non-Newtonian behavior, according to its surroundings. In small branches and capillaries and at very low shear rates it behaves in a non-Newtonian fashion [8, 9, 10], while in most arteries the viscosity can be considered constant, for all practical purposes, equal to $\approx 4cP$. Clearly, there are numerous possibilities of a non-linear flow curve. In general, we can crudely classify such fluids into

1. **Generalized Newtonian Fluids**: Governed by $\dot{\gamma} = f(\sigma)$, they are fluids for which the shear rate at any point/instant is determined by the shear stress at that particular point/instant. Typical example is the power-law fluid, governed by $\sigma = k\dot{\gamma}^n$.

2. **Time-Dependent Fluids**: The shear stress and the shear rate are also a function of the duration of the shearing.

3. **Viscoelastic Fluids**: Fluids that store and recover shear energy, they usually contain a high fraction of substances with high molecular weight. They exhibit characteristics of both ideal fluids and elastic solids.

For non-Newtonian fluids, it is convenient to define the *apparent viscosity* as the ratio of shear stress, σ, to shear rate, $\dot{\gamma}$. Hence, the apparent viscosity μ_{app} can, in general, be expressed as the non-constant function $\mu_{\text{app}} = \frac{\sigma}{\dot{\gamma}} = f(\sigma, \dot{\gamma}, t)$. Another useful categorization of non-Newtonian fluids deals with cases in which the viscosity decreases with shear rate (*shear-thinning* or *pseu-*

doplastic fluids), the viscosity increases with shear rate (*shear-thickening* or *dilatant* fluids), the viscosity decreases with the duration of applied shear (*thixotropic* fluids), and the viscosity increases with the duration of applied shear (*rheopectic* or *negatively thixotropic* fluids).

Modeling of several non-Newtonian flows consists of constructing constitutive equations for the evolution of the polymeric part of the stress, $\mathbf{s}$. Such equations may involve time derivatives, integrals and stress/strain tensors. A constitutive equation always contains at least one time constant λ in the form $\mathbf{s} + \lambda\overset{\triangledown}{\mathbf{s}} = [\ldots]$, which gives rise to two convenient non-dimensional numbers, the Deborah number $De = \frac{\lambda}{T}$, and the Weissenberg number $We = \lambda\dot{\gamma}$. Here, T can be a typical time-scale of the flow and $\dot{\gamma}$ a typical shear rate; notation is used interchangeably, depending on the problem. The symbol $\overset{\triangledown}{[\ldots]}$ in this case denotes the *upper-convective derivative*. Examples of fluid models defined by such constitutive equations include the Maxwell, Oldroyd-B and the FENE-P models [11, 12, 13].

Since a large portion of Part I of this dissertation deals with the viscoelastic FENE-P model, it is useful to isolate three of the most important properties specific to this model: (i) It is shear-thinning. (ii) It exhibits normal stress differences: polymers can exert additional forces in all directions when they are being stretched. (iii) It exhibits stress relaxation: the force exerted by the viscoelastic material under sudden and fixed stretching rises sharply and then decreases with a characteristic relaxation time.

In addition to macroscopic non-Newtonian models, the molecular understanding of dilute solutions of flexible polymers has been in the spotlight since the late 1980s. Larson [14] recently summarized such efforts, focusing on the rheology of such solutions, the description of several bead-spring polymer representations, computations using Brownian Dynamics simulations, and experimental results from flows involving $\lambda-$phage DNA molecules (see Figure 1.2). Such efforts are essential in order to understand the atomistic behavior of complex fluids with internal microstructure, and apply some closures to obtain constitutive equations from kinetic models [15, 16, 17, 18, 19, 20].

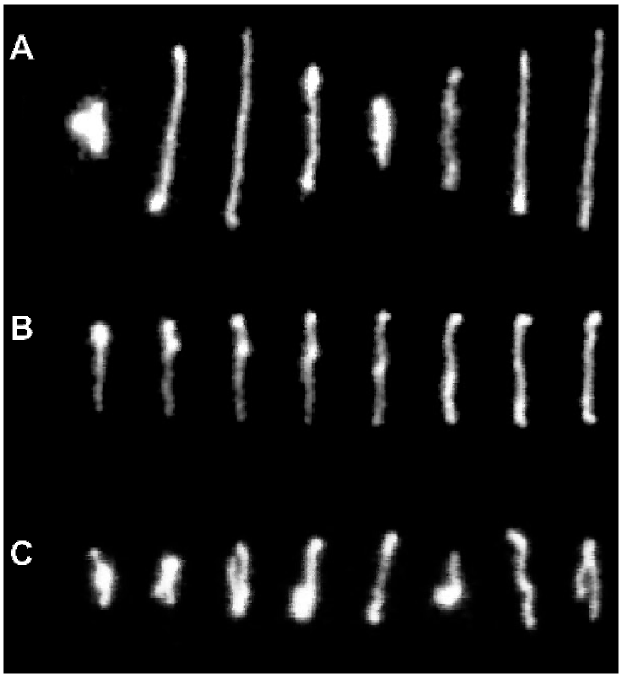

Figure 1.2: Snapshots of individual λ−phage DNA chains undergoing conformational changes under steady shear (image taken from Smith *et al.* [3]).

In order to move from atomistic scale simulations (such as Molecular Dynamics) to hydrodynamics and the continuum limit, it is useful to develop tools and methodologies that will help bridge the time- and length-scale gap. Brownian Dynamics have dominated the meso-scale arena for years, while the Lattice-Boltzmann method [21, 22, 23] provides an alternative approach. The Dissipative Particle Dynamics (DPD) method [24] is a promising, relatively new meso-scale simulation method and many consistency issues still remain open. However, there has been substantial effort by many research groups to employ DPD as a Brownian Dynamics alternative. This dissertation focuses on issues that have not been addressed before in the DPD framework, such as λ−DNA modeling and efficient numerical integrators for complex fluids. Mesoscopic models such as the Marko-Siggia [25] force-extension formula motivate us to carry out computations and compare the DPD results with existing ones in the literature, mostly from theory, Brownian Dynamics and experimental data.

1.2 Dissertation Outline

Research presented in this work is divided into two distinct parts. Part I contains results from *continuum* simulations. More specifically, Direct Numerical Simulation (DNS) is used for addressing problems in the numerical solution of macroscopic equations governing non-Newtonian fluids. Part II, on the other hand, addresses physical and numerical issues arising in the *atomistic* level of such simulations, using the particle-based Dissipative Particle Dynamics (DPD) approach. In general, the problems we address focus on

- ▷ the mathematical formulation of the underlying problems
- ▷ the numerical discretization and solution method
- ▷ numerical/computational problems and ways to overcome them
- ▷ related physical results and their possible dependence on the numerics

Part I contains:

- ▶ Chapter 2: A study of the FENE-P model, its formulation and the use of the spectral viscosity method, suitable for high order discretizations, applied to the conformation tensor. Examples from two- and three-dimensions are presented together with convergence tests and comparison with other studies.

- ▶ Chapter 3: A study of the second-order (Reiner-Rivlin) fluid, its formulation and the use of the spectral viscosity and polynomial over-integration methods for numerical stabilization. The hole pressure problem, together with Kearsley's flow in a parallel slot are also described. Numerical results for the hole pressure problem in Newtonian flows are presented. Direct comparison with experimental data is presented and reasonable agreement with empirical theories is established. The final section deals with numerical studies for the hole pressure problem in Reiner-Rivlin flows. An approximate scaling of the Stokes hole pressure involving the diameter of the tube relative to the channel height is obtained.

Part II contains:

- Chapter 5: A description of the DPD method, the motivation behind the simulation of complex fluids using DPD, the governing equations and the polymeric models this work employs.

- Chapter 6: A study of two integrating schemes for DPD, including a novel family of time-staggered algorithms suitable for polymeric systems governed by hybrid soft and hard interactions. Convergence tests are presented, together with parametric studies involving relaxation parameters.

- Chapter 7: A collection of physical applications, including DNA chains under shear and comparison with experimental and other computational works. Several issues, such as the Schmidt number of the DPD fluids, are addressed and parametric effects of the employed thermostats are examined.

Part I

Macroscopic Simulations

Chapter 2

The FENE-P Viscoelastic Model

2.1 Numerical Simulation of the FENE-P Model

There has been substantial progress in the development of high-order methods and specifically spectral methods for viscoelastic flows started with the work of [26]; see, for example, [12] and references therein. However, complex-geometry flows and high Weissenberg and Reynolds number regimes still present formidable difficulties. The loss of monotonicity of the solution of the stress field for many viscoelastic models becomes an even greater challenge for high-order methods. However, new ideas developed in the context of aerodynamic flows, e.g. discontinuous Galerkin methods and new stabilization techniques, have provided a new framework for developing robust high-order solvers for viscoelastic flows in domains of complex geometries. Another effective approach demonstrated in [27] and [28] is the use of Lagrangian and semi-Lagrangian methods that provide high-order accuracy and enhanced stability.

Recent studies by Fan et al. with *hp* finite elements [29] have examined standard benchmark problems using the *streamline upwind Petrov-Galerkin* (SUPG) technique combined with three different formulations: the *elastic viscous split stress* (EVSS), the *discrete* EVSS (DEVSS) and a third one, called MIX1, which proves to be very efficient in computational resources. Chauvière and Owens [30] have also used the SUPG in conjunction with features of discontinuous Galerkin methods (the SUPG-EE *element-by-element* method) for a variety of models. These include macroscopic models such as the Oldroyd-B, the finitely extensible non-linear elastic - Peterlin (FENE-P) and the Phan-Thien-Tanner (PTT) model, but also mesoscopic models such as the FENE model [31] that do not possess closed-form constitutive equations.

The dumbbell model has been at the center of viscoelastic studies due to its physical significance. The model suggests that dilute polymeric solutions are a mixture of the solvent and the polymer, where the solvent can stretch and convect the polymer molecules that are assumed to behave like elastic springs. In the limiting case of the spring being able to be stretched infinitely, the model becomes the simpler macroscopic Oldroyd-B model (or Hookean dumbbell model), which is less physical. A non-linearity was introduced first by Warner [32] to assign a maximum value to the extensibility of the spring, thus resulting in the FENE model. This model cannot be considered macroscopic, as stated above, but the modified *ensemble-averaged* FENE model, known as FENE-P, can. This model has been extensively studied by van Heel et al. [33], where they proposed a slight modification of the original model. Beris and his collaborators [34, 35] have also used the model to demonstrate turbulent drag reduction.

In this work we will examine the standard FENE-P model as it appears in the literature and with some small scaling variations, as those appear in the works of [11] and [1]. The discretization in space is based on the *modal version* of spectral/*hp* elements while in time a high-order splitting scheme is employed [36]. Monotonicity is maintained using a diffusion convolution kernel that controls the high-order modes, the so-called spectral vanishing viscosity (SVV) method.

SVV was first introduced by Tadmor (1989) in [37] in the context of constructing *monotonicity-preserving* discretizations to hyperbolic conservation laws. More recently, it has been employed successfully in formulating alternative large-eddy simulation (LES) approaches [38]. Also, in [39], the Legendre spectral vanishing method was shown to effectively control the Gibbs phenomenon, while in [40], the SVV approach was employed in two-dimensional simulation of waves in stratified atmosphere. The SVV approach guarantees an essentially non-oscillatory behavior although some small oscillations of *bounded amplitude* may be present in the solution. This theory is based on three key components:

1. A vanishing viscosity amplitude which decreases with the mode number;
2. A viscosity-free spectrum for the lower, most energetic modes; and
3. An appropriate viscosity kernel for the high wavenumbers.

This effective regularization is determined by parameters whose range is given directly by the *non-linear* theory for advection-dominated systems. More recent work has extended the method to superviscosity formulations, first by Tadmor [41] and later by Ma [42, 43], in order to extend the range of the *viscosity-free* spectrum.

In this work, we demonstrate the use and effectiveness of this technique using both analytic solutions as well as standard benchmark problems in two- and three-dimensions.

2.2 Mathematical Formulation

2.2.1 Governing Equations for the FENE-P Model

Incompressible viscoelastic flows for dilute polymer solutions can be modeled by a set of three equations: the equation for momentum conservation, the constitutive relationship describing the evolution of the non-Newtonian part of the stress tensor and, finally, the divergence-free condition for the velocity components. In this work we will specifically examine the FENE-P (**F**initely **E**xtensible **N**on-linear **E**lastic - **P**eterlin) model. This model is based on the assumption of a dumbbell shape for the polymer chains, and is further described by a function due to Peterlin that incorporates the maximum value allowed for the extension of the polymer chains. The non-dimensional momentum conservation equation takes the form

$$\frac{\partial \mathbf{u}}{\partial t} + \mathbf{u} \cdot \nabla \mathbf{u} = -\nabla p + \frac{1}{Re}\left[\beta \nabla^2 \mathbf{u} + (1-\beta)\nabla \cdot \mathbf{s}\right] + \mathbf{F} \tag{2.1}$$

where $\mathbf{u}$ denotes the velocity vector, $\mathbf{s}$ denotes the stress contribution due to the viscoelastic properties of the fluid, and β denotes the ratio of the viscosities $\frac{\eta_s}{\eta_s+\eta_p}$ and is also referred to as the *coupling parameter* later on. Here η_s denotes the viscosity of the solvent and η_p is the viscosity of the polymer. Clearly, when $\beta = 1$ this reduces to the Newtonian case. The Reynolds number in the above equation is defined as $Re = \rho U L/(\eta_s + \eta_p)$, with U, L and ρ denoting characteristic values of the velocity, length and density of the flow, respectively. The FENE-P model is based on a non-linear relation between the *stress* tensor $\mathbf{s}$ and the *conformation* tensor $\mathbf{c}$. The stress tensor $\mathbf{s}$ is defined through $\mathbf{c}$ by

$$\mathbf{s} = \frac{f(r)\mathbf{c} - \mathbf{I}}{We} \tag{2.2}$$

Here We denotes the Weissenberg number defined as $We = \lambda\kappa$, where κ is a typical shear rate of the flow and λ is a characteristic time constant related to the phenomenon of stress relaxation, typical of viscoelastic fluids. We can further define the Deborah number $De = \frac{\lambda}{T}$, where the unit of time T should be a typical time scale of the flow. However, in this chapter we will only be using the Weissenberg number definition. In the above equation $f(r)$ can be identified as the *Peterlin function*

$$f(r) = \frac{L^2 - R^2}{L^2 - r^2} \tag{2.3}$$

where $r^2 = \text{trace}(\mathbf{c})$ and the small correction R is usually set to zero, by redefining We and L. However, for consistency with other definitions, e.g. [34, 11], here we will require $R = \sqrt{3}$ (for three-dimensions) and $R = \sqrt{2}$ (for two-dimensions) since this proves to be convenient when we derive the conformation tensor analytic solution in the convergence studies. In the above relation, L is the maximum extensibility of the polymer chain. The conformation tensor has been non-dimensionalized by $\frac{k_B T_0}{H}$ where k_B is the Boltzmann constant, T_0 is the absolute temperature and H is the spring constant of the FENE-P dumbbell. The evolution equation for the conformation tensor $\mathbf{c}$ is given by

$$\frac{\partial \mathbf{c}}{\partial t} + \mathbf{u} \cdot \nabla \mathbf{c} - [\mathbf{c} \cdot (\nabla \mathbf{u}) + (\nabla \mathbf{u})^T \cdot \mathbf{c}] = -\frac{f(r)\mathbf{c} - \mathbf{I}}{We} \tag{2.4}$$

where ^{T} denotes transposition. The left-hand-side of (2.4) is known as the *upper convected derivative*. The boundary conditions for the conformation tensor will be specifically discussed in the problems of sections 2.2.4 and 2.3.

2.2.2 Discretization

For the temporal discretization of the Navier-Stokes equations we use a time-splitting stiffly-stable scheme. Stiffly-stable type schemes enhance stability through backwards differentiation. The implemented scheme has three different steps and it is an extension of the high-order splitting scheme proposed in [44]:

1. Non-linear step:

$$\hat{\mathbf{u}} = \sum_{q=0}^{J_u-1} \alpha_q \mathbf{u}^{n-q} + \Delta t \sum_{q=0}^{J_u-1} \beta_q \left[-(\mathbf{u}^{n-q} \cdot \nabla)\mathbf{u}^{n-q} + \frac{(1-\beta)}{Re} \nabla \cdot \mathbf{s}^{n-q} + F^{n-q} \right] \tag{2.5}$$

where $\mathbf{s}$ is the contribution from the polymer computed from:

$$\mathbf{s}^n = \frac{f(r)\mathbf{c}^n - \mathbf{I}}{We} \tag{2.6}$$

The evolution equation of the conformation tensor is discretized using the following scheme:

$$\hat{\mathbf{c}} = \mathbf{c}^n + \Delta t \sum_{q=0}^{J_c-1} \xi_q \Bigg[\mathbf{c}^{n-q} \cdot \nabla \mathbf{u}^{n-q} + (\nabla \mathbf{u}^{n-q})^T \cdot \mathbf{c}^{n-q} \\ - (\mathbf{u}^{n-q} \cdot \nabla)\mathbf{c}^{n-q} - \frac{[f(r)\mathbf{c}]^{n-q} - \mathbf{I}}{We} \Bigg] \tag{2.7}$$

For stabilization a convolution kernel that introduces the proper amount of diffusion is then employed (see next section) as follows:

$$\epsilon \nabla \cdot (Q_N * \nabla \mathbf{c}^{n+1}) - \frac{1}{\Delta t}\mathbf{c}^{n+1} = -\frac{\hat{\mathbf{c}}}{\Delta t} \tag{2.8}$$

where Q_N is a smooth kernel that controls which modes (wavenumbers) are affected.

The implemented boundary condition for the two-dimensional case are $\frac{\partial \mathbf{c}}{\partial n}^{n+1}|_\Gamma = 0$ and $\mathbf{c}^{n+1}|_\Gamma = \hat{\mathbf{c}}|_\Gamma$. In the three-dimensional case we only implemented the latter. We have systematically studied the effect of both of the above boundary conditions, showing that accuracy is not affected by them. From the numerical experiments that we performed, the Neumann boundary condition seems to enhance stability. Also, our benchmark results do not show any appreciable differences as will be shown in sections 2.2.4 and 2.3.

In the above notation $J_u \in \{1, 2, 3\}$ is the extrapolation order for the velocity field, $J_c = 2$ is the integration order of the conformation tensor, n is the current time step, α_q, β_q are coefficients associated with the stiffly-stable scheme [44] as shown in table 2.1, ξ_q are coefficients associated with the Adams-Bashforth scheme, ^{T} denotes matrix transposition, N denotes N^{th} polynomial order, $(*)$ denotes the convolution operator, and finally $|_\Gamma$ denotes

Coefficient	First Order	Second Order	Third Order
γ_0	1	3/2	11/6
α_0	1	2	3
α_1	0	$-1/2$	$-3/2$
α_2	0	0	1/3
β_0	1	2	3
β_1	0	-1	-3
β_2	0	0	1

Table 2.1: Coefficients $\alpha_q, \beta_q, \gamma_0$ associated with the stiffly-stable scheme.

value evaluation at the boundary.

2. Pressure step:

$$\nabla^2 p^{n+1} = \nabla \cdot \left(\frac{\hat{\mathbf{u}}}{\Delta t} \right) \tag{2.9}$$

with the boundary condition

$$\frac{\partial p^{n+1}}{\partial n} = \mathbf{n} \cdot \left[\hat{\mathbf{u}} - \frac{\beta}{Re} \sum_{q=0}^{J_p - 1} \beta_q \nabla \times (\nabla \times \mathbf{u}^{n-q}) \right] \tag{2.10}$$

3. Viscous step:

$$\left[\nabla^2 - \frac{\gamma_0 Re}{\beta \Delta t} \right] \mathbf{u}^{n+1} = -\frac{\gamma_0 Re}{\beta \Delta t} \hat{\mathbf{u}} + \frac{\gamma_0 Re}{\beta} \nabla p^{n+1} \tag{2.11}$$

In the above notation $J_p \in \{1, 2, 3\}$ is the extrapolation order for the pressure. The overall temporal accuracy of the scheme is $\mathcal{O}(\Delta t^2)$ and it is dictated by $J_c = 2$; it can be readily extended to third-order in time similar to the velocity solver in the Newtonian case [44].

For **spatial discretization** we have adopted the spectral/*hp* element method, see [36]. It employs standard unstructured and hybrid grids unlike previous approaches that require special structured grids. This new version of the spectral element method uses a hierarchical basis based on Jacobi polynomials with mixed weights that accommodate accurate numerical quadrature and flexibility in discretization by employing *polymorphic subdomains*. The degenerate case corresponds to a linear finite element discretization with the vertices corresponding to linear modes. Each element consists of N modes per direction but no gridding within the element is required as all computations are done in modal space. Specifically, each element is separated into linear vertex modes, edge modes, face modes and interior or bubble modes.

For a smooth solution, the error in a Galerkin projection of a smooth function converges exponentially fast to zero by simply increasing the number of modes per element/subdomain. This allows for selective refinement and sharp *a priori* error estimates in the numerical solution without the overhead cost associated with regeneration of a three-dimensional mesh. Another distinction with other versions of the *hp* finite element method that employ monomials is that very high order is readily employed (e.g., $N = 32$) and that the multi-dimensional basis is a tensorial product in the transformed domain, [36]. This, in turn, leads to good efficiency in simulations with high-order N. The new method has been implemented in the serial and parallel versions of the computer code named $\mathcal{N}\varepsilon\kappa\mathcal{T}\alpha r$ [45].

2.2.3 The Spectrally Vanishing Viscosity (SVV) Method

Tadmor (1989) [37] first introduced the concept of spectral vanishing viscosity (SVV) for hyperbolic conservation laws. Specifically, he considered the inviscid Burgers' equation

$$\frac{\partial}{\partial t}u(x,t) + \frac{\partial}{\partial x}\left(\frac{u^2(x,t)}{2}\right) = 0, \tag{2.12}$$

subject to given initial and boundary conditions. The distinctive feature of solutions to this problem is that spontaneous jump discontinuities (shock waves) may develop, and hence *a class* of weak solutions can be admitted. Within this class, there are many possible solutions, and in order to single out the physically relevant one an additional entropy condition is applied, of the form

$$\frac{\partial}{\partial t}\left(\frac{u^2(x,t)}{2}\right) + \frac{\partial}{\partial x}\left(\frac{u^3(x,t)}{3}\right) \leq 0. \tag{2.13}$$

In the context of viscoelastic flows, the objective is to obtain a unique stable solution of the conformation stress equation. In the SVV method of Tadmor (1989), a small amount of *mode-dependent* dissipation is added that satisfies the entropy condition, yet retains spectral accuracy. It is based on viscosity solutions of non-linear Hamilton-Jacobi equations, which have been studied systematically in [46]. Specifically, the viscosity solution for the Burgers' equation has the form

$$\frac{\partial}{\partial t}u(x,t)+\frac{\partial}{\partial x}\left(\frac{u^2(x,t)}{2}\right)=\epsilon\frac{\partial}{\partial x}\left[Q_\epsilon\frac{\partial u}{\partial x}\right], \tag{2.14}$$

where $\epsilon(\rightarrow 0)$ is a viscosity amplitude and Q_ϵ is a viscosity kernel. Convergence may then be established by compactness estimates combined with entropy dissipation arguments [37]. To respect spectral accuracy, the SVV method makes use of viscous regularization and equation (2.14) may be rewritten in discrete form (retaining N modes)

$$\frac{\partial}{\partial t}u_N(x,t)+\frac{\partial}{\partial x}\left[\mathcal{P}_N\left(\frac{u^2(x,t)}{2}\right)\right]=\epsilon\frac{\partial}{\partial x}\left[Q_N*\frac{\partial u_N}{\partial x}\right], \tag{2.15}$$

where the star ($*$) denotes convolution and $\mathcal{P}_N$ is a projection operator. Q_N is a viscosity kernel, which is only activated for high wavenumbers. In Fourier space, this kind of spectral viscosity can be efficiently implemented as multiplication of the Fourier coefficients of u_N with the Fourier coefficients of the kernel Q_N, i.e.,

$$\epsilon\frac{\partial}{\partial x}\left[Q_N*\frac{\partial u_N}{\partial x}\right]=-\epsilon\sum_{M\leq|k|\leq N}k^2\hat{Q}_k(t)\hat{u}_k(t)e^{ikx},$$

where k is the wavenumber, N the number of Fourier modes, and M the wavenumber above which the spectral vanishing viscosity is activated. Originally, Tadmor (1989) used

$$\hat{Q}_k=\begin{cases}0, & \mid k\mid\leq M\\ 1, & \mid k\mid> M,\end{cases} \tag{2.16}$$

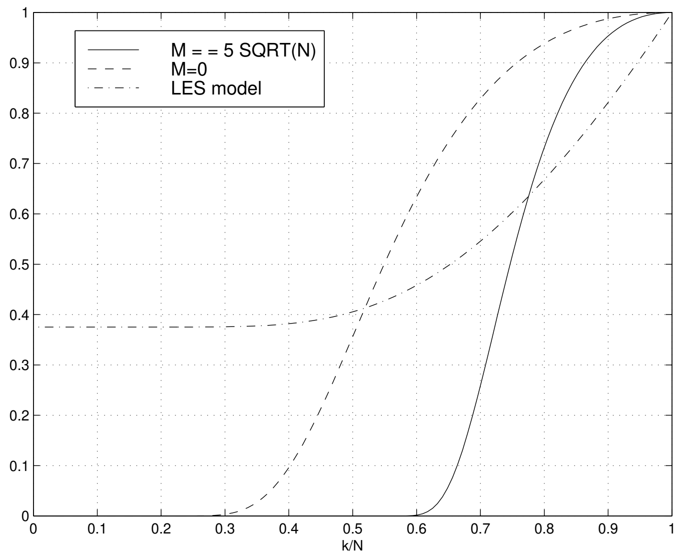

Figure 2.1: Normalized viscosity kernels for the spectral vanishing viscosity (dash line $C = 0$ and solid line $C = 5$) and the Kraichnan/Chollet-Lesieur viscosity (dash-dot line).

with $\epsilon M \sim 0.25$ based on considering minimization of the total-variation of the numerical solution. In subsequent work, however, a smooth kernel was used, since it was found that the C^∞ smoothness of $\hat{Q}_k$ improves the resolution of the SVV method. For Legendre pseudo-spectral methods, Maday et al. [47] used $\epsilon \approx N^{-1}$, activated for modes $k > M \approx 5\sqrt{N}$, with

$$\hat{Q}_k = e^{-\frac{(k-N)^2}{(k-M)^2}}, \quad k > M. \tag{2.17}$$

In order to see the difference between the convolution operator on the right-hand-side in equation (2.15) and the usual viscosity regularization, we follow Tadmor [48] and expand as

$$\epsilon \frac{\partial}{\partial x}\left[Q_N * \frac{\partial u_N}{\partial x}\right] = \epsilon \frac{\partial^2 u_N}{\partial x^2} - \epsilon \frac{\partial}{\partial x}[R_N(x,t) * \frac{\partial u_N}{\partial x}] \tag{2.18}$$

where

$$R_N(x,t) \equiv \sum_{k=-N}^{N} \hat{R}_k(t) e^{ikx}; \quad \hat{R}_k(t) \equiv \begin{cases} 1 - \hat{Q}_k(t) & |k| \geq M \\ 1 & |k| < M \end{cases} \tag{2.19}$$

The extra term appearing in addition to the first standard viscosity term makes this method different. It measures the distance between the spectral (vanishing) viscosity and the standard viscosity. This term is bounded in the L_2 norm similarly to the spectral projection error. In this paper we refer to the viscosity as vanishing as the theory requires that

$$\epsilon \approx \frac{1}{N^\theta logN}, \quad \theta \leq 1$$

and thus $\epsilon \to 0$ for high wavenumbers.

The basis we use is written in terms of Jacobi polynomials and is decomposed into *vertex* modes, *edge* modes and *interior* modes. This is a semi-orthogonal basis (see [36] for details) but the SVV procedure should be applied to orthogonal modes. To this end, we will transform the semi-orthogonal basis to the orthogonal one as outlined below.

If we examine the weak form of the SVV term $\epsilon \frac{\partial}{\partial x}\left(Q_\epsilon \frac{\partial u}{\partial x}\right)$ only, ignoring boundary terms and the leading coefficient, we have the following basic form of the SVV operator:

$$\left(\frac{\partial v}{\partial x}, Q\frac{\partial u}{\partial x}\right) \tag{2.20}$$

where v is a test function taken from the Jacobi polynomials $\{\phi_k\}$ and $u = \Sigma_k \hat{u}_k \phi_k$. In the derivation below we will assume that all discrete summations are from $1, ..., N$. In the notation above and henceforth $(\cdot, \cdot)$ denotes the L_2 inner product and it is assumed that the continuous and discrete inner products are interchangeable, given sufficient quadrature order.

Now, let $\mathbf{B}$ be a matrix that transforms the modal coefficients $\hat{u}$ for the basis functions $\{\phi_k\}$ to $\tilde{u}$ in $\{\psi_k\}$ space, where $\{\phi_k\}$ is our C^0 basis used for the Galerkin formulation and $\{\psi_k\}$ is an *orthonormal* basis that spans the same space as $\{\phi_k\}$. Let $\mathbf{F}$ be a diagonal matrix that acts as a filtering function (the entries of which are given by equation (2.17)). In the notation above we have $\tilde{u} = \mathbf{B}\hat{u}$. Our goal is to filter the coefficients $\tilde{u}$ instead of filtering the coefficients $\hat{u}$. Hence, we would like to transform (via the matrix $\mathbf{B}$) to the orthogonal space, filter, and then transform back. This can be accomplished by the operation

$$\hat{\hat{u}} = \mathbf{B}^{-1}\mathbf{F}\mathbf{B}\hat{u}. \tag{2.21}$$

We can now write expression (2.20) in the discrete form using matrix notation as follows:

$$\mathbf{S}^T\mathbf{B}^{-1}\mathbf{F}\mathbf{B}\mathbf{M}^{-1}\mathbf{S}\hat{u} \tag{2.22}$$

where $\mathbf{S}_{ij} = \left(\phi_i, \frac{\partial \phi_j}{\partial x}\right)$ and $\mathbf{M}_{ij} = (\phi_i, \phi_j)$. It can be shown that $\mathbf{B}^{-1} = \mathbf{M}^{-1}\mathbf{B}^T$, and hence the discrete form of the SVV operator for the Galerkin method is given by:

$$\mathbf{S}^T\mathbf{M}^{-1}\mathbf{B}^T\mathbf{F}\mathbf{B}\mathbf{M}^{-1}\mathbf{S}\hat{u}. \tag{2.23}$$

Note that the above discrete operator is symmetric, semi-positive definite.

The above formulation was first introduced by Kirby [49] for LES. It has been suggested that the artificial viscosity added usually in the stress equation in physical space is analogous to subgrid viscosity in large-eddy simulations (LES). That is, instabilities typically arise when the small scales are under-resolved and, correspondingly, solution monotonicity is lost. To this end, it is instructive to compare the spectral vanishing viscosity to the spectral eddy-viscosity introduced by Kraichnan [50] as modified by Chollet-Lesieur [51, 52]. The latter has the non-dimensional form [52]

$$\nu(k/N) = K_0^{-3/2}[0.441 + 15.2exp(-3.03N/k)], \quad K_0 = 2.1 \tag{2.24}$$

Comparing the Fourier analog of the eddy-viscosity employed in LES [51] to the viscosity kernel $Q_k(k, M, N)$ introduced in the SVV method, figure 2.1 shows both viscosity kernels normalized by their maximum value at $k = N$. For SVV, two different values of the cut-off wavenumber are considered, i.e.,

$$M = C\sqrt{N} \quad \text{for } C = 0 \text{ and } C = 5, \tag{2.25}$$

and are shown in the plot of figure 2.1. In particular, the solid line can be thought of as a *stability barrier* above which monotonicity and thus stability is not guaranteed. On the other hand, the dashed line can be thought of as an *accuracy barrier* below which the convergence of the method is affected. This range has been used in most of the numerical experiments so far (see for example [47, 40, 38]) and is consistent with the theoretical results [37]. In the plot it is shown that, in general, the two forms of viscosity have similar distributions but that the SVV form does not affect the first one-third or one-half of the spectrum (viscosity-free portion) and it increases faster than the Kraichnan/Chollet-Lesieur eddy-viscosity in the higher wavenumbers range, e.g. in the second-half of the spectrum.

In the following, we will address the effect of SVV on the convergence rate and the stability of spectral/*hp* element discretization.

2.2.4 Convergence and SVV Parameters

The convergence tests used to show the effect of SVV are based on an analytic solution derived for the conformation tensor in a channel flow. By letting $R = \sqrt{2}$ for a two-dimensional flow and $R = \sqrt{3}$ for a three-dimensional flow in equation (2.3), we can simplify the analytic solution for velocity fields of the form $\mathbf{u} = (U(y), 0, 0)$. Thus, we can examine the effect of the two different parameters appearing on the SVV formulation (the cutoff mode M and the value of ε) and the L_2 error of the numerical results when compared to the analytic solution. As stated in [34], the exact solution of the conformation tensor for a three-dimensional problem can be identified as the following (symmetric) matrix:

$$\mathbf{c} = \begin{pmatrix} \frac{1}{F(y)}\left[1+\frac{2We^2}{F^2(y)}\left(\frac{dU}{dy}\right)^2\right], & \frac{We}{F^2(y)}\left(\frac{dU}{dy}\right), & 0 \\ & \frac{1}{F(y)}, & 0 \\ & & \frac{1}{F(y)} \end{pmatrix} \tag{2.26}$$

where the following definitions apply:

$$\Omega(y) = \frac{\sqrt{2}We}{L}\frac{dU}{dy}, \tag{2.27}$$

$$F(y) = \frac{\sqrt{3}\Omega(y)}{2\sinh(\phi/3)}, \tag{2.28}$$

$$\phi = \sinh^{-1}(3\sqrt{3}\Omega/2) \tag{2.29}$$

For the two-dimensional case we reduce the value of R from $\sqrt{3}$ to $\sqrt{2}$ and consequently only the upper left 2×2 block appears for the exact expression.

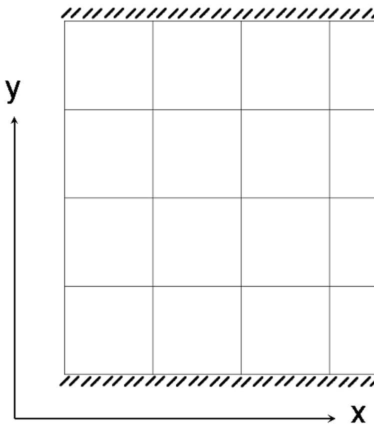

Figure 2.2: The 16-element mesh employed for the convergence tests in two-dimensions. The channel has a non-dimensional length of 2 in both directions.

Based on the above analytic expression, we conclude that the exact relation for the conformation tensor subject to the above restrictions is dependent only on the velocity gradient in the y-direction. Fabricating a non-trivial solution for the flow field for $y \in [-1, 1]$ other than the parabola $U(y) = 1 - y^2$ requires the introduction of a more complicated expression for the driving force $\mathbf{F}$ in equation (2.1). It can be shown that if

$$F_x = \sqrt{\frac{2}{3}}\frac{L}{ReWe}\big[\beta\cosh(3y) + (1-\beta)\cosh(y)\big] \tag{2.30}$$

the corresponding expression for the velocity has the simple but non-trivial form

$$U(y) = \frac{\sqrt{2}}{9\sqrt{3}}\frac{L}{We}\big[\cosh(3) - \cosh(3y)\big]; \qquad\qquad y \in [-1,1]. \tag{2.31}$$

Figure 2.2 shows the two-dimensional mesh that was used to investigate the convergence rate of the method. The mesh we employ consists of 4×4 elements and the domain is as shown, with the length of each side equal to 2. We have set $L = 10, \nu = 0.1$ which gives $Re = \frac{UL}{\nu} \sim \frac{1.02\times 1}{0.1} = 10.2$ and $We = 8$ and considered two values of the coupling parameter β, namely 1 (no coupling, i.e. Newtonian with $\eta_p = 0$) and 0.9 (loose coupling).

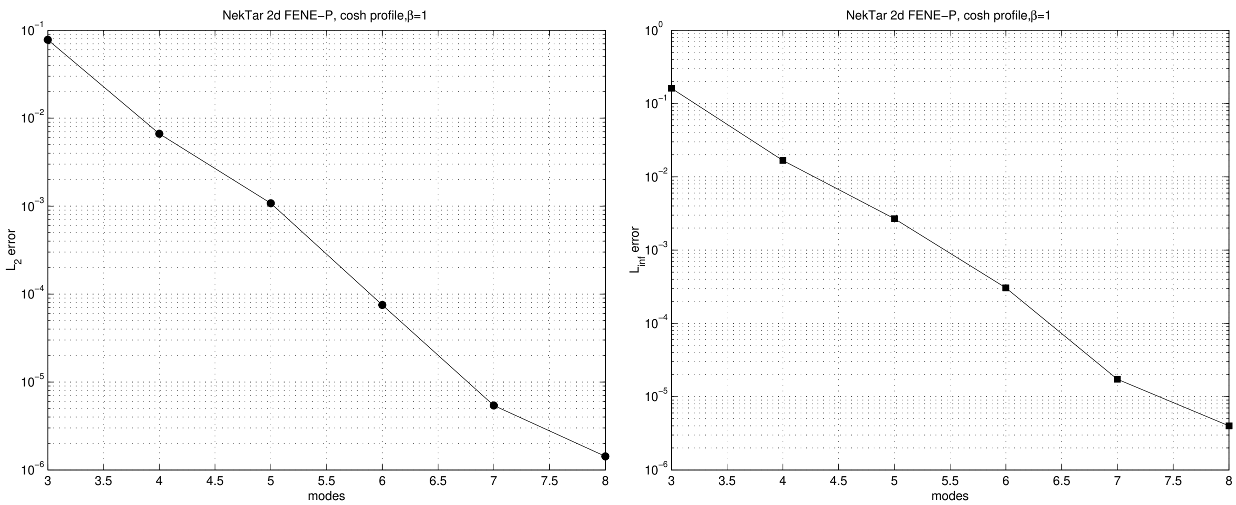

Figure 2.3: Convergence rate in conformation tensor in the L_2 (left) and L_∞ norm (right) for $\beta = 1.0$ (Newtonian).

In figure 2.3 and 2.4 we plot the L_2 and L_∞ error in the conformation tensor (all components)

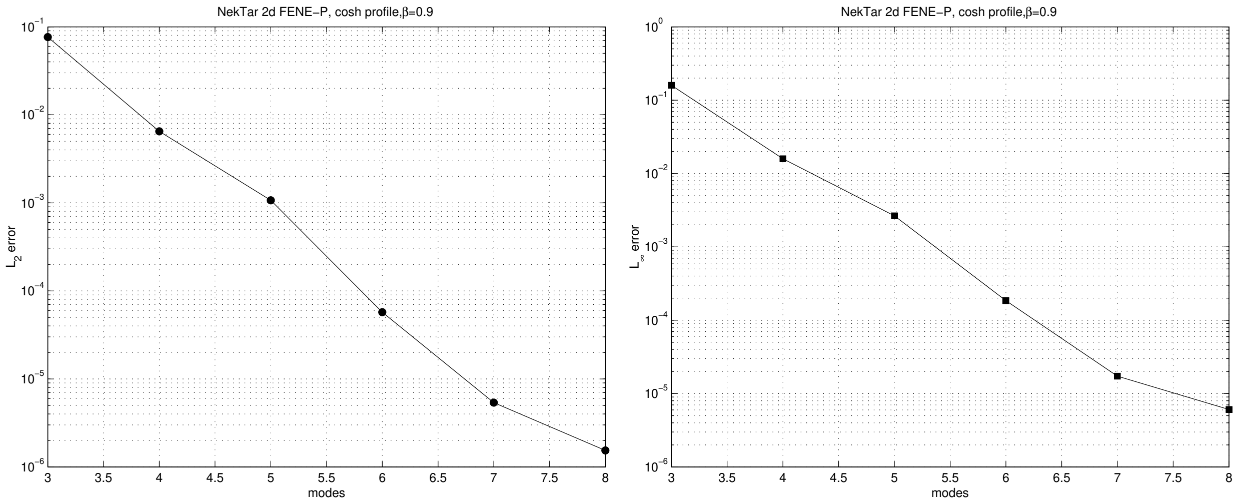

Figure 2.4: Convergence rate in conformation tensor in the L_2 (left) and L_∞ norm (right) for $\beta = 0.9$

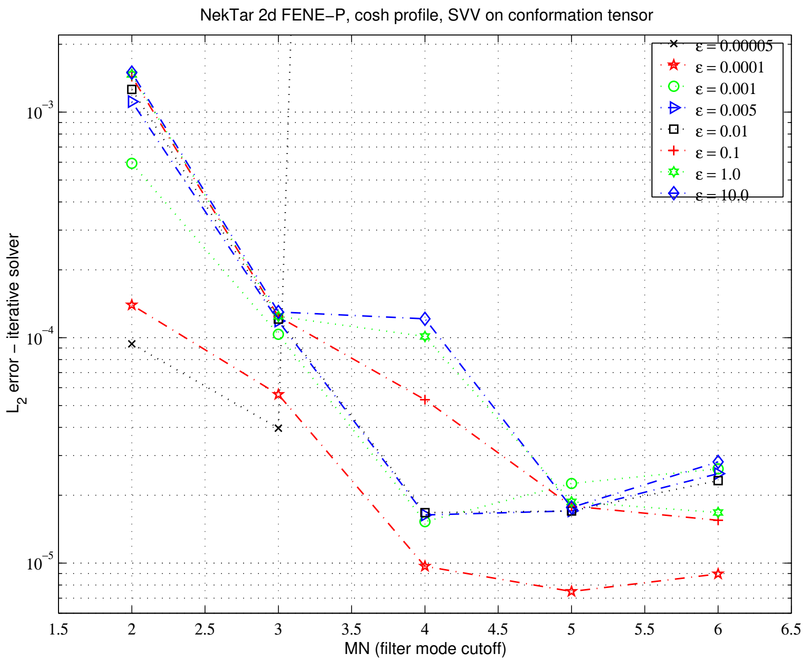

Figure 2.5: Effects of SVV amplitude and cut-off wavenumber on the error of conformation tensor.

for $\beta = 1$ and 0.9 respectively; we see that the solution error converges exponentially to zero for cases. Solutions are obtained for $N \in [3, 8]$. We see that the formal (exponential) accuracy of the discretization is maintained. This is true irrespective of the size of the coupling parameter β although, the greater the value of $(1 - \beta)$ the larger the error is expected to be.

Next we examine how sensitive the numerical solution is with respect to the choice of the SVV parameters; we fix the spectral order to $N = 7$, the coupling parameter $\beta = 0.9$, the Weissenberg number $We = 80$ and $Re \sim 102$. These parameters result to a numerically unstable system, without the use of SVV. In figure 2.5 we plot the L_2 error of the conformation tensor (all components) versus the cut-off wavenumber M for several values of the SVV amplitude ε. With respect to the latter, we see indeed that for larger values we run into a stability barrier whereas for low values of ε the accuracy degrades; such trends are valid for different values of the SVV amplitude as shown in figure 2.5. The stability and accuracy trends with respect to viscosity amplitude ε are also in agreement with Tadmor's theory although here the *optimal* value of ε cannot be predicted precisely by the theory. The absent values correspond to divergent cases.

As a final remark on the selection of the two different boundary conditions $\frac{\partial \mathbf{c}}{\partial n}^{n+1}|_\Gamma = 0$ and $\mathbf{c}^{n+1}|_\Gamma = \hat{\mathbf{c}}|_\Gamma$, we show in figure 2.6 that accuracy is not significantly affected by favoring one or the other. The plot shows the *difference* in the L_2 error between the two, normalized by the L_2 error of the Dirichlet boundary condition.

2.3 Benchmark Problem: Stokes Flow Past a Cylinder in a Channel

To demonstrate the stability and accuracy of the method, we will compare our results with one of the most commonly published set of results on a specific benchmark problem for two-dimensional simulations. The robustness of the scheme will be demonstrated in the well-examined flow past a

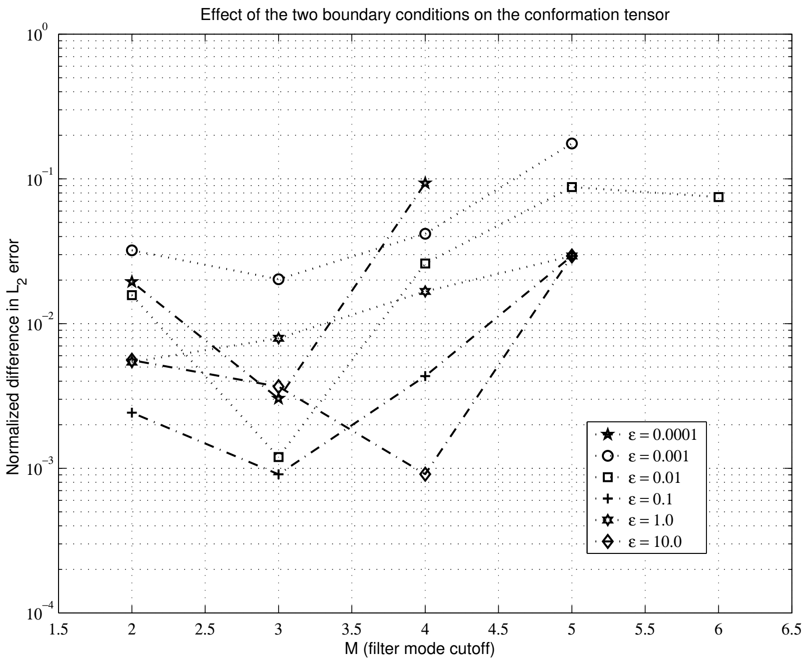

Figure 2.6: Effect of the two different boundary conditions $\frac{\partial \mathbf{c}}{\partial n}^{n+1}|_\Gamma = 0$ and $\mathbf{c}^{n+1}|_\Gamma = \hat{\mathbf{c}}|_\Gamma$ on the L_2 error. Results shown are from the two-dimensional (analytical) case.

two-dimensional cylinder in a symmetric channel. Here, we do not make use of the symmetry, and thus we include the entire domain, unlike past studies. The use of symmetry for Stokes flow is indeed beneficial, but symmetry-breaking bifurcations at some Re regimes demands the use of the full domain, as section 2.4 shows. The computational mesh employs 176 quadrilateral elements as shown in figure 2.7.

The setup of the problem is as follows: The length of the channel is 40 non-dimensional units long ($x \in [-20, 20]$), the channel half-width H is 2 units long ($y \in [-2, 2]$), the radius of the cylinder R is 1 unit long ($R = 1$) and consequently the aspect ratio $\Lambda = R/H = 1/2$. Parabolic inflow of the form

$$u_x(y) = \frac{3}{2}U\big(1 - (\frac{y}{H})^2\big)$$

$$u_y = 0$$

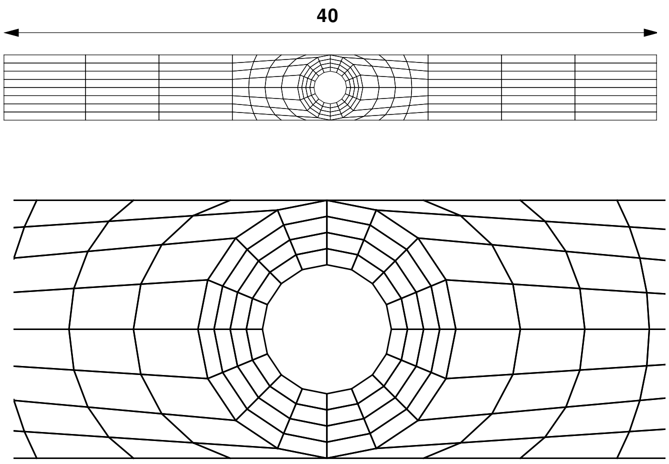

Figure 2.7: The two-dimensional mesh used for the benchmark problem. The curved sides are represented isoparametrically with a high-order expansion. Here, faces are plotted as straight lines.

	$N = 5$	$N = 6$	$N = 7$	$N = 8$	$N = 9$
$We = 0.505$	$\Delta t = 1e-4$	$\Delta t = 1e-4$	$\Delta t = 1e-4$	$\Delta t = 3e-5$	$\Delta t = 1e-5$
$We = 0.608$	$\Delta t = 1e-4$	$\Delta t = 1e-4$	$\Delta t = 1e-4$	$\Delta t = 3e-5$	$\Delta t = 1e-5$
$We = 0.712$	$\Delta t = 1e-4$	$\Delta t = 1e-4$	$\Delta t = 5e-5$	$\Delta t = 3e-5$	$\Delta t = 1e-5$
$We = 0.818$	$\Delta t = 1e-4$	$\Delta t = 5e-5$	$\Delta t = 1e-5$	$\Delta t = 1e-5$	$\Delta t = 1e-5$

Table 2.2: Time step Δt with SVV parameter $\varepsilon = 0.001$ and $M = 2$ for each successful case. N denotes the spectral order per direction.

is imposed along $y \in [-2, 2]$ at $x = -20$, thus the mean value $U = 1$. The above profile is an *not* an exact solution for $\beta \neq 1$; however due the ample length of the domain upstream we anticipate this to have little effect for the studied values of β. The outflow boundary condition at $x = 20$ is treated with Neumann boundary condition set to zero. The boundary conditions for the conformation tensor in the entrance of the channel are Dirichlet and are set to be the analytic values corresponding to $\beta = 1$ as dictated by equation (2.26). We also define the Weissenberg number for this flow to be $We = U\lambda/R$. Choosing the SVV parameters $(\varepsilon, M) = (0.001, 2)$ throughout, the timestep Δt is adjusted as shown in table 2.2. The evolution equation (2.4) for the conformation tensor is solved in physical space explicitly, using the second-order Adams-Bashforth scheme. The additional SVV part of the equation is solved implicitly in modal space. The computations are considered steady-state once the stopping criterion

$$\frac{\|\mathbf{u}^{n+1} - \mathbf{u}^{n}\|_{\infty}}{\Delta t} < 10^{-3}$$

is met. The simulation parameters chosen for this benchmark problem are $\beta = 0.59$, $L = \sqrt{20}$. Consistency with [1, 53] requires, in the two-dimensional case, a small normalization factor for the stress tensor $\mathbf{s} = \alpha(L)\frac{f(r)\mathbf{c}-\mathbf{I}}{We}$, where $\alpha(L) = \frac{L^2+2}{L^2} = 1.1$

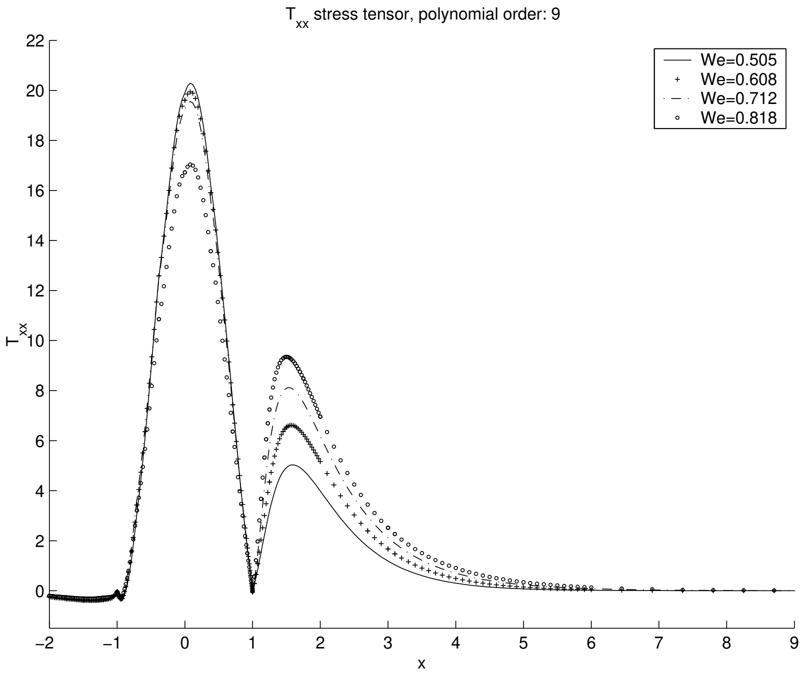

Figure 2.8: T_{xx} stress tensor, polynomial order $N = 9$.

Letting $\tau = (1 - \beta)\mathbf{s}$, we will focus on the *axial normal stress* $T_{xx} = \tau_{1,1}$ profiles on the rim of the cylinder, the wake, and the stagnation points. Comparisons of these values were done with Chauvière's [1, 53] parameters, namely Weissenberg numbers equal to 0.505, 0.608, 0.712 and 0.818. Figure 2.8 shows the profiles of the axial normal stress T_{xx} for a given polynomial order along the x-direction as the Weissenberg number varies. $x \in [-1, 1]$ is the region between the two stagnation points. Observing the axial normal stress at the wake and at $x = 0$, we see that T_{xx} has higher values in the wake region as Weissenberg numbers get higher, but inversely for the highest point on the cylinder $x = 0$.

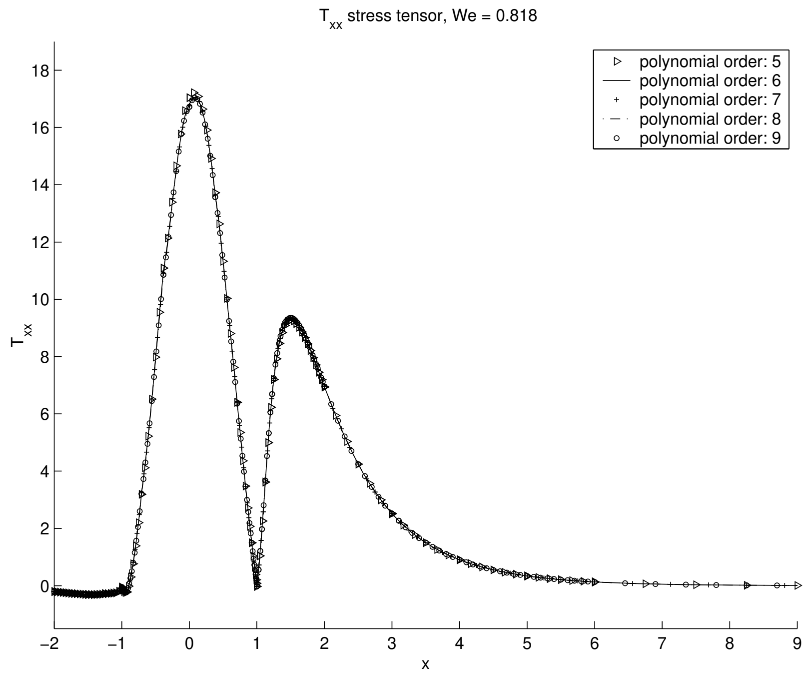

Figure 2.9: Effects of p-refinement: T_{xx} stress tensor, Weissenberg number $We = 0.818$.

Figure 2.9 shows the results of p-refinement for a given Weissenberg number. The agreement among the five different polynomial orders is clear. Of significance is also the drag coefficient F^* on the cylinder normalized as

$$F^* = \frac{F}{4\pi\eta U} \tag{2.32}$$

where $\eta = \eta_s + \eta_p$ is the total viscosity, and as stated earlier $U = 1$. Table 2.3 demonstrates the robustness of the SVV filtering, as none of the values are diverging to infinity, compared to other methods for macroscopic simulations. Table 2.3 also shows the percentage of disagreement between Chauvière [1, 53] and the SVV-calculated values. Naturally, increasing the Weissenberg number increases the disagreement. It has to be noted that in this disagreement the effect of the SVV is secondary. To this end, we performed a series of simulations for $We = 0.505$ (the drag coefficients shown in table 2.3) without applying any SVV filtering. The results support the above conclusion. Comparison was also made on the effect of SVV on the T_{xx} profiles. To this

no SVV	$N=5$	$N=6$	$N=7$	$N=8$	$N=9$
$We = 0.505$	8.992	8.998	8.999	9.002	9.006

SVV	$N=5$	$N=6$	$N=7$	$N=8$	$N=9$
$We = 0.505$	8.998	9.001	9.002	9.003	9.007
$We = 0.608$	8.844	8.848	8.850	8.852	8.856
$We = 0.712$	8.728	8.733	8.738	8.739	8.740
$We = 0.818$	8.639	8.635	8.652	8.653	8.652

Chauvière [1]	$N=5$	$N=6$	$N=7$	$N=8$	$N=9$
$We = 0.505$	9.090	9.093	9.081	9.077	9.076
$We = 0.608$	8.967	8.979	8.964	8.958	8.957
$We = 0.712$	8.886	8.906	8.891	-	-
$We = 0.818$	8.838	-	-	-	-

% difference	$N=5$	$N=6$	$N=7$	$N=8$	$N=9$
$We = 0.505$	1.0138	1.0136	0.8655	0.8122	0.7553
$We = 0.608$	1.3711	1.4579	1.2739	1.1813	1.1303
$We = 0.712$	1.7782	1.9405	1.7197	-	-
$We = 0.818$	2.2529	-	-	-	-

Table 2.3: Drag coefficient F^* for macroscopic simulations with SVV (upper middle) and drag coefficient F^* by Chauvière [1] (lower middle). Empty boxes correspond to divergent runs. It has to be noted here that the corresponding mesoscopic simulations done in [1] did converge. We also present the drag coefficient for $We = 0.505$ without applying any SVV filtering (upper). The percentage of difference between Chauvière's values and the SVV values is shown here too (lower).

end, results from the standard and modified SUPG method ([1, 53], private communications) and the SVV were compared to verify the accuracy and stability of the method. Figure 2.10 shows a good agreement for $We = 0.608$.

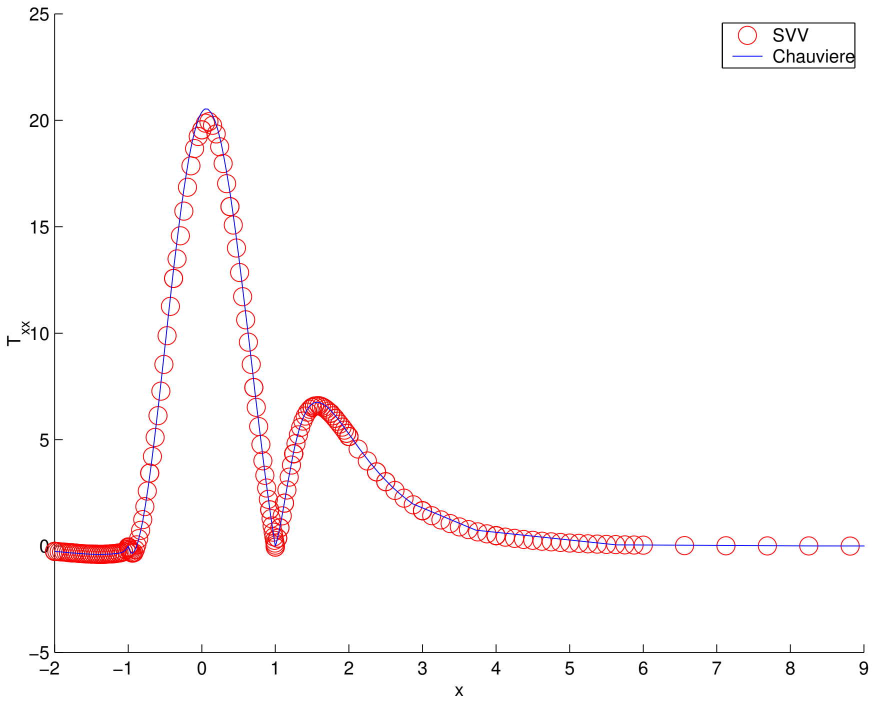

Figure 2.10: Comparison of T_{xx} profiles at $We = 0.608$ and polynomial order $p = 8$.

In figure 2.11 we plot the T_{xx} contours for the Weissenberg number of 0.712 and $N = 8$ close to the cylinder. Good agreement is established between the two results.

Figure 2.12 shows the T_{xx} profiles for higher Weissenberg numbers, ranging from $We = 0.88$ up to $We = 2.00$. Our simulations appear to be highly stable in this range. No attempt was made to reach higher Weissenberg numbers than $We = 2.00$, although no stability or accuracy degradation was present. The qualitative trends agree in these cases as well, i.e. the axial normal stress is higher at the wake of the cylinder for higher Weissenberg numbers but inversely for $x = 0$. Figure 2.13 also shows the drag coefficient variation for $N = 6$ with respect to the Weissenberg number.

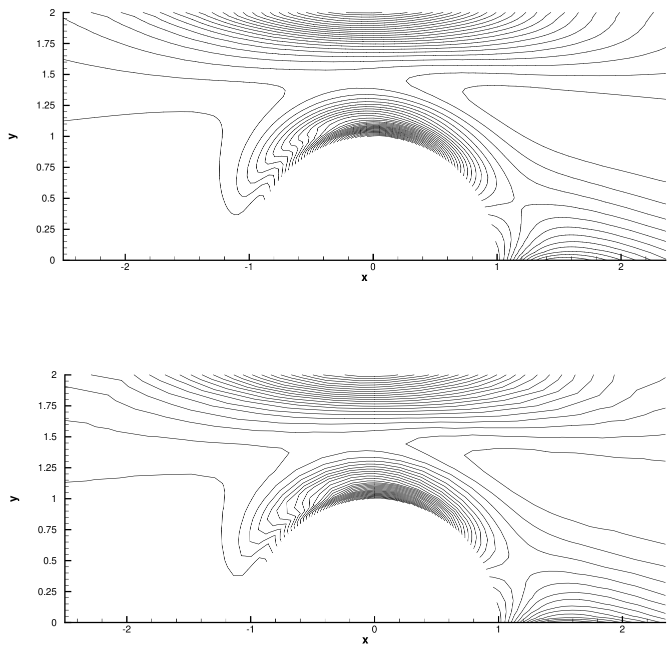

Figure 2.11: T_{xx} contours for $We = 0.712$ and polynomial order $N = 8$. We compare the SVV method (upper) and Chauvière's results [1] (lower).

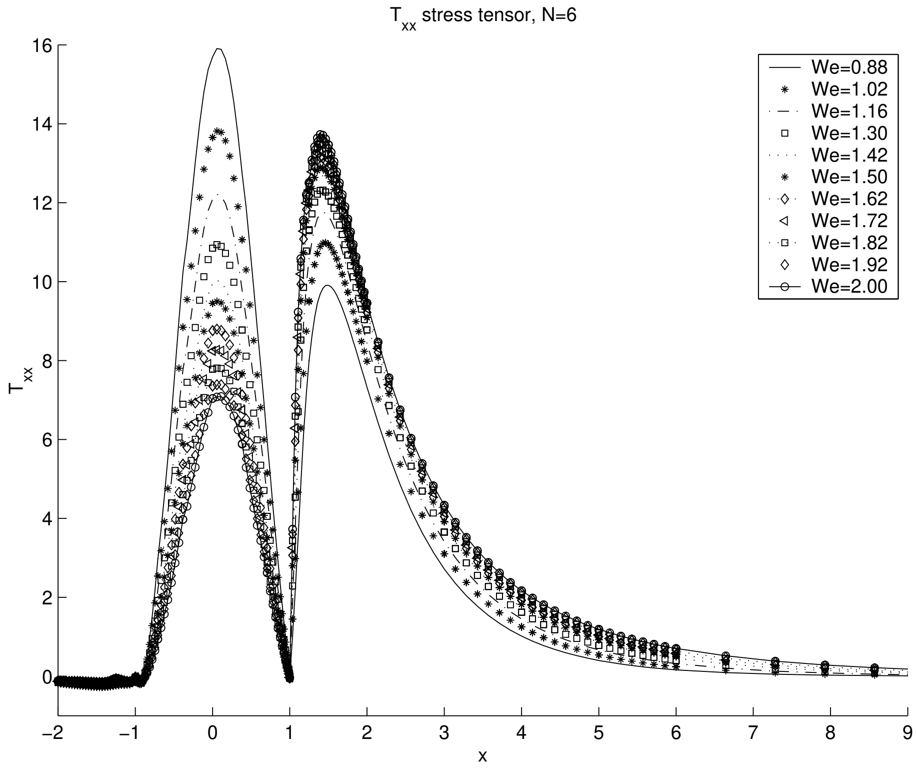

Figure 2.12: T_{xx} profiles for Weissenberg numbers up to 2.0

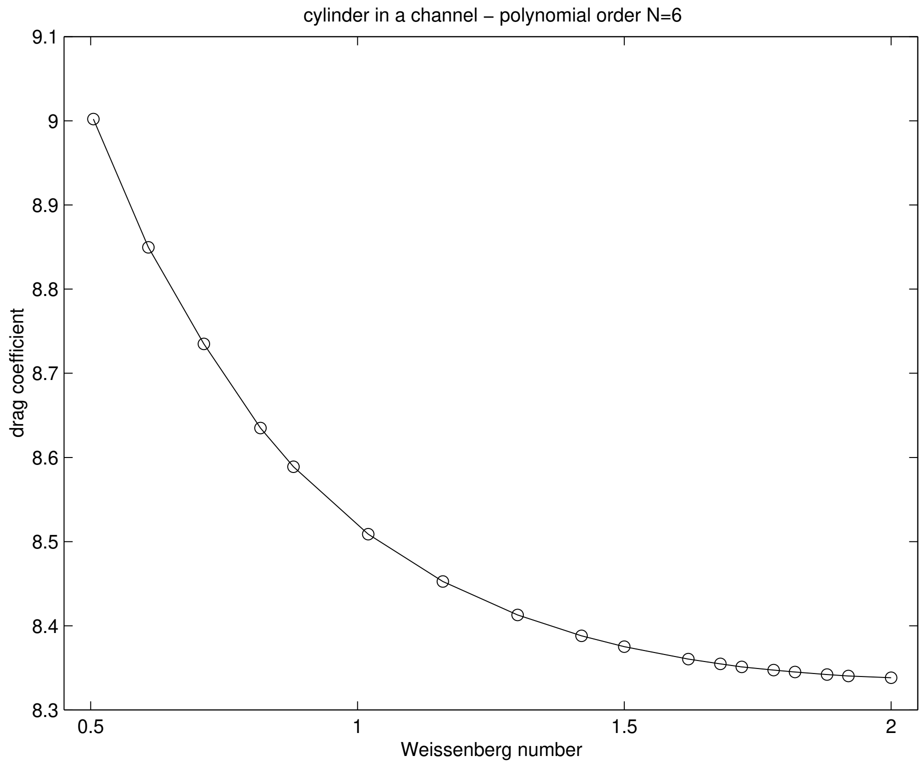

Figure 2.13: Drag coefficient for Weissenberg numbers ranging from 0.505 to 2.0

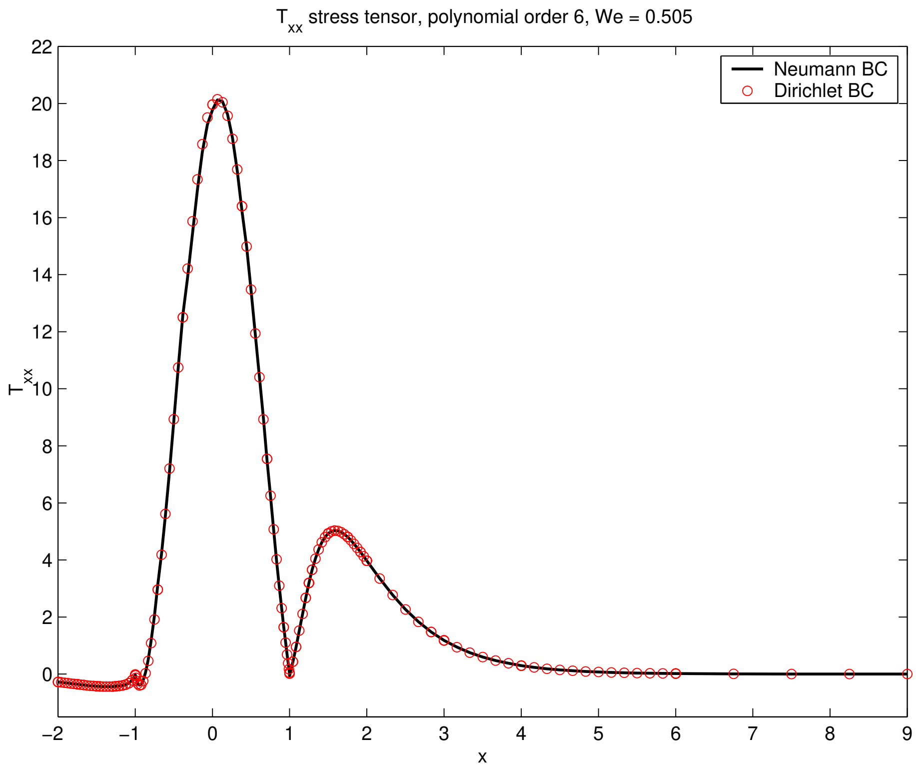

Figure 2.14: T_{xx} profiles for $We = 0.505$ and polynomial order $N = 6$. Here we compare the two different boundary conditions for the conformation tensor.

Finally, comparing again the effect of the two different boundary conditions $\frac{\partial \mathbf{c}}{\partial n}^{n+1}|_\Gamma = 0$ and $\mathbf{c}^{n+1}|_\Gamma = \hat{\mathbf{c}}|_\Gamma$, figure 2.14 shows no appreciable differences in the axial normal stress profiles for $We = 0.505$, verifying the convergence remarks of section 2.2.4.

2.4 Flat Plate in a Channel: Two-Dimensions

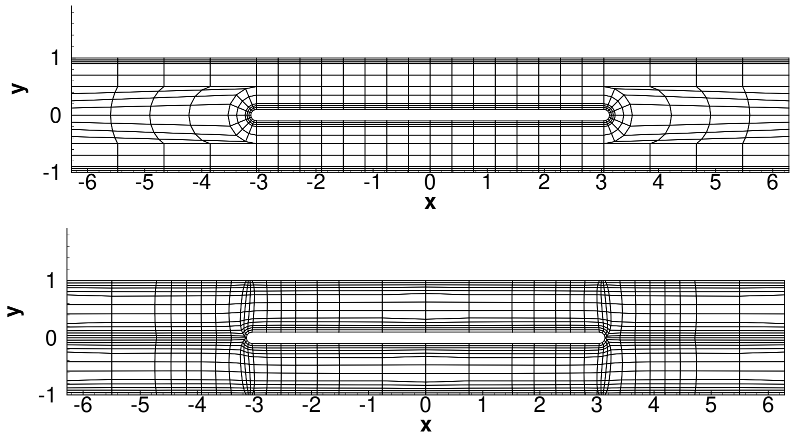

Figure 2.15: The 544-element mesh (upper) and the 936-element mesh (lower) used in the simulations.

Next we consider internal flow past a two-dimensional rounded plate in a channel. The meshes used are as shown in figure 2.15 and they consist of 544 and 936 elements; higher resolution requirements employed the fine mesh, while the coarser one was used in most 2-dimensional cases. The domain dimensions are $x \in [-2\pi, 2\pi], y \in [-1, 1]$, while the plate extends from $[-\pi, \pi]$ in the x-direction and $[-\frac{1}{10}, \frac{1}{10}]$ in the y-direction. The leading and trailing edges are complementing semicircles of radius $\frac{1}{10}$, as shown in Figure 2.16. The domain is considered periodic in the x-direction at $x = -2\pi, 2\pi$, while all other boundary conditions are represented by solid surfaces. The flow is driven by a constant body force $\mathbf{F} = (F_x, 0, 0)$.

The main challenge of the problem is the presence of the rounded edge followed by the upper and lower parts of the channel that re-define the Reynolds number of the domain through a half-height of 0.45 instead of 1 (the original value of the large channel). The periodic boundary conditions in the direction of the body force are also of interest, since all disturbances propagate in the

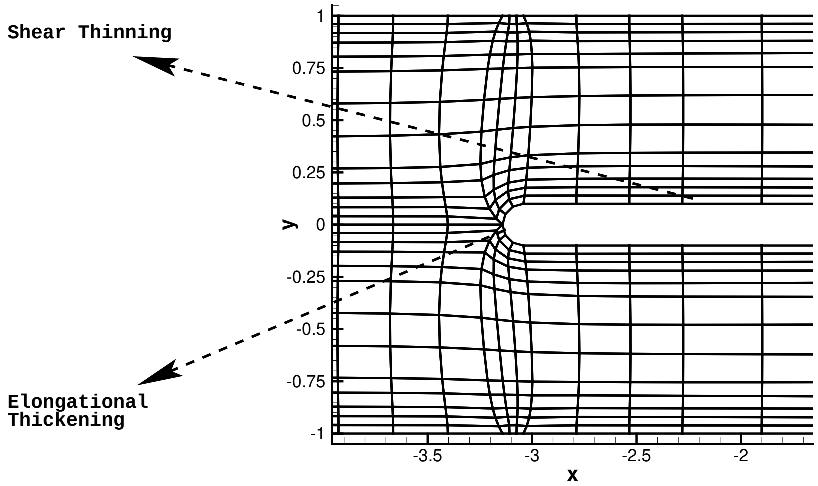

Figure 2.16: Close-up of the leading edge from the 936-element mesh, showing the semicircular edge. The rounded sides are represented by a high-order isoparametric expansion.

entrance of the domain at $x = -2\pi$. However, the biggest numerical challenge for viscoelastic fluids such as the FENE-P model in this setup is the presence of both elongational thickening and shear thinning in different parts of the domain - namely the leading edge for the former and the upper/lower channels for the latter (Figure 2.16). More specifically, denoting the shear rate by $\dot{\gamma}$ and the stretch rate by $\dot{\epsilon}$, the polymer-induced stresses σ, τ exhibit different power law scalings for finite extensibility models, namely

$$\dot{\epsilon} = \left|\frac{\partial u}{\partial x}\right| \quad \longrightarrow \quad \sigma_{\text{tip}} \sim \dot{\epsilon}$$

$$\dot{\gamma} = \left|\frac{\partial u}{\partial y}\right| \quad \longrightarrow \quad \tau_{\text{channel}} \sim (\dot{\gamma})^{\frac{1}{3}}$$

If λ denotes a characteristic polymer relaxation time, we define the Weissenberg number of the flow by $We = \frac{\lambda U_{\text{CL}}}{L}$, where U_{CL} is a typical value for the centerline velocity and L a typical length. The Reynolds number of the flow is defined as $Re = \frac{U_{\text{CL}} L}{\nu}$. Clearly, different parts of the domain have different typical values, and therefore different Weissenberg numbers define and dominate them. Figure 2.17 illustrates clearly the difficulties we face in such a geometry; the axial normal stress at the leading edge is one order of magnitude larger than that at other parts of the domain and this leads to numerical instabilities. Typical values for the simulation parameters (unless otherwise stated) are: the FENE-P maximum extensibility parameter $L = 10, 20$, the coupling parameter $\beta \in [0.97, 0.99]$, the kinematic viscosity $\nu = 6000$, the time-step $\Delta t = 5 \times 10^{-4}$, the polynomial spectral order $N = 7$, the relaxation time $\lambda \in [0.005, 0.1]$ and the forcing function $F_x = 15\nu$.

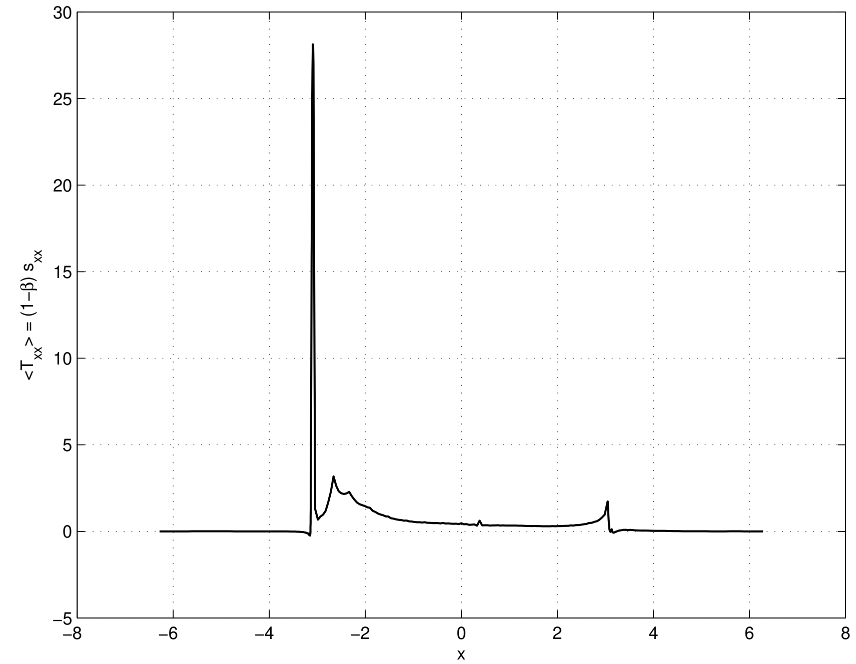

Figure 2.17: Averaged profile of the axial normal stress $T_{xx} = (1 - \beta)\tau_{xx}$ along the centerline of the domain and the surface of the plate.

In order to illustrate the fundamental differences in the value of We between two different parts of the domain, we calculate typical values of the Weissenberg number at the leading edge (We_{tip}) and the upper or lower sub-channels (We_{channel}). The radius of the semicircular tip is $R_{\text{tip}} = 0.1$, the big channel half-height $H = 1$, the sub-channel half-height $h = 0.45$ and a typical value for the centerline velocity in the whole domain is 0.6 (the channel and sub-channels have approximately the same centerline velocity in the $x-$direction). Therefore,

$$We_{\text{tip}} = \frac{\lambda U_{\text{CL}}}{2R} \sim 0.03, \qquad We_{\text{channel}} = \frac{\lambda U_{\text{CL}}}{H} \sim 0.006.$$

The computed values are small, and raise the question of whether the *elasticity* of the flow has indeed attained realistic values. The elasticity number El is defined as the ratio $\frac{We}{Re}$, and in our simulations it takes typical values of

$$\frac{1}{El} = \frac{Re}{We} = \frac{(2R)^2\rho}{\mu\lambda} = \frac{0.2^2 \times 6000}{\{0.01, 0.1\}} = \mathcal{O}(\{10^3, 10^4\})$$

Assuming that the leading and trailing edges of the plate operate locally as circular cylinders, this elasticity range is within the values presented in the experimental studies of Coelho and Pinho [54] done in 2003, who investigated the elasticity effects on the transition regimes of shear-thinning fluids past a circular cylinder.

The effect of the SVV amplitude on the solution T_{xx} profile is shown in Figure 2.18 for $\varepsilon = \{0.001, 0.01\}, M = 2$ and $N = 7$. Although the two ε values differ by one order of magnitude, the profile values show minimal disagreement, verifying the accuracy of the stability-preserving spectral filtering. The effect of the FENE-P maximum extensibility was also investigated for $L = 10, 20$ and Figure 2.19 shows a considerable rise of T_{xx} with an increase in L in the elongational thickening region (around $x = -\pi$). However, the effect is very small at the trailing edge. Lastly, investigating the effect of the relaxation parameter λ for the values $0.05, 0.1$, Figure 2.20 shows two time-averaged profiles of T_{xx} at both edges of the smooth plate. The leading edge and wake profiles of the axial normal stress rise with λ. It is interesting to note that in the Stokes case of the 2-dimensional cylinder, the dependence on λ was different.

2.5 Flat Plate in a Channel: Three-Dimensions

As a simple example of a three-dimensional case of a fully turbulent flow, we consider the rounded plate example extruded in the z-direction. The homogeneous z-direction is handled by the modified computer code $\mathcal{N}\varepsilon\kappa\mathcal{T}\alpha r$ with Fourier expansions, as opposed to the Jacobi-based expansion of the x- and $y-$ directions. Figure 2.21 shows an instantaneous snapshot of the streamwise

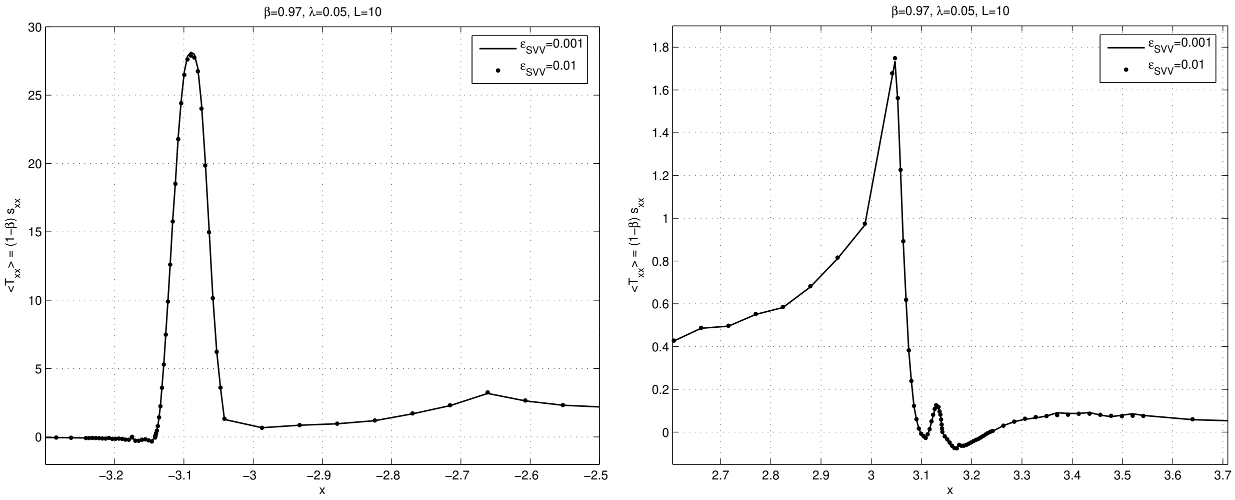

Figure 2.18: The effect of the SVV parameter ε on time-averaged values of the axial normal stress T_{xx} at the leading (left) and trailing (right) plate edges.

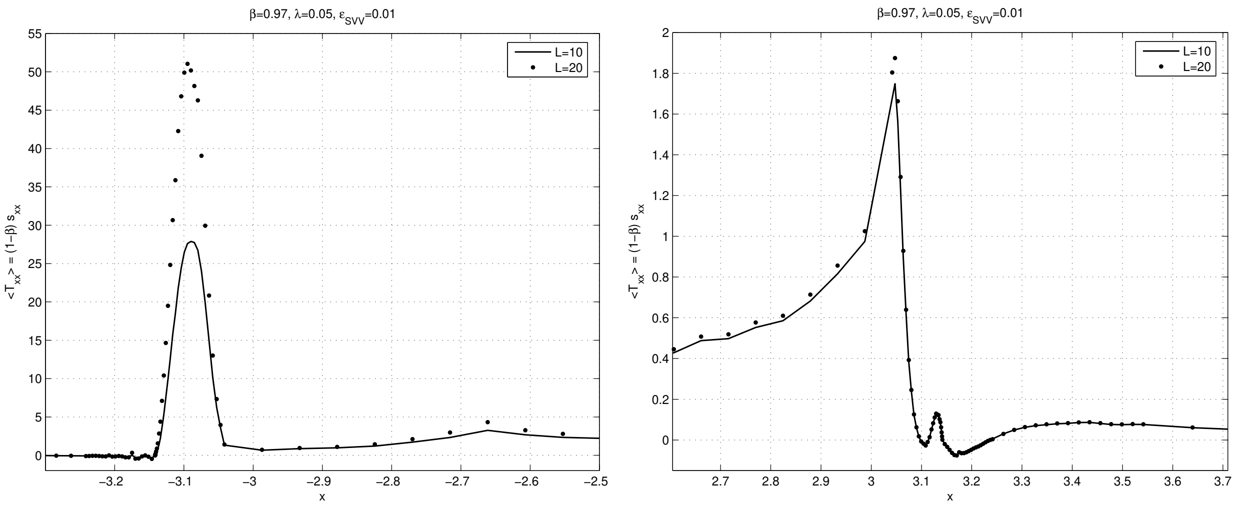

Figure 2.19: The effect of FENE-P maximum extensibility parameter L on time-averaged values of the axial normal stress T_{xx} at the leading (left) and trailing (right) plate edges.

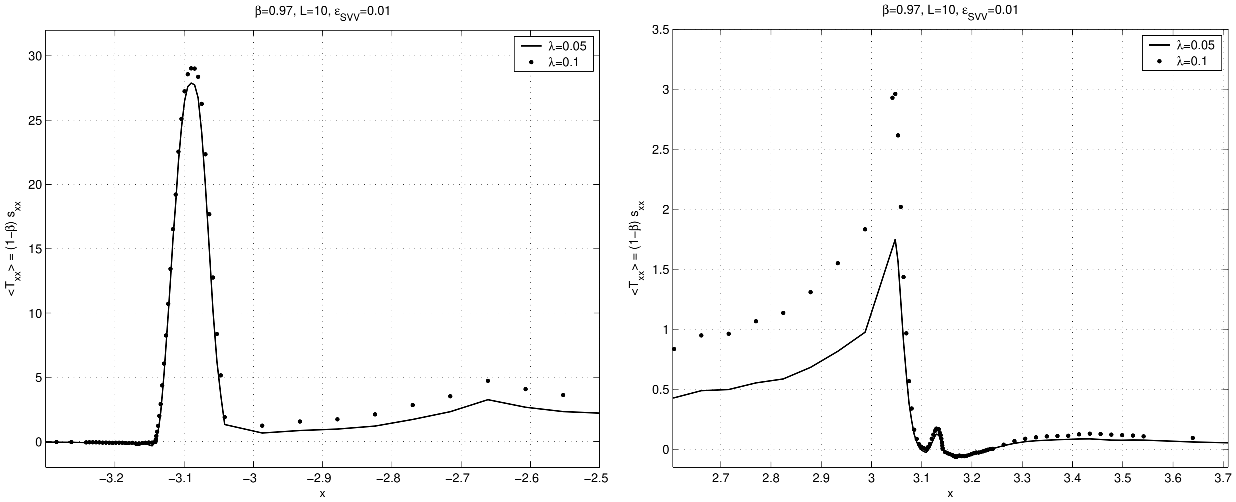

Figure 2.20: The effect of relaxation parameter λ on time-averaged values of the axial normal stress T_{xx} at the leading (left) and trailing (right) plate edges.

velocity contours at a friction Reynolds number $Re_\tau \sim 105$ in wall units, and a friction velocity $u_\tau \sim 0.0382$. Given the turbulent conditions and the numerical instabilities at $x \sim -\pi$ described in section 2.4, we have increased the coupling parameter to $\beta = 0.99$, i.e., almost Newtonian.

Figure 2.22 shows instantaneous slices of all six components of the stress tensor $\mathbf{s}$ at $y = 1.01$, i.e. $\sim 2\%$ of the half-channel height of the upper sub-channel. Figure 2.23 shows the mean, root-mean-square and skewness factor of the streamwise velocity component plotted against y. Denoting time- and $z-$averaging by an overbar, we define the quantities as follows:

$$\text{mean:} \quad u_{\mathrm{m}} = \frac{\bar{u}}{u_\tau} \tag{2.33}$$

$$\text{root-mean-square:} \quad u_{\mathrm{rms}} = \frac{\sqrt{\overline{(u-\bar{u})^2}}}{u_\tau} = \frac{\sqrt{\overline{u^2} - \bar{u}^2}}{u_\tau} \tag{2.34}$$

$$\text{skewness factor:} \quad S(u) = \frac{\overline{(u-\bar{u})^3}}{{u_{\mathrm{rms}}}^3} = \frac{\overline{u^3} - 3\overline{u^2}\bar{u} + 2\bar{u}^3}{{u_{\mathrm{rms}}}^3} \tag{2.35}$$

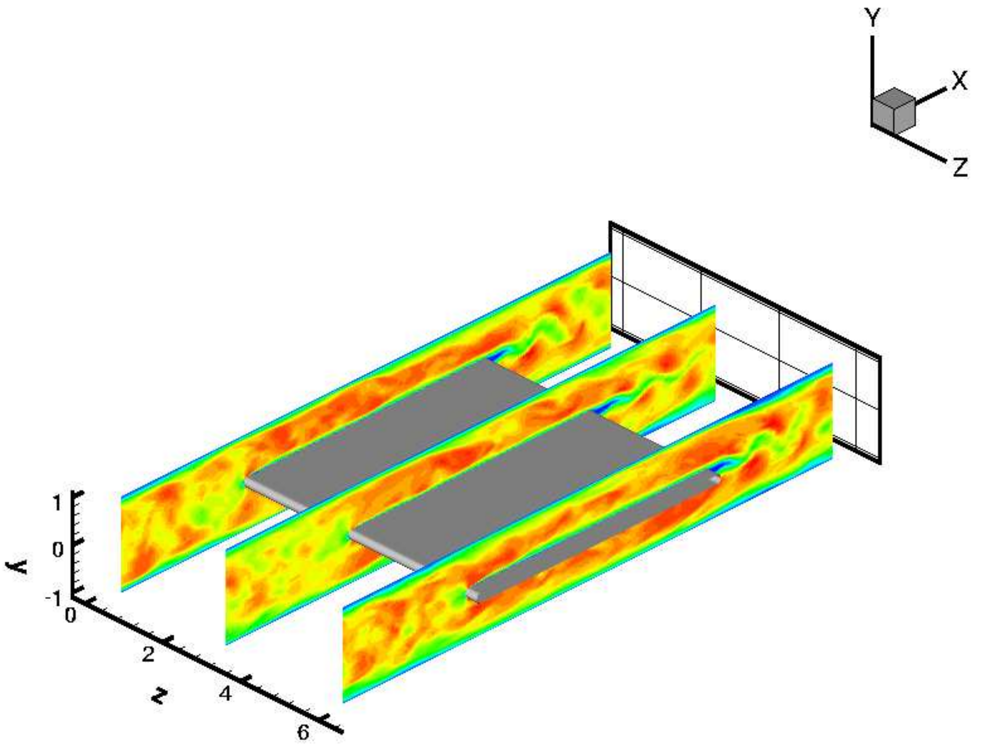

Figure 2.21: Instantaneous slices of streamwise velocity contours in turbulent flow regime ($Re_\tau \sim$ 105).

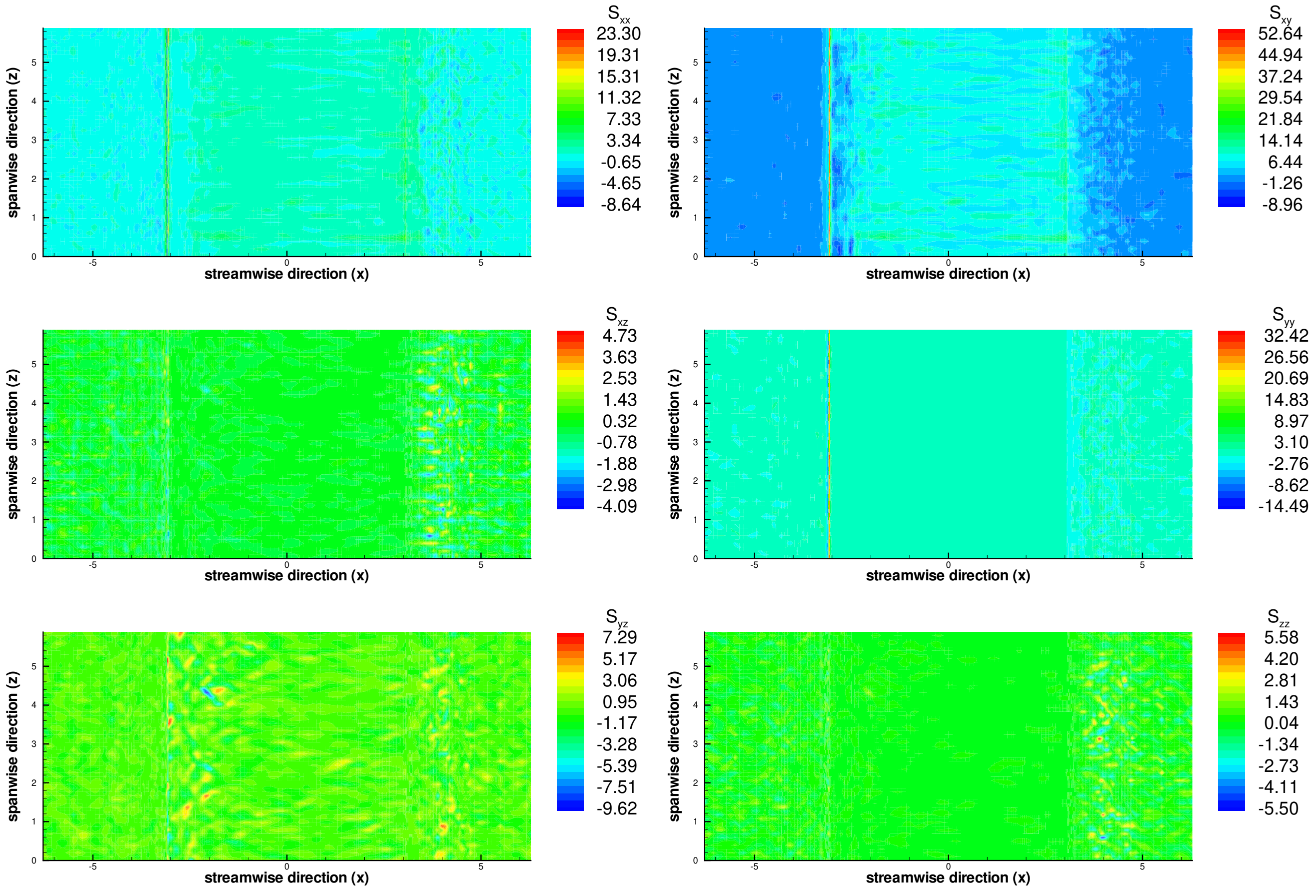

Figure 2.22: Instantaneous slices of all 6 components of the stress tensor **s** in turbulent flow regime.

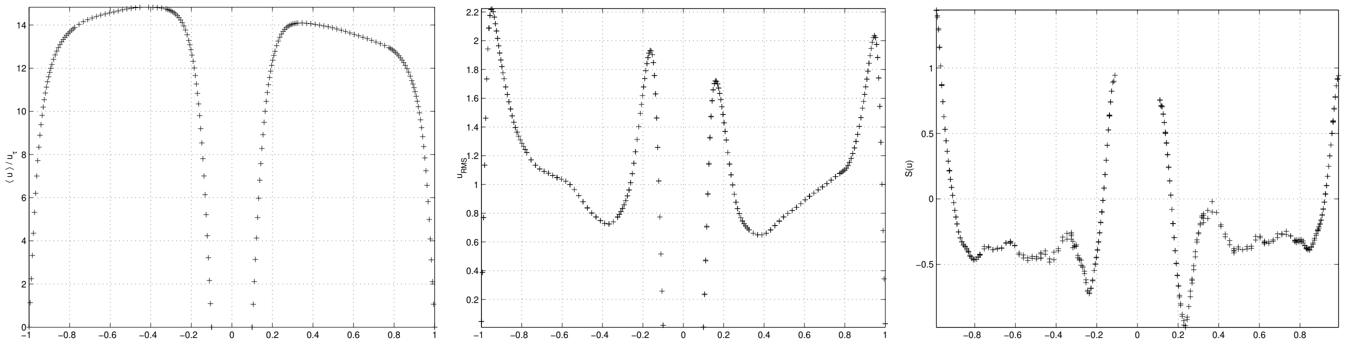

Figure 2.23: First (left), second (middle) and third (right) order time-averaged streamwise velocity statistics plotted versus y, gathered at $\{0, y, \langle z \rangle\}$ (i.e., averaged in the z-direction).

Chapter 3

The Reiner-Rivlin Model and the Hole Pressure Problem

3.1 Second-Order Fluids

Caswell's [55] three-dimensional analog of the Giesekus-Tanner (G-T) theorem allows the flow in the vicinity of a pressure tap to be analyzed with the solution of the inertialess flow of a Riener-Rivlin fluid just as Tanner & Pipkin [56] used G-T to analyze the corresponding two-dimensional flow with the Stokes solution. Kearsley [2] extended the Tanner & Pipkin analysis to the rectilinear flow in a channel with a parallel slot. In the two-dimensional case the hole pressure found by Tanner & Pipkin is independent of hole geometry and is relative to the Stokes value, usually neglected. In three-dimensions the Tanner & Pipkin term is again independent of hole geometry, but now is relative to the Reiner-Rivlin value which is not negligible. Hence the complete hole pressure in three-dimensions requires the solution of the Reiner-Rivlin problem. The latter is formulated for numerical simulation so that the hole pressure can be read off values of the pressure field without any post-processing calculation of velocity gradients. The numerical simulations were performed with a three-dimensional spectral element code [36] well suited to the efficient solution of flow problems in complex geometries. The limiting values of the hole pressure have been obtained for several hole sizes. Numerical results for large holes are not in agreement with the Higashitani-Pritchard [57] theory, and for such holes the Stokes hole pressure is large enough to be measurable.

3.2 Stress in Materially Steady Flows

In a previous article Caswell [55] defined the materially steady stress system in terms of the Reiner-Rivlin stress system. The name is motivated by the form of the stress for the simple fluid of Noll in the two important classes of materially steady flows:

1. Homogeneous, irrotational, isochoric flows (stretching flows),

2. Steady shear (viscometric) flows for which it reduces to the familiar CEF equation [58].

In isochoric flow the Reiner-Rivlin stress is an isotropic function of $\mathbf{A}$, twice the strain rate tensor, and is given by

$$\mathbf{R} = -\mathbf{1}P(II, III) + \eta(II, III)\mathbf{A} + \alpha(II, III)\mathbf{A}^2 \tag{3.1}$$

Here the scalar coefficients η and α are functions of II and III, the second and third invariants of $\mathbf{A}$ defined by

$$II = \frac{1}{2} tr\mathbf{A}^2, \qquad III = \frac{1}{3} tr\mathbf{A}^3 \tag{3.2}$$

The isotropic scalar pressure P is an arbitrary function of which a part may be expressed in terms of II and III and another part is to be determined by the solution of the equation of motion and the boundary conditions which define the flow problem.

Caswell [55] defines the materially steady stress $\mathbf{S}$ in terms of the Reiner-Rivlin stress $\mathbf{R}$ of equation 3.1, including the scalar pressure P, as

$$\mathbf{S} = \mathbf{R} - \mathcal{D}(\lambda(II, III)\mathbf{R})/\mathcal{D}t + \mathbf{1}\Psi \tag{3.3}$$

where λ is a scalar function of the indicated arguments, and Ψ is an additional isotropic stress which may be required to satisfy the equation of motion . The co-rotational time rate is denoted by $\frac{\mathcal{D}(*)}{\mathcal{D}t}$, and is clearly distinguishable from the material derivative denoted by an over dot. In steady viscometric flows $III = 0$, and the coefficients η, α and the factor λ are then functions of II alone. It is easily shown that equation 3.3 becomes the familiar CEF equation [58] with viscosity function $\eta(II)$, first normal stress coefficient $2\lambda(II)\eta(II)$ and second normal stress coefficient $\alpha(II) - \lambda(II)\eta(II)$.

Caswell [55] gave dynamical arguments for requiring two of the coefficients in equation 3.3 to be derivable from a strain-rate potential $\Phi(II, III)$ which delivers the coefficients of the Reiner-Rivlin stress as,

$$\lambda\eta \ = \partial\Phi/\partial II, \qquad \lambda\alpha = \partial\Phi/\partial III \tag{3.4}$$

where the time-function $\lambda(II, III)$ is an integrating factor. A further restriction, which follows from Theorem 3.2.1 below, is to set λ to be constant and to replace Φ with $\lambda\phi(II, III)$. The volume integral of $\phi(II, III)$ is the functional to be rendered stationary in the variational formulation [59] of the inertialess Reiner-Rivlin problem,

$$\nabla \cdot \mathbf{V} = \mathbf{0}, \qquad \nabla \cdot \mathbf{R} = \mathbf{0}, \qquad \nabla \times (\nabla \cdot \mathbf{R}) = \mathbf{0} \tag{3.5}$$

where the coefficients of the Reiner-Rivlin stress, equation 3.1, are given by

$$\eta \ = \partial\phi/\partial II, \qquad \alpha = \partial\phi/\partial III \tag{3.6}$$

The following statement of Caswell's [55] Theorem 1 summarizes the role of the Reiner-Rivlin stress in flows governed by the materially constant stress of equation 3.3:

Theorem 3.2.1 *Let* $\mathbf{V}$,P *be velocity, pressure fields, and let* $\mathbf{S}$ *be the materially constant stress* *of equation 3.3 with constant* λ *and with* $\Psi = \lambda\phi(II, III)/2$,

$$\mathbf{S} = \mathbf{R} - \lambda\left[\frac{\mathcal{D}\mathbf{R}}{\mathcal{D}t} - \frac{\mathbf{1}}{2}\phi(II, III)\right] \tag{3.7}$$

where $\mathbf{R}$ *is constructed from* $\mathbf{V}$,P *with equation 3.1. Then this stress system satisfies the inertialess flow or equilibrium equation and its compatibility condition,*

$$\nabla\cdot\mathbf{S} = \mathbf{0}, \qquad \nabla\times(\nabla\cdot\mathbf{S}) = \mathbf{0} \tag{3.8}$$

provided the following two conditions are met:

1. *The velocity-pressure fields* $\mathbf{V}$, P *satisfy the Reiner-Rivlin problem of equation 3.5 with variable coefficients* $\eta(II, III)$, $\alpha(II, III)$.

2. *The Reiner-Rivlin coefficients* $\eta(II, III)$, $\alpha(II, III)$ *are derivable from the derivatives of the strain-rate potential* $\phi(II, III)$ *according to equations 3.6.*

Tanner [60] proved a similar theorem for flows governed by the equilibrium of the CEF stress in the two-dimensional plane where $III = 0$, α plays no role and η is a function of II alone. In the limit of small strain rates, II, $III \to 0$ the coefficients η, α of equation 3.1 are constants, and the strain-rate potential becomes

$$\phi = \eta II + \alpha III \tag{3.9}$$

Theorem 3.2.1 reduces to Theorem 1a of Caswell [55] which is the three-dimensional generalization of the Giesekus-Tanner (G-T) theorem [61, 62]. The materially steady stress system 3.7 then becomes the augmented second order fluid,

$$\mathbf{S} = -\mathbf{1}\left[P - \lambda\dot{P} - \lambda\eta\frac{II}{2} - \lambda\alpha\frac{III}{2}\right] + \eta\mathbf{A} + \alpha\mathbf{A}^2 - \lambda\eta\frac{\mathcal{D}\mathbf{A}}{\mathcal{D}t} - \lambda\alpha\frac{\mathcal{D}\mathbf{A}^2}{\mathcal{D}t}. \tag{3.10}$$

This stress system is the complete second order fluid (SOF) system with three coefficients augmented by the last term of third order whose coefficient is a product of two coefficients of the SOF.

The G-T theorem is recovered either by setting $\alpha = 0$ in equations 3.9 and 3.10. The Reiner-Rivlin stress $\mathbf{R}$ of equation 3.1 reduces to the Newtonian stress, and the Reiner-Rivlin problem of equation 3.5 reduces to the Stokes problem. The power of G-T theorem is the prospect of obtaining the solution of a non linear problem from that of the corresponding linear one. Theorem 1a of [55] shows that in three-dimensions all that can be expected is a reduction of the order of spatial differentiation, which can have important advantages when numerical solutions are sought. It is clearly preferable to apply numerical methods to a problem defined by equation 3.5 instead of equation 3.8. This is the basis for the calculation of the limiting value of the three-dimensional hole pressure given below.

3.3 The Hole Pressure

A tap in the wall of a channel, Figure 3.1, gives rise to a small flow disturbance which in turn alters the pressure relative to its undisturbed value in the neighborhood of the tap. Deep within the hole this disturbance is known as the hole pressure, and is defined by Lodge & Vargas [4] as the difference of the normal tractions $\sigma_w = -P_1$ at the wall in undisturbed channel flow, and $\sigma_h = -P_2$ at the bottom of the hole respectively.

$$P_{\mathrm{H}} = \sigma_w - \sigma_h \tag{3.11}$$

The depth is large enough to guarantee hydrostatic conditions so that by equations 3.1 and 3.10 it follows respectively that both the $\mathbf{R}$-stress and the $\mathbf{S}$-stress become isotropic. The calculation of P_{H} is carried out in two steps:

1. The application of theorem 3.2.1 to obtain the part which is analytic and also independent of hole size,

2. The part which can be found only by solution of the Reiner-Rivlin problem and depends on the hole size.

The first step requires only that $\mathbf{S} - \mathbf{R}$ be considered. Far upstream in the channel the flow

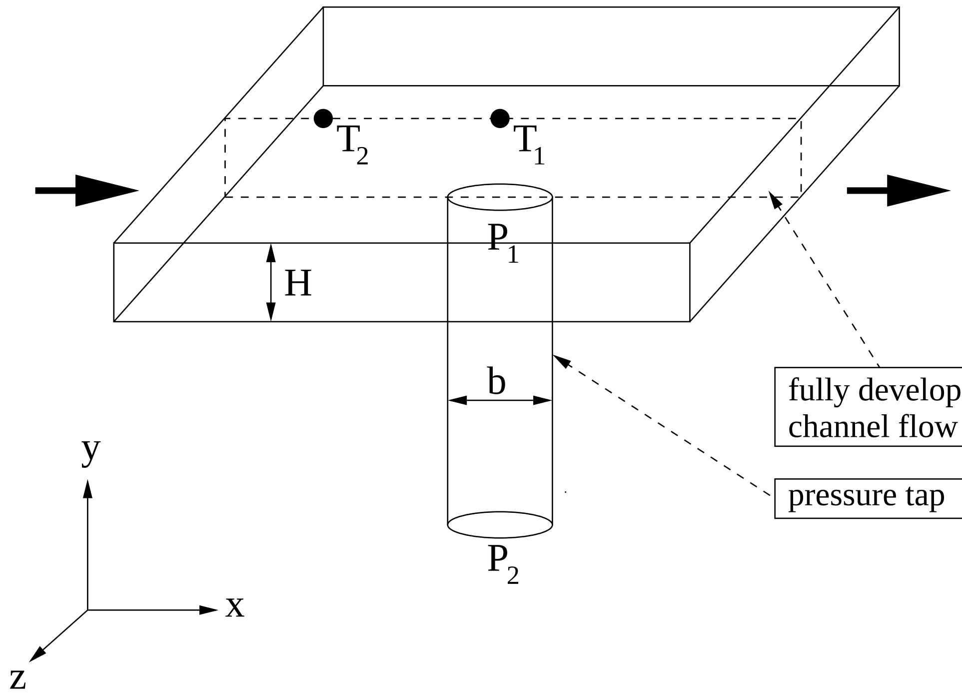

Figure 3.1: Channel with pressure tap. T_1 and T_2 indicate locations of pressure transducers in the stressmeter of Lodge & Vargas [4].

is exactly viscometric, and the stress is then given exactly by the materially constant stress of equation 3.3 which reduces to the CEF [58] equation in such flows. Let the velocity be $\mathbf{V} = u(y)\mathbf{i}$ relative to Cartesian coordinates x, y along and transverse to the streamlines respectively, and with z normal to the xy plane. The kinematical tensors of the materially constant stress system are evaluated in terms of the strain rate $\dot{\gamma} = \frac{du}{dy}$ as follows:

$$\mathbf{A} = (\mathbf{ji} + \mathbf{ij})\dot{\gamma}, \qquad \mathbf{A}^2 = (\mathbf{ii} + \mathbf{jj})\dot{\gamma}^2, \qquad \frac{\mathcal{D}\mathbf{A}}{\mathcal{D}t} = (\mathbf{jj} - \mathbf{ii})\dot{\gamma}^2, \qquad \frac{\mathcal{D}\mathbf{A}^2}{\mathcal{D}t} = 0, \tag{3.12}$$

and the invariants II, III are then $\dot{\gamma}^2, 0$ respectively. The stress system equation 3.1 is then

$$\mathbf{R} = -\mathbf{1}p + (\mathbf{ji} + \mathbf{ij})\tau + (\mathbf{ii} + \mathbf{jj})\sigma, \tag{3.13}$$

and from equation 3.3, $\mathbf{S} - \mathbf{R}$ becomes

$$\mathbf{S} - \mathbf{R} = \mathbf{1}(\lambda u p_x + \Psi) - \frac{1}{2}N_1\dot{\gamma}^2(\mathbf{jj} - \mathbf{ii}), \qquad \Psi = \frac{1}{2}N_1\dot{\gamma}^2 - \lambda u p_x \tag{3.14}$$

where $p_x = \frac{\partial p}{\partial x}$, $\tau = \eta\dot{\gamma}$, $\sigma = \alpha\dot{\gamma}^2$, $N_1 = 2\lambda\eta\dot{\gamma}^2$ is the first normal stress difference, and the coefficients η, α, and λ are now functions of II alone. The scalar Ψ is not known for general flows; in the Appendix of Caswell [55] it was shown that the form given in equation 3.14 holds in viscometric flow. Disturbed by the hole from the purely viscometric one, the flow is not easily calculated by direct solution of the equilibrium equation for typical constitutive equations. The materially constant stress 3.3 gives an approximate description of the stress in this nearly viscometric flow. However, the higher order spatial derivatives in equation 3.3 are well-known to be troublesome in numerical simulation. Hence a further simplification approximates the time function $\lambda(II, III)$ by a constant λ_c, and thereby reduces the flow problem to the solution of the lower-order Reiner-Rivlin problem 3.5 by means of Theorem 3.2.1. The constant λ_c is fixed in the far-upstream, viscometric region by equating the channel-wall, exact difference-stresses of equation 3.14 to the values given by the constant-λ approximation of equation 3.7. By use of equations 3.12 and 3.13 the latter becomes

$$\mathbf{S} - \mathbf{R} = \mathbf{1}\lambda_c(up_x + \frac{\phi}{2} + \frac{\phi_c}{2}) - \lambda_c\eta\dot{\gamma}^2(\mathbf{jj} - \mathbf{ii}), \tag{3.15}$$

ϕ_c is a constant which has no effect on the equilibrium equation 3.8, and the potential $\phi(\dot{\gamma}^2, 0)$ vanishes as $\dot{\gamma}^2 \to 0$. In viscometric flow Caswell [55] (see Appendix therein) showed that ϕ can be expressed in terms of the shear stress τ as

$$\frac{\phi(\tau)}{2} = W_R(\tau) - \int_0^{\tau} \frac{W_R(\tau')}{\tau'} d\tau', \qquad W_R = \tau\dot{\gamma} \tag{3.16}$$

Equations 3.14 and 3.15 have no off-diagonal components, and equality of their diagonal-components is satisfied by

$$\frac{\phi_c}{2} = \int_0^{\tau_w} \frac{W_R(\tau)}{\tau} d\tau, \qquad \lambda_c = \frac{N_1(\tau_w)}{2\tau_w\dot{\gamma}_w}, \tag{3.17}$$

where the subscript w denotes wall values in the viscometric domain far from the hole. Hydrostatic conditions at the bottom of a deep hole means the only non-zero term in equation 3.7 is the constant isotropic tension,

$$\mathbf{S} - \mathbf{R} = \mathbf{1}\frac{\lambda_c \phi_c}{2} = \mathbf{1}\int_0^{\tau_w} \lambda_c \frac{W_R(\tau)}{\tau} d\tau. \tag{3.18}$$

Lodge & Vargas [4] define the *hole pressure* as the wall value of the normal wall-stress in undisturbed plane Poiseuille flow minus the total stress deep inside the hole. From equations 3.15 and 3.17 the **jj**-component of the difference stress is zero on the wall, and hence the hole pressure in excess of the Reiner-Rivlin value is, in fact, the isotropic stress in equation 3.18. In the limit of small strain rates Theorem 3.2.1 reduces to Theorem 1a of [55], λ_c becomes the mean relaxation time of linear viscoelasticity and the integral 3.18 goes to the Pipkin-Tanner [56] limit of $\frac{N_1}{4}$

The complete hole pressure is obtained in step 2 by solution of the Reiner-Rivlin problem in the channel-with-hole geometry (Figure 3.1). In the formulation of the Reiner-Rivlin problem given below the pressure is modified so that equation 3.1 is replaced by

$$\mathbf{R} = -\mathbf{1}P + \eta\mathbf{A} + \alpha\left(\mathbf{A}^2 - \mathbf{1}II\right) \tag{3.19}$$

The effect of this pressure definition is that in plane flow the α term vanishes. In viscometric flow the stress component normal to the shear planes is $-P$, and since the pressure is a primitive variable in the numerical scheme the hole pressure given by equation 3.11 can be read off from the solution without spatial differentiation of the velocity field. In this work solutions have been obtained only for the small strain-rate limit where η and α are constant, and where dimensional analysis suggests the Reiner-Rivlin hole pressure P_{RR} should have the form

$$P_{\mathrm{RR}} = -P_{\mathrm{HS}} - r\alpha\dot{\gamma}_w^2, \tag{3.20}$$

where the Stokes ($\alpha = 0$) hole pressure P_{HS} and r are constant for every hole size. As defined, r is positive for all known cases. These are: $r = 0, \frac{1}{2}, \frac{1}{6}$ respectively for the transverse slot (Tanner & Pipkin [56]), the parallel slot (Kearsley [2]), and the circle (Higashitani & Pritchard [57]). The flow across the transverse slot is planar, and hence r is zero since the α-term vanishes from equation 3.19. Kearsley [2] showed that with a modified pressure field the velocity field for the rectilinear flow of a Newtonian fluid also satisfies the Reiner-Rivlin problem. The flow in the parallel slot is an example of a rectilinear motion, and it is used in this work as a benchmark for the numerical method. From equations 3.18 and 3.20, the total hole pressure in the limit of small strain rates can be written as

$$P_{\mathrm{H}} = \frac{N_1}{4} - r\left[\frac{N_1}{2} + N_2\right] - P_{\mathrm{HS}}, \tag{3.21}$$

where N_1 and N_2 are the first and second normal stress differences respectively.

3.4 The Reiner-Rivlin Stress in Nearly Incompressible Flows

In plane flows the Cayley-Hamilton theorem takes the form

$$\mathbf{A}^2 - [tr\mathbf{A}]\,\mathbf{A} + \left[\frac{1}{2}(tr\mathbf{A})^2 - II\right]\mathbf{1} = \mathbf{0}, \tag{3.22}$$

where $tr\mathbf{A} = 2\nabla\cdot\mathbf{V}$. It follows from equation 3.22 that for plane isochoric motions the flows of the Reiner-Rivlin fluid (equation 3.19) are indistinguishable from the corresponding flows of a Newtonian fluid with viscosity η . In numerical simulation incompressibility is nearly always imposed as a constraint, and consequently the calculated flow fields are nearly, but not exactly, isochoric. It is of interest to formulate the Reiner-Rivlin stress so that the α-term in equation 3.19 will produce dynamic effects only in three-dimensional flows regardless of compressibility. Since incompressibility is imposed as part of the solution of the equilibrium equation 3.5 the Reiner-Rivlin stress is formulated in terms of $\mathbf{A}$ modified by any multiple of $\nabla\cdot\mathbf{V}$. In terms of $\mathbf{B} = \mathbf{A} - (\nabla\cdot\mathbf{V})\,\mathbf{1}$ it is easily shown that the left hand side of equation 3.22 becomes

$$\mathbf{B}^2 + \frac{1}{2}\left[(tr\mathbf{B})^2 - tr(\mathbf{B}^2)\right]\mathbf{1}. \tag{3.23}$$

By design, $tr\mathbf{B}$ is zero in plane flow, and since the whole expression is also zero then $\mathbf{B}^2$ is isotropic in plane compressible flows just as $\mathbf{A}^2$ is isotropic in plane incompressible flows. With the pressure modified by $\frac{1}{2}\left[(tr\mathbf{B})^2 - tr(\mathbf{B}^2)\right]$ the Reiner-Rivlin stress (equation 3.1) is written with $\mathbf{A}$ replaced by $\mathbf{B}$, as

$$\mathbf{R} = -\mathbf{1}p + \eta\mathbf{B} + \alpha\mathbf{C}, \qquad \mathbf{C} = \mathbf{B}^2 + \frac{1}{2}\left[(tr\mathbf{B})^2 - tr(\mathbf{B}^2)\right]\mathbf{1}. \tag{3.24}$$

In principle, the solution of the dynamical equations rendered under an incompressibility constraint should yield essentially the same numerical result for the stress systems of equations 3.1 or 3.24. Numerical experiments on the parallel slot geometry have demonstrated that formulation 3.24 results in greater accuracy and improved convergence with respect to the magnitude of α.

In the numerical implementation described below, $\mathbf{C}$ is calculated from known velocity fields from its Cartesian components displayed in the Appendix. After a Galerkin projection onto element nodes these values are used to obtain $\nabla \cdot \mathbf{C}$ and $\nabla \cdot (\nabla \cdot \mathbf{C})$ which appear in the momentum and pressure equations respectively. Analytical expressions for the direct computation of these quantities are derivable by use of the following identities for the components of the strain rate $\mathbf{A}$:

$$\begin{aligned} a_{ij} &= v_{i,j} + v_{j,i} = \epsilon_{jik}\omega^k + 2v_{j,i} = \epsilon_{ijk}\omega^k + 2v_{i,j} \quad , \\ \omega^k &= \epsilon^{kmn} v_{n,m}. \end{aligned} \tag{3.25}$$

Here ϵ_{ijk} is the alternator and the ω^k are the components of the vorticity vector $\boldsymbol{\omega}$. When these identities are employed in the definition of $\mathbf{B}$, the components of $\mathbf{C}$, constructed from equation 3.24, can be expressed in the form

$$C_i^k = -\omega^k\omega_i + 2(v^j_{,i}v^k_{,j} + v_i^{,j}v_j^{,k} - v^j_{,j}a_i^k) - 2\delta_i^k(v^j_{,k}v^k_{,j} - v^j_{,j}v^k_{,k}), \tag{3.26}$$

where δ_i^k is the Kronecker delta. Equations A.5 of the Appendix are recovered when the components 3.26 are written in Cartesian coordinates. The vorticity product terms are easily identifiable, and it then follows that the remaining terms appear in equations A.5 as sums of 2×2 Jacobians. The divergence of $\mathbf{C}$ can be derived from equation 3.26 and expressed in condensed notation as

$$\nabla \cdot \mathbf{C} = -\boldsymbol{\omega} \cdot \nabla \boldsymbol{\omega} - 2\nabla \times (\nabla \mathbf{V} \cdot \boldsymbol{\omega}), \tag{3.27}$$

which is easily shown to vanish in any plane flow independent of the magnitude of $\nabla \cdot \mathbf{V}$. From equation 3.27 the divergence of $\nabla \cdot \mathbf{C}$ is

$$\nabla \cdot (\nabla \cdot \mathbf{C}) = -\nabla \boldsymbol{\omega} : \nabla \boldsymbol{\omega}. \tag{3.28}$$

Although equation 3.28 is derived from equation 3.27 by an additional spatial differentiation the highest order of differentiation of the velocity field is the same in each, and again this result is independent of the magnitude of $(\nabla \cdot \mathbf{V})$.

3.5 Numerical Method

The momentum equation for the Reiner-Rivlin fluid with constant coefficients takes the dimensionless form

$$\frac{\partial \mathbf{u}}{\partial t} + Re\,[\mathbf{u} \cdot \nabla \mathbf{u}] = -\nabla p + \nabla^2 \mathbf{u} + \alpha' \nabla \cdot \mathbf{C} + \mathbf{F}, \tag{3.29}$$

where $\mathbf{F}$ denotes the body force vector, $\mathbf{u}$ the velocity vector and $\mathbf{C}$ is defined by equation 3.24. The Reiner-Rivlin number $\alpha' = \frac{\alpha \dot{\gamma}_w}{\eta}$ is a Deborah number which measures the strength of the non-Newtonian stress contribution, while the Reynolds number $Re = \frac{\dot{\gamma}_w b^2}{4\nu}$ measures the inertial disturbance due to the hole of diameter b. In view of Theorem 3.2.1 the Reynolds number will be set to zero in all the simulations presented below. The solution is obtained by marching in time to the steady state from a known initial state, and hence the scale of the dimensionless time t is determined by the magnitude of the time step.

For the *temporal discretization* of the Navier-Stokes equations we use the time-splitting stiffly-stable scheme described in section 2.2. The version of the implemented scheme has the same structure as the one used for the FENE-P case, with the following distinct differences:

1. The non-linear step differs from the viscoelastic case in the right-hand side, due to the presence of the Reiner-Rivlin stress. Hence the equation reads now

$$\hat{\mathbf{u}} = \sum_{q=0}^{J_u-1} \alpha_q \mathbf{u}^{n-q} + \Delta t \sum_{q=0}^{J_u-1} \beta_q \left[-(\mathbf{u}^{n-q} \cdot \nabla)\mathbf{u}^{n-q} + \alpha' \nabla \cdot (\mathbf{C})^{n-q} + F^{n-q} \right]. \tag{3.30}$$

   We note the difference in the polymeric stress; $\nabla \cdot \mathbf{C}$ replaces the viscoelastic $\nabla \cdot \mathbf{s}$ term of the FENE-P stress. The pressure and viscous steps are the same as the FENE-P case.

2. The Reiner-Rivlin stress is purely a function of the velocity components and no evolution equation for the polymeric stress exists. In absence of a conformation tensor, the SVV (whenever used) filters the velocity components instead.

The spatial discretization is identical to the FENE-P case, see section 2.2.

3.6 Convergence Studies

3.6.1 Simulations without Stabilization

Since the Reiner-Rivlin (R-R) fluid contains high-order derivatives, we need to address the problem of discontinuity across elemental boundaries as well as the effect of the R-R parameter α' on the accuracy of the computed solution. To this end we perform an analytical study of a simple plane channel flow with a given velocity distribution taking the form

$$\mathbf{U}(y,z) = \begin{pmatrix} (1-z^2)cos(\pi y) \\ 0 \\ 0 \end{pmatrix}. \tag{3.31}$$

The body force sustaining such a flow profile is given by

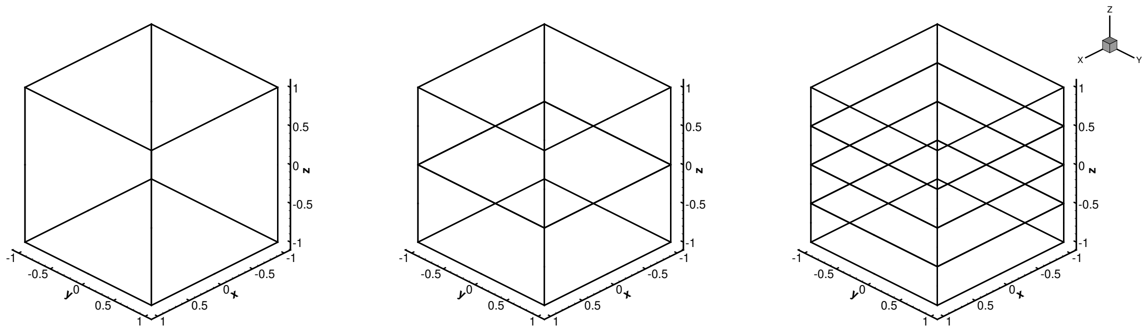

Figure 3.2: The 1-, 2- and 4-element meshes used for the convergence studies of the R-R fluid. Each hexahedral element has a 10^{th} order Jacobi polynomial approximating the solution in all 3 directions.

$$\mathbf{F}(y,z) = \begin{pmatrix} \nu cos(\pi y)(2+\pi^2-\pi^2 z^2) \\ -\pi\alpha' sin(2\pi y)(1+z^2) \\ -2\pi^2\alpha' z(1-z^2) \end{pmatrix}. \tag{3.32}$$

A notable point regarding the above combination of $\mathbf{U}(y,z), \mathbf{F}(y,z)$ is that although the flow is 1-dimensional it requires a 3-dimensional body force, rendering the computation non-trivial and hence meaningful for convergence study purposes. Another interesting aspect of the above solution is the α'-dependence of components y, z of the forcing function but *not* of the x-component. We examine the L_∞ error of all velocity components and of the pressure versus α' in figure 3.3. We observe a clear monotonic dependence of the error on α', but the effect of elemental boundaries has a secondary effect on the accuracy of the computed solution. The pressure error is 2 orders higher than the velocity error and this trend is consistent for all examined values of α'. For $\alpha' \approx 0.4$, a value larger than the ones we will be considering in the following sections, the pressure error is $\mathcal{O}(10^{-3})$. The introduction of more elements causes the simulation to diverge in the higher α' values (the elemental boundary discontinuities *do* affect stability), but when solutions converge accuracy is maintained at the same levels regardless of the number of elements.

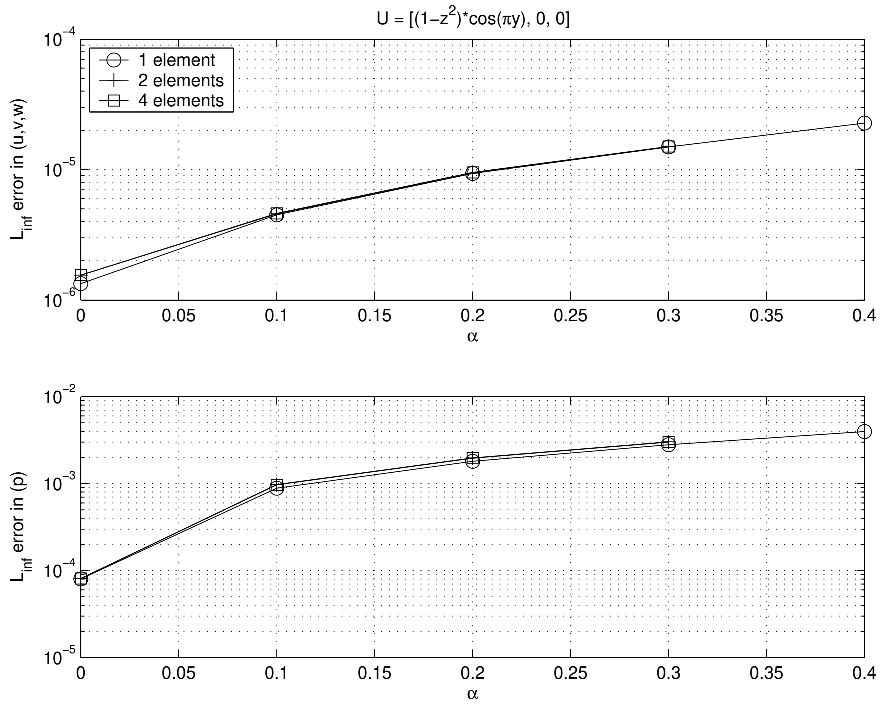

Figure 3.3: L_∞ error in the velocity (upper) and pressure (lower) plotted against the Deborah number α' for 1-, 2- and 4-element meshes.

3.6.2 Polynomial Over-Integration and SVV

Nonlinearities in the R-R equations appear both in the convective $\mathbf{u}\cdot\nabla\mathbf{u}$ and the stress $\nabla\cdot\mathbf{C}$ terms. In spectral/*hp* methods errors occur from insufficient quadrature of collocation when primitive variables are in physical space, in our case during the nonlinear step before the transform to modal space. For the integration of a polynomial $u(\xi)$ of degree N we require $(N+3)/2$ Gauss-Lobatto-Legendre quadrature points for exact computation of the integral. The decomposition of $u(\xi)$ is done using the basis functions $\phi_i(\xi)$; hence since $u(\xi) = \sum_{i=0}^{N} \hat{u}\phi_i(\xi)$ the inner product $\langle\phi_i(\xi)\phi_j(\xi)\rangle$ is of interest due to the Galerkin projection. Letting $M = N+1$ be the number of modal coefficients for the polynomial expansion of $u(\xi)$, the quadratic nonlinearity of the $\mathbf{u}\cdot\nabla\mathbf{u}$ term involves numerical computation of a polynomial of degree $3N$, and hence the minimum sufficient number of quadrature points is

$$Q_{3\mathrm{N}} = \frac{3N+3}{2} = \frac{3(M-1)+3}{2} = \frac{3M}{2}. \tag{3.33}$$

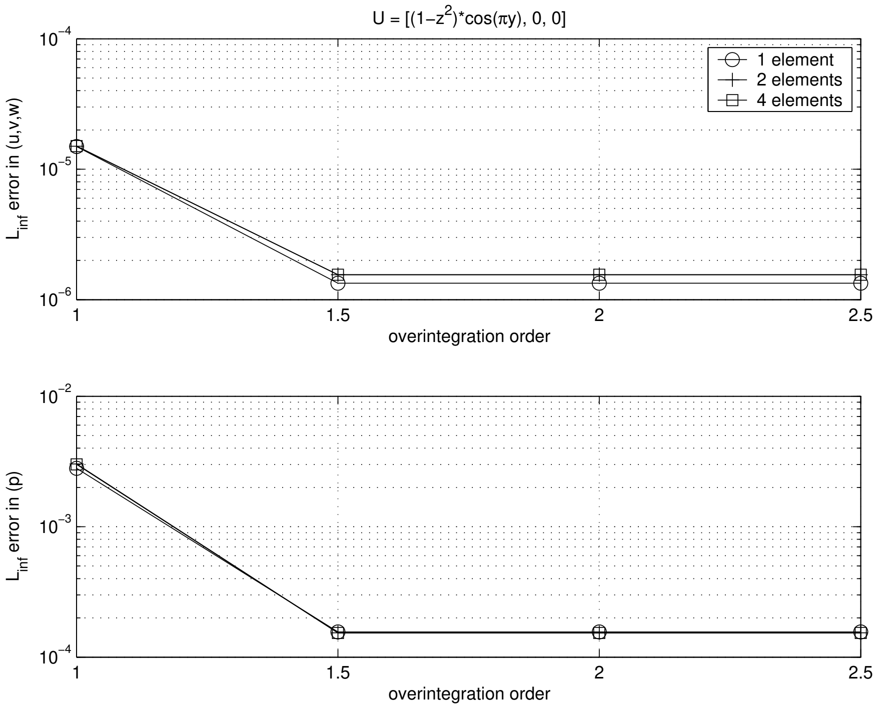

Figure 3.4: L_∞ error in the velocity (upper) and pressure (lower) plotted against the overintegration order for 1-, 2- and 4-element meshes.

Studies of this *over-integration* approach have been presented in [49] for the viscous Burger's equation; in this work we extend the study to the second order fluid. Figure 3.4 shows the effect of the over-integration order (defined as the multiplicative factor of M in the right-hand side of 3.33) on the L_∞ error of the velocity and pressure for the analytical solution and sample meshes presented earlier. The quadratic nonlinearity of both the convective and R-R terms is accurately resolved with the *three-halves* rule; accuracy is increased by one order of magnitude in the velocity and pressure for all studied meshes by simply using $\frac{3M}{2}$ modes in the nonlinear computations. The saturation of the error in the plot suggests that there is no numerical advantage in using more; curiously, though, the accuracy in the pressure is two orders of magnitude worse than that of the velocity components. This is true for the case of $\alpha = 0$, indicative that the non-Newtonian effect is not responsible. Possible reason might be the use of the L_∞ norm in our study.

Applying the SVV filtering in the case of the two-element mesh, managed to increase the range of Deborah numbers shown in Figure 3.3 to $\alpha' = 0.4$. Naturally, the use of the spectral filtering trades accuracy for stability and the corresponding errors for $(\varepsilon, M) = (1.0, 3)$ in the velocity components and pressure are $L_\infty = 0.0029$ and 0.3190, respectively.

3.7 Benchmark Problem: Parallel Slot

Kearsley [2] showed that the non-planar rectilinear flow with velocity components $\{u(y,z), 0, 0\}$, and driven by a constant pressure gradient $\{P_x, 0, 0\}$ also satisfies the equilibrium problem for the Reiner-Rivlin stress with constant coefficients provided the pressure is defined appropriately. On one wall of a channel the center plane of a deep slot extends along the entire x-axis giving the channel a constant *T-shaped* cross-section, Figure 3.5. The flow problem is solvable in the $y, z-$plane, but for the purposes of validation of the numerical code it was solved as a three-dimensional problem in a channel of finite length. Periodic boundary conditions were applied at the ends to simulate a channel of infinite length. The hole pressure was obtained, and the results are displayed in Figure 3.5.

Meshes with rounded corners and sharp corners at the slot junction were used. The rounded corners gave r-values in closest agreement with Kearsley's [2] analytical value for deep, narrow holes. Here the slot width was $\frac{H}{10}$. The Jacobi polynomial order p was varied and the r-values of Figure 3.5 show that little it gained for $p > 3$. In fact, the plot suggests there is no convergence with $p-$refinement. The sharp corners in the domain are responsible for this numerical inconsistency, and combined $h/p-$refined studies are under way, since it has been observed that $p-$refinement alone in domains with singularities is not sufficient.

Figure 3.6 shows the effect of over-integration and SVV filtering on the r-values for the round-edged slot. Over-integration effects are small in the given geometry for both accuracy and stability; SVV, however, proves to enhance stability for appropriate amplitudes ε. The results we provide use different SVV parameters for different values of α', as shown in table 3.1. Naturally, larger α' values require stronger filtering, a property that manifests itself in the corresponding significant

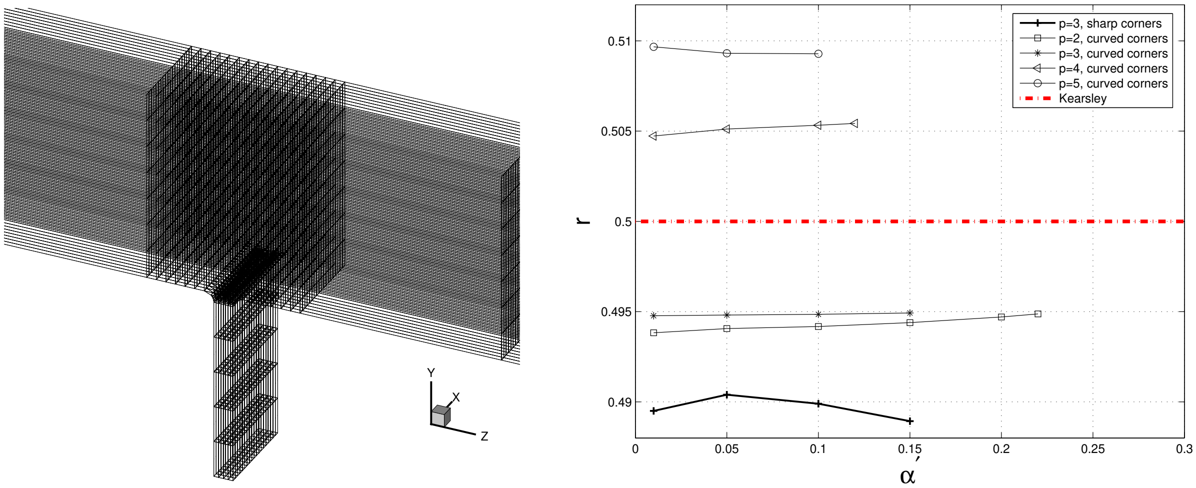

Figure 3.5: The mesh used for the rounded T-shaped cross-section (left) and the corresponding results $\frac{P_{\mathrm{RR}}}{\alpha\dot{\gamma}^2}$ plotted versus the R-R number α' (right).

$p=2$	$\alpha' \in [0.001, 0.16]$	$\alpha' = 0.17$	$\alpha' = 0.2$
	$(\varepsilon, M) = (0.006, 2)$	$(\varepsilon, M) = (1.0, 2)$	$(\varepsilon, M) = (2.5, 2)$

$p=3$	$\alpha' \in [0.001, 0.12]$	$\alpha' = 0.15$
	$(\varepsilon, M) = (0.006, 2)$	$(\varepsilon, M) = (1.2, 2)$

Table 3.1: Different SVV parameters used for stabilization of different Deborah numbers in the Reiner-Rivlin problem described by Kearsley [2].

increase of the SVV amplitude ε for higher values of α'. We note that all cases studied with $\alpha' > 0.16$ (for $p=2$) and $\alpha' > 0.12$ (for $p=3$) diverge if SVV is not used. The sudden drop in r with the use if SVV is not surprising, since the damping amplitude ε is increased by 3 orders of magnitude to achieve stability (Table 3.1), and accuracy is clearly affected under these conditions.

3.8 The Hole Pressure for Newtonian Fluids

3.8.1 Laminar Hole Pressure for a Newtonian Fluid

The hole pressure is the disturbance to the manometric pressure resulting from the presence of a pressure tap on the wall of a channel as depicted in Figure 3.1. It is the manometric measurement error incurred when the hydrostatic pressure deep within the tube is taken to be the *wall-pressure*, i.e., the negative of the total normal traction.

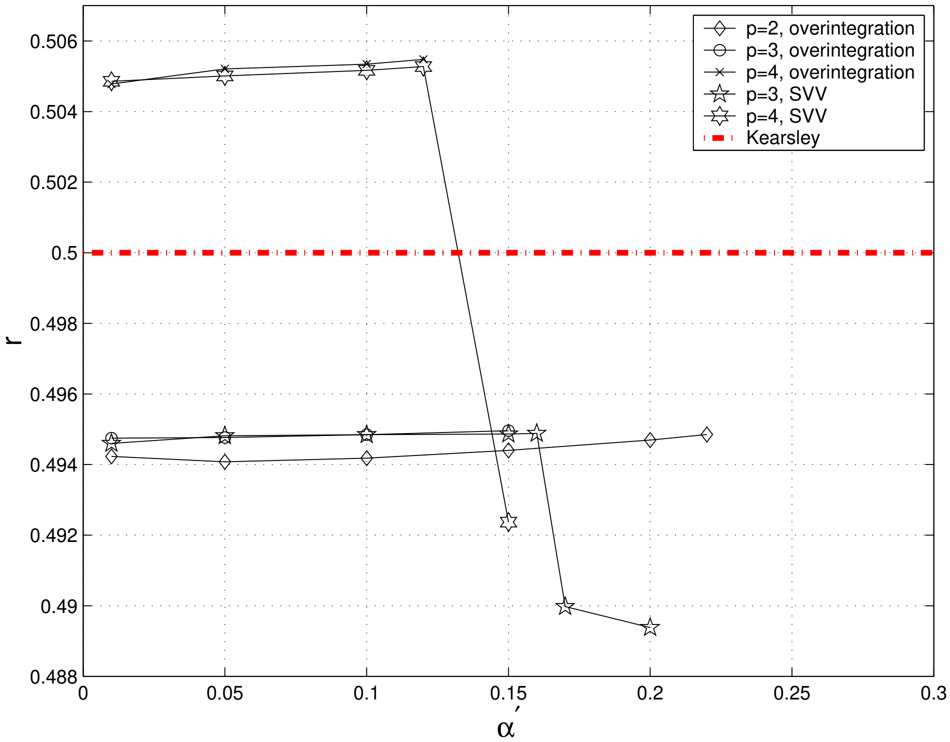

Figure 3.6: $\frac{P_{\mathrm{RR}}}{\alpha\dot{\gamma}^2}$ plotted versus the R-R number α' and compared with Kearsley's [2] analytical result for different polynomial orders using over-integration and SVV.

For non-Newtonian fluids the hole pressure is related to the two normal stress differences and is thought to be nearly independent of the hole size. Potentially, the effect provides a method to measure a combination of the normal stress differences, and hence is not considered to be an error [4]. This work investigates both the Newtonian and non-Newtonian cases (for the latter, see section 3.9.1). In most applications, the hole size relative to the channel dimension, wall curvature, or other geometric lengths are assumed to have a negligible effect on the hole pressure. Here, this assumption is investigated through flow calculations for two hole sizes, and it is shown that for hole sizes used in some experimental work the size effect is substantial. The calculations reported in this work demonstrate that pressure taps give rise to two global effects, namely:

1. The manometric error due to the flow disturbance caused by the hole, i.e., the hole pressure.

2. The pressure recovery in the channel due to the hole. This recovery of pressure is positive at small Reynolds numbers and becomes negative as inertia is increased.

Both of these quantities are consequences of the disturbance to the flow caused by the perturbation of the channel geometry due to the tap. Hence, the pressure field of interest will usually be the disturbance pressure. The undisturbed pressure field consists of the linear Poiseuille field in the channel and a uniform constant pressure in the hole; the constant being the Poiseuille value at the streamwise position of the hole axis. The undisturbed field can be considered an initial condition in which a membrane is placed across the mouth of the hole to isolate the two regions. At time zero, the membrane is removed and the flow evolves to a new steady state. The disturbance pressure field is the *difference* between the new steady state pressure field and the initial or undisturbed field. Since most of the discussion focuses on the disturbance pressure, it will be referred to as simply the "pressure", unless otherwise noted. In Stokes flow, the plane normal to the flow direction, coincident with the axis of the hole, is a plane of fore-aft symmetry for the streamlines, and anti-symmetry for the isobars. It follows that the hole pressure is one-half the pressure recovery in the channel (see Figure 3.9). This provides a consistency check for the calculations.

For the Newtonian fluid, dimensional analysis of the hole pressure problem depicted in Figure 3.1 gives

$$\frac{P_H}{\tau_w} = f(Re, \frac{b}{H}) \tag{3.34}$$

$$Re = \frac{\dot{\gamma}_w b^2}{4\nu} = \frac{\tau_w b^2}{4\mu\nu}, \tag{3.35}$$

where $\dot{\gamma}_w$ and $\tau_w = \mu\dot{\gamma}_w$ are wall values of the shear rate and the shear stress respectively for the undisturbed channel flow. The channel width is H and hole diameter is b. The hole is deep enough to ensure stagnant conditions for all channel flow rates of this study, and hence its depth is not a relevant parameter. The fluid has shear viscosity μ and kinematic viscosity ν. The hole pressure is defined as the difference of the normal tractions σ_w at the wall (undisturbed channel flow) and σ_h at the bottom of the hole, respectively:

$$P_H = \sigma_w - \sigma_h. \tag{3.36}$$

This definition gives a positive hole pressure for small Reynolds numbers for both Newtonian and non-Newtonian fluids. The relevant measure of inertial effects is the *hole Reynolds number* defined in equation 3.35, which vanishes as the hole size $b \to 0$. In that limit, the motion reduces to undisturbed, plane Poiseuille flow. The channel Reynolds number is not a relevant parameter, since the flow is assumed to be laminar. The numerical method is the same as the one described in section 3.5 with $\alpha' = 0$ in equation 3.29.

3.8.2 Numerical Results for Three-Dimensional Holes: Newtonian Fluid

Figure 3.7 shows plots of hole pressure vs. Reynolds number for two hole sizes; $b = H$ and $b = H/2$. The former appears to be unusually large, but was chosen because of available experimental data [63], which are displayed with the calculated curves in the figure (upper). Two sets of calculated curves are shown in both plots. The solid line represents the hole pressure with σ_w in equation 3.36 taken as the undisturbed, Poiseuille normal wall-traction at the center point of the hole. The dashed curve is constructed by taking the σ_w to be the normal wall-traction, for the disturbed flow, at the point of intersection of the hole axis with the wall opposite the hole. Figure 3.8 shows both hole pressure curves relative to the Stokes values (i.e. $(P_H - P_{HS})/\sigma)$ collapsed in one plot. From the experimental data of Tong [63], Lodge & Vargas [4] fitted a slope of 0.024 for circular holes with $b = H$; the straight line in Figure 3.8 has slope ≈ 0.027.

Tong's [63] experimental design assumes the pressure disturbance to be confined to the near-hole region, and that the normal traction on the opposite wall is essentially the undisturbed Poiseuille value; hence the location of the flush-mounted pressure transducers shown in Figure 3.1. The misconception of this assumption is clarified by the calculated results displayed in Figures 3.9 and 3.10, which show the disturbance pressure for Stokes flow for $b = H$. Figure 3.9 is the pres-

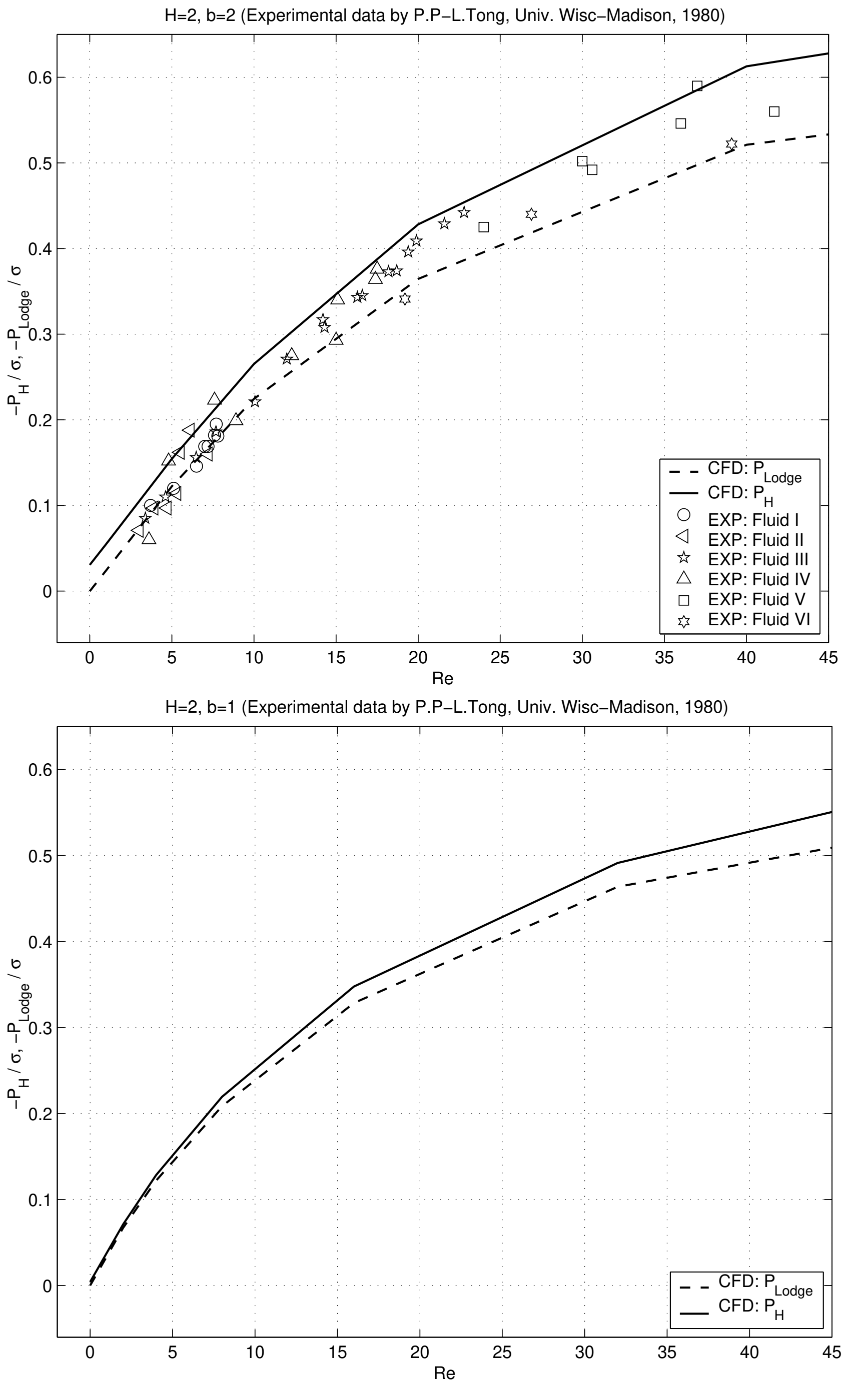

Figure 3.7: Hole pressure versus Reynolds number for 1:1 ($b = H$, upper) and 2:1 ($2b = H$, lower) ratios. Points represent experimental measurements.

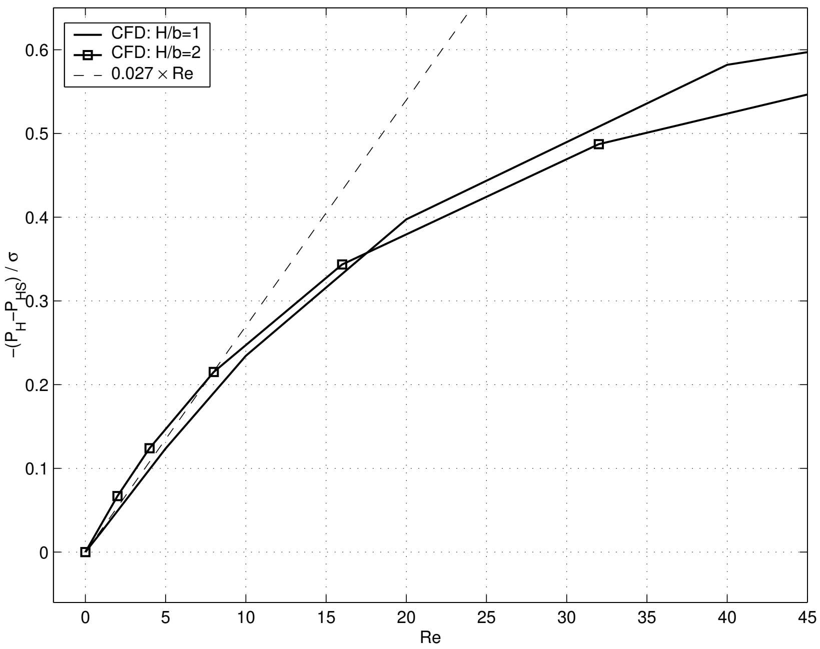

Figure 3.8: Hole pressure relative to Stokes versus Reynolds number for 1:1 and 2:1 ratios. Straight line represents tangent at $Re = 0$. Experimentally, Lodge & Vargas [4] fitted a slope of 0.024.

sure profile in the streamwise center plane $(x, \pm 1, 0)$ on the top and bottom channel walls, while Figures 3.10 and 3.11 display contour plots of the pressure on the upper and lower channel walls $(x, \pm 1, z)$. These results show that for large holes the pressure traverses the channel gap and the channel width with little attenuation. The peaks in the vicinity of the hole are smoothed out, but the ramp-like increase is projected across the gap and laterally across the full width of the channel. Figure 3.11 corresponds to Figure 3.10 for $Re = 20$ and shows the development of the pressure wake as inertia increases.

Contour plots of all three velocity components u, v, w at $(x, -1, z)$ for Stokes flow and $Re = 64$ (Figures 3.12, 3.13 and 3.14, respectively) show visible symmetry-breaking effects of inertia along the x-direction. Figure 3.15 shows the central-plane pathlines in the vicinity of the hole for Stokes flow and $Re = 20$. The secondary flow near the bottom of the hole is very much weaker than the upper one, and gives rise to a negligible pressure over the hydrostatic value at the bottom. A view from top in Figure 3.16 reveals visible inertia effects on the near-wall streamlines above the

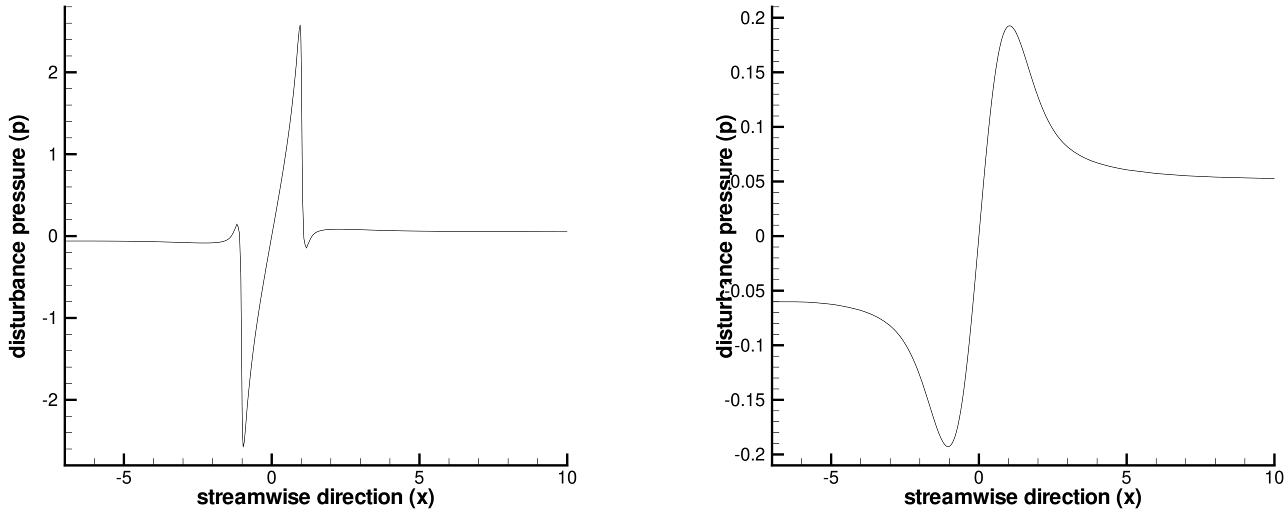

Figure 3.9: Streamwise pressure profiles in center plane for hole of ratio 1:1 ($b = H$) on the lower ($\{x, y, z\} = \{x, -1, 0\}$, left) and upper ($\{x, y, z\} = \{x, 1, 0\}$, right) walls; $Re = 0$.

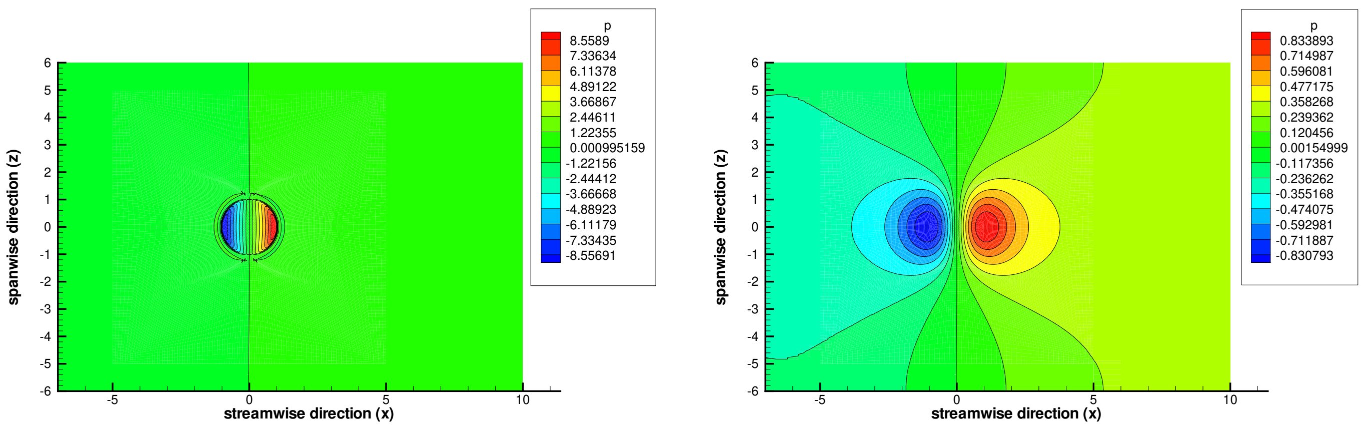

Figure 3.10: Pressure distributions on lower ($\{x, y, z\} = \{x, -1, z\}$, left) and upper ($\{x, y, z\} = \{x, 1, z\}$, right) walls; $Re = 0$, $H/b = 1$.

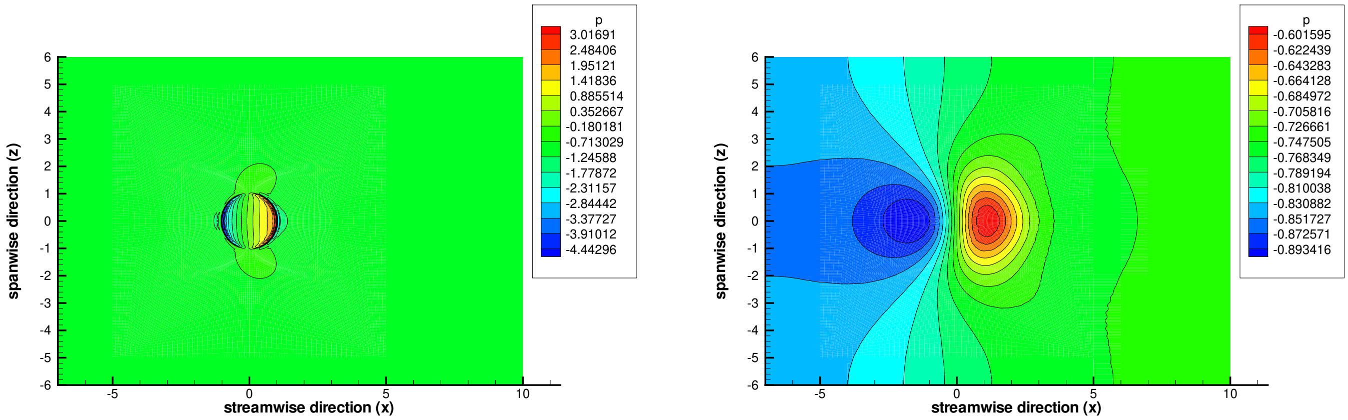

Figure 3.11: Pressure distributions on lower ($\{x, y, z\} = \{x, -1, z\}$, left) and upper ($\{x, y, z\} = \{x, 1, z\}$, right) walls; $Re = 20$, $H/b = 1$.

hole.

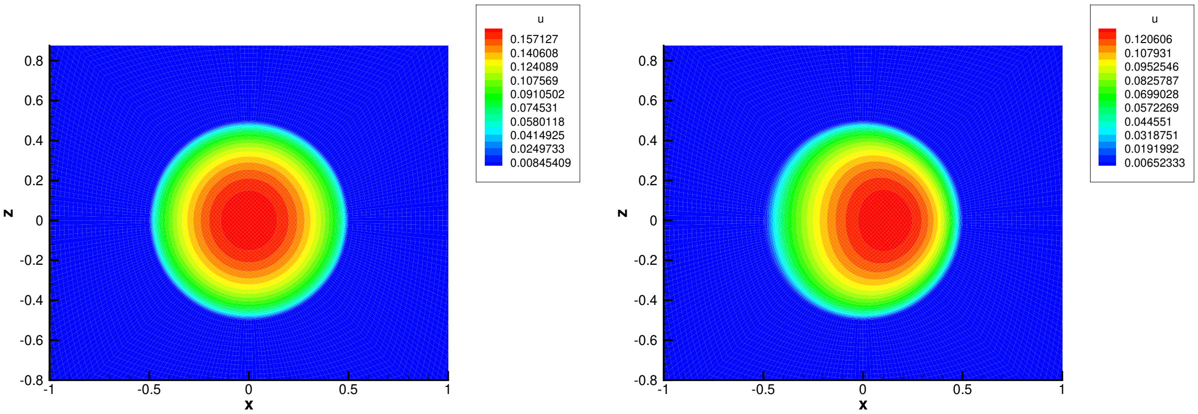

Figure 3.12: Contour plots of the u-velocity component at the lower wall of the $2b = H$ case for Stokes flow (left) and $Re = 64$ (right).

3.9 The Hole Pressure for Reiner-Rivlin Fluids

3.9.1 Numerical Results for Three-Dimensional Holes: Reiner-Rivlin Fluid

Assuming the walls of the plane channel are at $y = \pm 1$, the fully three-dimensional hole problem is addressed with a prescribed Poiseuille velocity $u(y) = 1 - y^2, v = w = 0$ at the channel entrance, while the outflow channel boundary is treated with the Neumann boundary condition

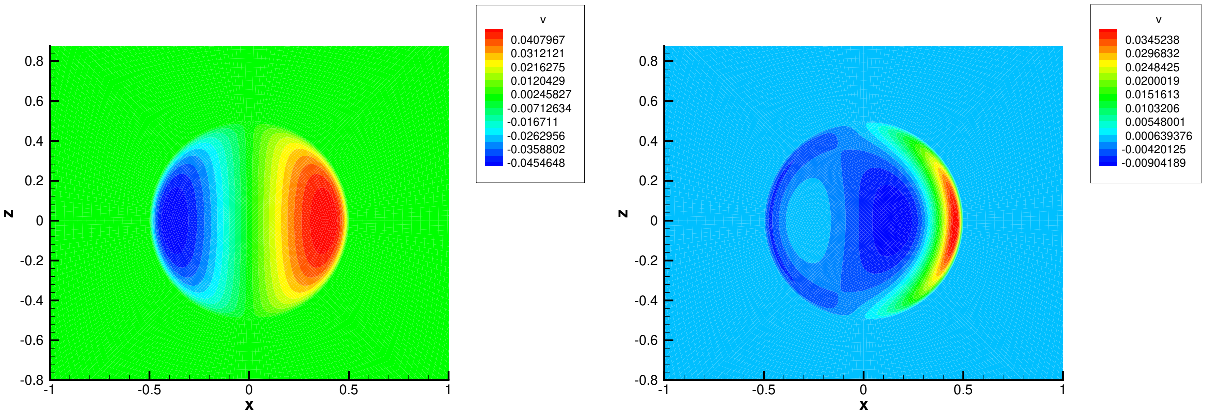

Figure 3.13: Contour plots of the v-velocity component at the lower wall of the $2b = H$ case for Stokes flow (left) and $Re = 64$ (right).

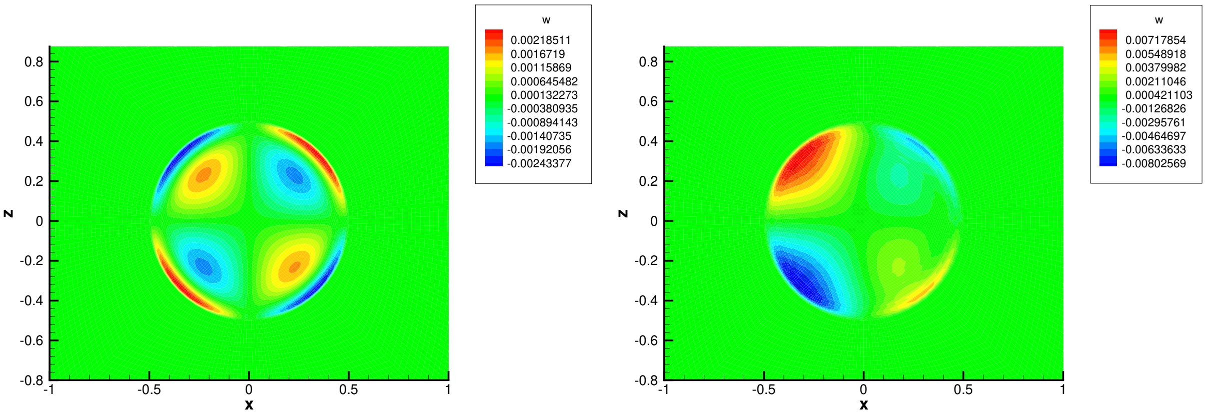

Figure 3.14: Contour plots of the w-velocity component at the lower wall of the $2b = H$ case for Stokes flow (left) and $Re = 64$ (right).

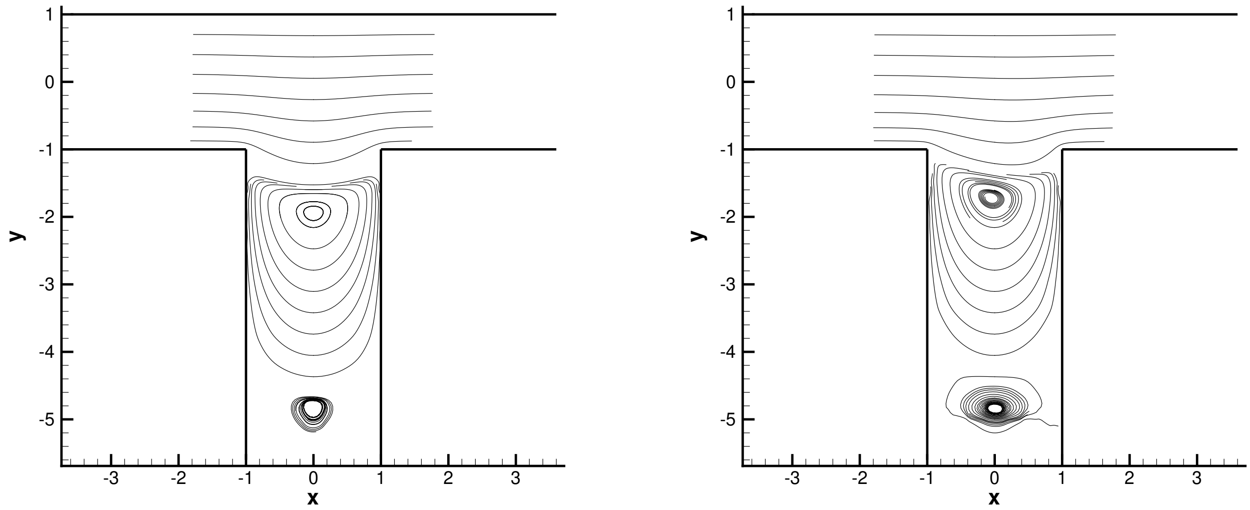

Figure 3.15: Streamlines ($b = H$) for Stokes (left) and $Re = 20$ (right).

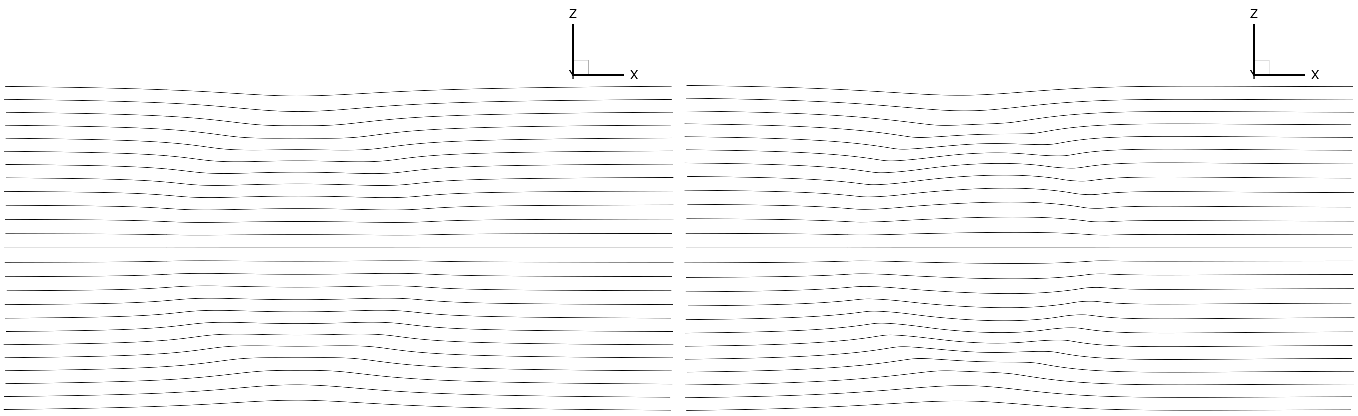

Figure 3.16: Streamlines in the xz plane ($b = H$) for Stokes (left) and $Re = 20$ (right).

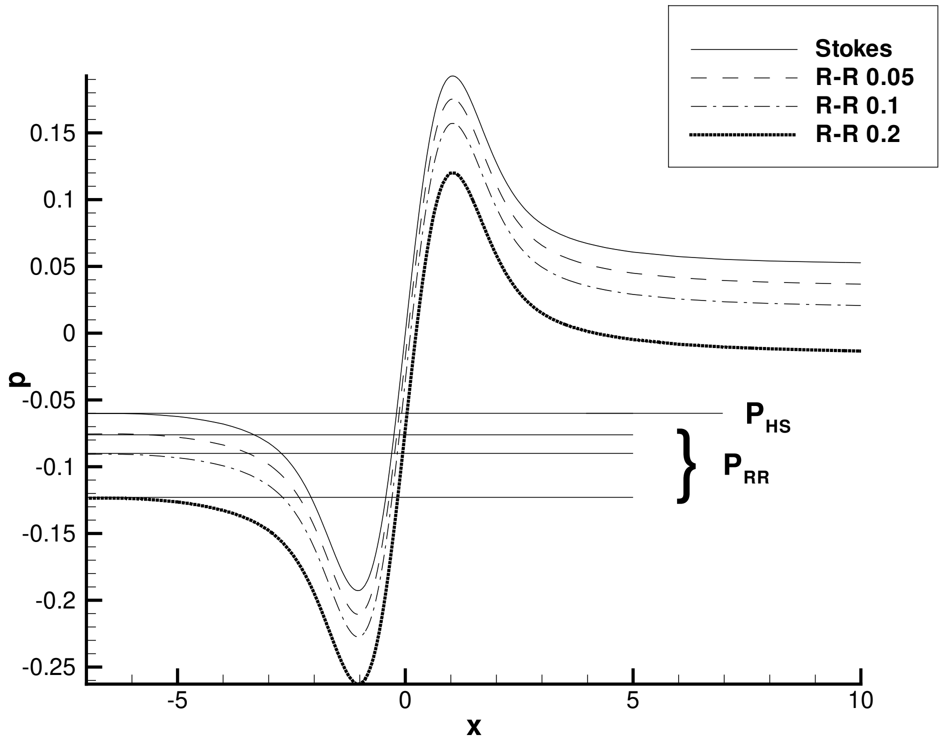

Figure 3.17: Centerline pressure on top wall for $b/H = 1$.

$\frac{\partial \mathbf{u}}{\partial n} = 0, P = 0$. We note that in absence of the pressure tap, this is an exact solution for a plane R-R flow. The boundaries for the cross-flow z-direction are assumed periodic, and the rest of the boundaries are set to solid surfaces. A typical simulation for such a geometry has 2 million degrees of freedom. The presented results were obtained with polynomial orders $p = 2$ and 4 per direction.

The results for three-dimensional holes are presented in terms of the disturbance pressure field which is the extra pressure due to the disturbance created by the hole (see section 3.8.1).

Figure 3.17 shows the centerline pressure on the top wall of the channel for $b/H = 1$ for several values of α' (R-R). The pressure constant is chosen so that the pressure is zero at $(0, -d, 0)$, the center of the bottom plate of the hole at depth d. By definition 3.11 the far upstream ($x = -7$) value of the pressure is the hole pressure as indicated in Figure 3.17, and the difference between the far downstream and far upstream ($x = 10$) values is the pressure recovery P_{D} due to reduced

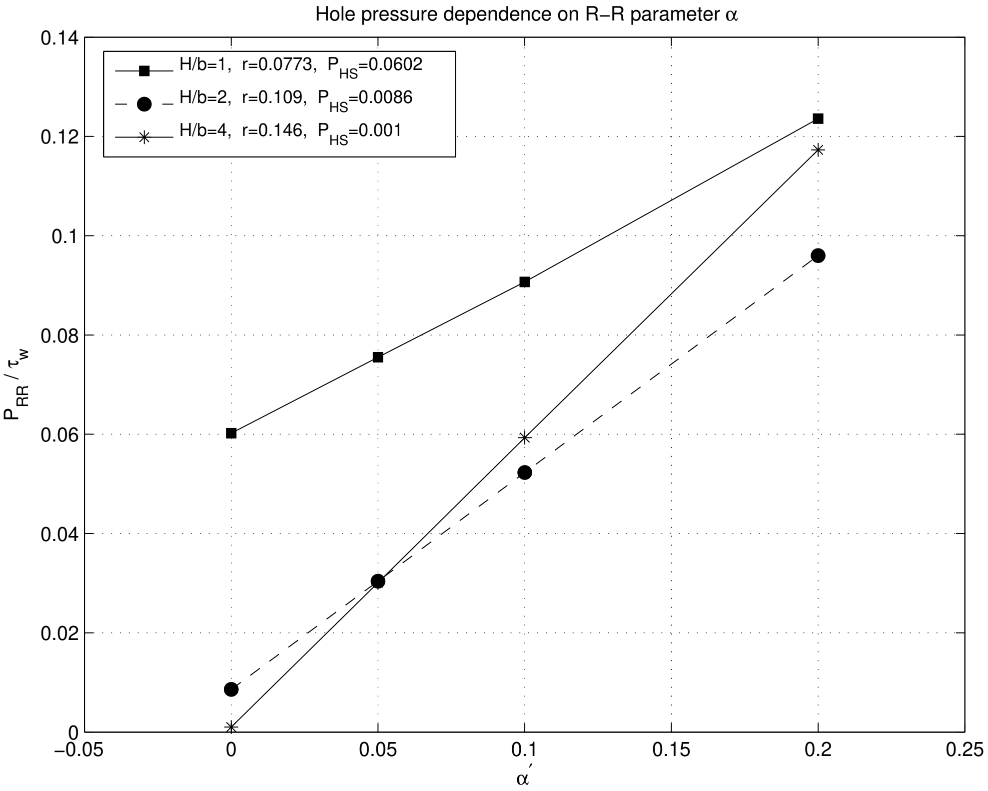

Figure 3.18: Hole pressure as a function of the Reiner-Rivlin number.

dissipation relative to the no-hole geometry. If $P_{\rm H}$ is added to each curve then the pressure will be zero far upstream, $P_{\rm H}$ at the bottom of the hole, and $P_{\rm D}$ far downstream. The advantage of the shifting the pressure to be zero at the hole bottom is that $P_{\rm H}$ and $P_{\rm D}$ can be conveniently displayed on one plot. Since at each end of the channel the flow is asymptotic to Poiseuille flow the plane $(0, y, z)$ is one of fore-aft symmetry. In Stokes flow the streamlines and the pressure field must then have fore-aft symmetry and anti-symmetry respectively as is evident in Figure 3.17 and Figure 3.21 below and, furthermore, $P_{\rm D}$ must be equal to $-2P_{\rm H}$. These properties of Stokes flow provide useful checks on the numerical solutions.

The hole pressures for three hole sizes are plotted according to equation 3.20 rendered dimensionless with division by the Poiseuille wall shear stress, $\tau_w = \eta\dot{\gamma}_w$. The linearity of the plots suggests that for Reiner-Rivlin numbers less than about 0.2 the solutions obtained here fall within the domain of first order perturbations of Stokes flow. In both theoretical and experimental work it has

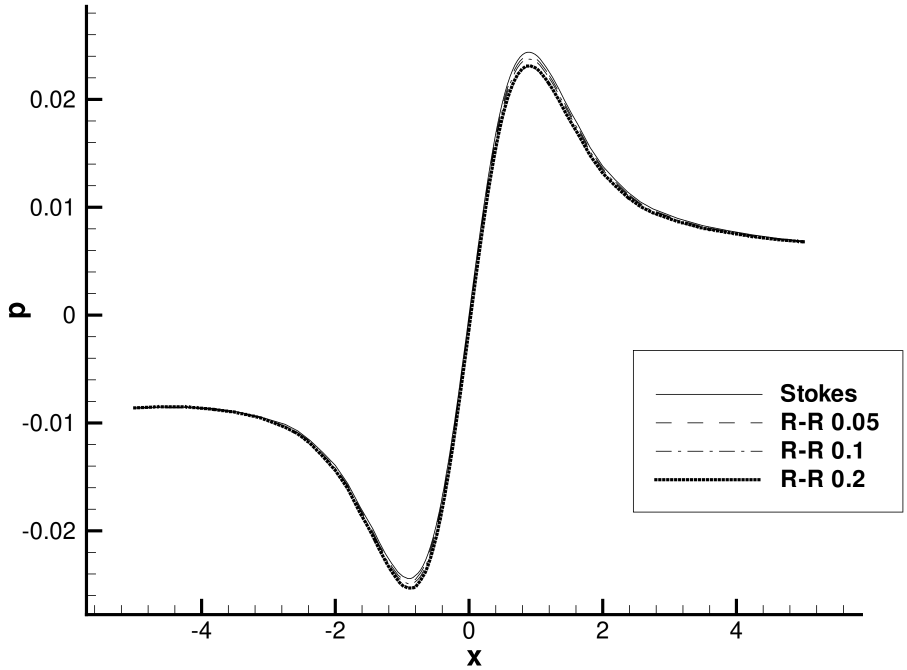

Figure 3.19: Shifting property of centerline pressures: The profiles for different R-R values collapse to a single one when they are shifted by $P_{\mathrm{RR}} - P_{\mathrm{HS}}$.

been assumed (Lodge & Vargas [4], Tanner & Pipkin [56]) that the hole pressure in Stokes flow is negligible compared to non-Newtonian effects. For large holes the experimental data of Tong [63] for $b/H = 1$ show P_{HS} to be measurable. Over the range of numerical values in Figure 3.18. P_{HS} scales roughly as $\sim (b/H)^3$ while r scales as $\sim (b/H)^{-1/2}$. The latter is unlikely to hold for very small b/H, and the r values given here may be approaching the Higashitani-Pritchard [57] value of 1/6 as $b/H \to 0$; indeed a calculation for $b/H = 1/10$ on a coarse mesh gave $r = 0.17$. A fine mesh calculation for the same geometry proved extremely demanding in CPU resources and was judged inappropriate. Kearsley's value of 1/2 for the parallel slot may well be an upper bound for r.

When the pressure curves in Figure 3.17 are shifted by $P_{\mathrm{RR}} - P_{\mathrm{HS}}$ the result is essentially a single curve as shown in Figure 3.19 for $b/H = 1/2$.; similar results were obtained for all values of b/H. This means that away from the aperture the pressure distribution for $\alpha' > 0$ differs from the

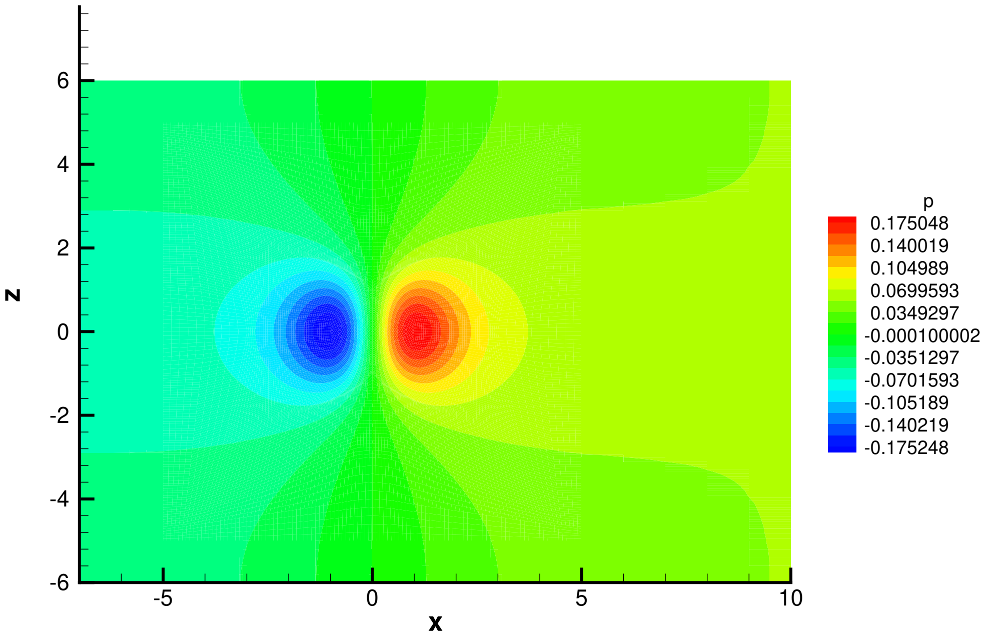

Figure 3.20: Pressure contours on the top plane; positive contours lie to the right of $x = 0$.

corresponding Stokes field by a constant. This implies that far from the aperture the flow is the governed by the Stokes equation. However, it is clear from Figures 3.17 and 3.19 that, except for very small values of b/H, the flow near the wall opposite the hole is not undisturbed Poiseuille flow as assumed in the Higashitani-Pritchard [57] theory.

Figure 3.20 displays pressure field contours for a $\alpha' = 0.2$ on the top wall $(x, H/2, z)$ for $b/H = 1$. The contour pattern shows that the hole disturbance of $O(P_{\mathrm{HS}})$ extends all the way across the channel is an unexpected result. Since P_{HS} scales as $(b/H)^3$ it suggests that in experimental designs which employ large holes, such as the Lodge & Vargas [4] stressmeter, the placement of transducers to measure the gradient of the total pressure will be subject to systematic error in the arrangement shown in Figure 3.1. Furthermore, a sideways off-set of the transducer T_1 does not resolve the problem, and clearly, it should be placed upstream in the undisturbed region.

The hole-pressure is an example of how the asymmetry of an apparently small geometric dis-

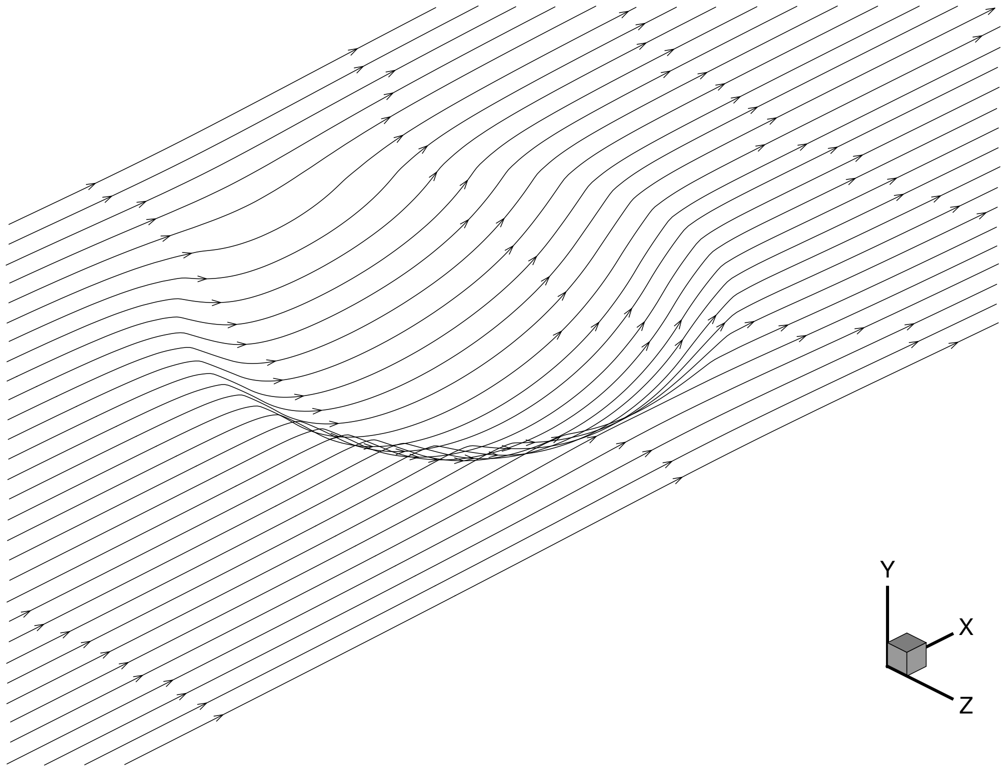

Figure 3.21: Three-dimensional pathlines at a small distance above the wall.

turbance of a viscometric domain can give rise to a significant effect due mostly to the normal stresses. For the values of α' of this work the velocity fields differ only slightly from their Newtonian counterparts. In Figure 3.21 streamlines originating upstream at a distance $0.025H$ from the lower wall are seen to form a bowl as they pass over the aperture with $\alpha' = 0$. This picture changes very slightly when α' is increased to 0.2, and examination of the velocity field through most of the domain yields a similar conclusion. This is consistent with Figure 3.19 which shows the pressure field on the top wall to be Stokesian, but it does not account for the extra hole pressure which shifts the pressure curves to produce a single one. The plane of the aperture is the one location where the Reiner-Rivlin velocity fields are distinctly different from their Newtonian counterparts. In Figure 3.22 the velocity components are plotted in the plane of the aperture along $(0, -H/2, z)$, for $b/H = 1$ and $\alpha' = 0.2$. The Newtonian v, w-components are essentially zero while their Reiner-Rivlin counterparts are small but distinct from the numerical errors. When the u-components are magnified they exhibit differences of the same magnitude as the Reiner-Rivlin v, w-components. Thus even in the limit of small shear rates the three-dimensional hole-pressure flow in the region of

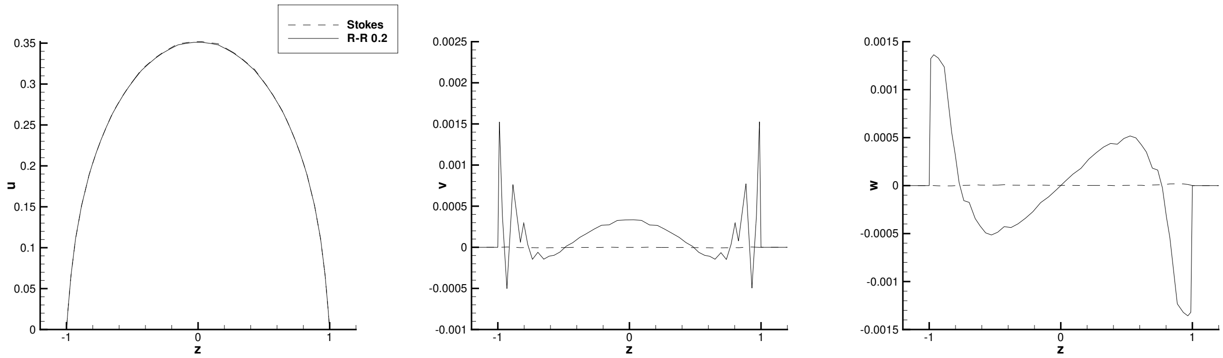

Figure 3.22: Velocity components across the aperture. The observed oscillations in the $v-$component of the R-R flow are due to the sharp corners of the junction and is a manifestation of the noise in the non-Newtonian stress.

the aperture is considerably more complicated than the corresponding two-dimensional problem. The Higashitani-Pritchard [57] theory is built conceptually on the assumption that the aperture region has streamlines in the pattern of Figure 3.21.

3.9.2 Conclusion

The low shear-rate hole pressure for a non-Newtonian fluid has been shown to be determined by the augmented second order fluid, equation 3.10, derived from the materially constant stress, equation 3.3, in which the Reiner-Rivlin stress has constant coefficients η, and α. In that equation the definition of the isotropic stress allows the equilibrium equation to be satisfied by the solution of the Reiner-Rivlin problem, equation 3.5, by means of Theorem 3.2.1 proved by Caswell [55]. This reduction in the order of spatial derivatives is numerically advantageous, and naturally breaks the problem into two steps. In the first, the hole pressure relative to the Reiner-Rivlin value is determined analytically to be independent of hole size and to be the same as the Tanner & Pipkin [56] result for two-dimensional holes. In step two the Reiner-Rivlin value is determined by solution of equation 3.5. Since the term in α in equation 3.1 plays no role in plane flow, the Reiner-Rivlin stress has been put into a form, equation 3.24, that is unaffected by the small discrepancies in the dilatation rate $\nabla \cdot \mathbf{V}$ from zero which occur in numerical simulation. This avoids the creation of artificial three-dimensional forces in regions of plane flow embedded in a three-dimensional domain. Our modified $\mathcal{N}\varepsilon\kappa\mathcal{T}\alpha r$ code was checked in two benchmark problems with known analytical solutions. In particular, for Kearsley's [2] parallel slot the r coefficient in equation 3.20 is calculated to within 1% of the analytical value of $\frac{1}{2}$ (the $p-$convergence issue can be resolved by combined $h/p-$refinement).

The numerical values of the Reiner-Rivlin hole pressure have been shown to follow equation 3.20, and its constants P_{HS}, and r have been tabulated for $\frac{b}{H} = \frac{1}{4}, \frac{1}{2}, 1$. The Stokes hole pressure, P_{HS}, has been shown to scale roughly as $(b/H)^3$, and from the experimental data of Tong [63] its magnitude at $b/H = 1$ was found to be in the measurable range. The coefficient of the Reiner-Rivlin number r which determines hole size dependence of the total hole pressure P_{H} in equation 3.21 is smaller than the Higashitani-Pritchard [57] value of 1/6, which may be the limit for very small holes. Of value to experimental design is the observation that the pressure on the channel wall opposite the aperture is significantly disturbed. An important assumption of the Higashitani-Pritchard theory is that this disturbance is negligible, which is true only for very small holes. This assumption has been influential in the design of the Lodge stressmeter where the hole pressure was measured with pressure transducers located opposite the aperture and at the bottom of the hole. This transducer together with one located upstream, as in Figure 3.1, was also used to measure the pressure gradient of the undisturbed channel flow. This apparent hole pressure will be exactly zero in Stokes flow due to its symmetry properties, but, once non-linear effects such as non-Newtonian stresses or inertia are significant, the measurement cannot be accurately interpreted. Furthermore, the measured pressure gradient will not be the undisturbed value. As might be expected, large holes are intrusive, and their disturbance shown in Figure 3.20 can reach all the way across the channel.

Chapter 4

Part I: Summary and Future Work

In part I of this dissertation we have presented continuum simulations of two non-Newtonian models: The simplest non-Newtonian model, namely the second-order Reiner-Rivlin fluid, and the viscoelastic FENE-P model. The fundamental contribution of this work is the use of numerical stabilization techniques, such as polynomial over-integration and spectral viscosity (SVV). However, in the case of the Reiner-Rivlin fluid, our calculations motivate the direct comparison of fundamental laboratory measurements with computed results, and interesting comparisons arise for the hole pressure problem in both Newtonian and non-Newtonian regimes.

The FENE-P model is described by an additional evolution equation for the conformation tensor $\mathbf{c}$, while the Reiner-Rivlin fluid has no such dependence on polymeric stress variables. Consequently, the numerical stabilization techniques employed in this work target

- The velocity components for the Reiner-Rivlin fluid, and
- The conformation tensor for the FENE-P fluid.

The first section of part I of this dissertation addressed the FENE-P case; we presented a new numerical method suitable for simulating high Reynolds number viscoelastic flows. Our particular interest is on turbulent drag reduction for flows around hydrodynamic surfaces (e.g., ship hulls, torpedos, etc.) using polymers, and some of the developments in this paper were motivated by this application. To this end, the modified splitting scheme proposed in [44] in combination with the modal type representation of spectral elements has been found to be both robust and accurate. We have followed this procedure for Newtonian turbulent flows with success as well, e.g. see [64]. We intentionally targeted the three-dimensional configuration of the flat plate in order to demonstrate that spectral element simulations are practical and that the new stabilization technique is quite effective. Moreover, the Weissenberg number $We = 2.0$ reached in the two-dimensional flow past a cylinder, together with the smoothness of the T_{xx} profiles for these Weissenberg numbers, demonstrate the stability of the method.

The use of numerical diffusion to stabilize simulations of hyperbolic nature goes back to von Neumann and Richtmyer, and it has been practiced routinely in aerodynamic flows, and also in subgrid scale models in large-eddy simulations. However, in more recent work it has been formulated as an adaptive feature, i.e., to be used non-uniformly in space and/or in time as needed. In addition, high-order superviscosity kernels have been the preferred choice. In viscoelastic flows, explicit treatment with artificial viscosity has been done typically without a particularly close connection to resolution or the spatial non-uniformities in the stress field. Of course, formulations such as SUPG address this issue implicitly, but here we refer to explicit artificial viscosity approaches. The current formulation addresses that by targeting modal representations of the numerical solution. This work introduced the spectral vanishing viscosity (SVV) method that imposes monotonicity of the solution without affecting the lower most energetic modes. Only the upper one-third of the modes is affected in a special way so that the high-order accuracy (exponential in our case here) is maintained.

The appeal of the new approach is that it derives its origin in non-linear hyperbolic laws – a theoretical proof presented first by Tadmor (1989) [37]. Another useful feature from the implementation standpoint is that the convolution kernel that represents SVV is second-order and thus it can be easily implemented in existing finite element codes. To this end, an extension of the method in the physical (instead of modal) domain is required but some initial work has already been done in [47]. This is the first work using SVV for viscoelastic flows and many issues need to be resolved. First, the two parameters that characterize the SVV kernel, namely the amplitude and cut-off wavenumber need to be studied more systematically. In the presented examples we have seen that the values of the viscosity amplitude ε depend on the flow parameters. Our criterion in choosing ε has been to employ the smallest value that ensures stability since this will not decrease the accuracy.

A dynamic model that relates the amplitude of SVV and the local strain needs to be explored and implemented appropriately. In addition, the smooth kernel $Q(M, N)$ can be modified so that a space-dependent (i.e., variable) cut-off wavenumber be introduced. Moreover, non-uniform polymer concentration using diffusion models suggested by Apostolakis *et al.* [65] can prove beneficial, considering the disproportionally high values of the xx-component of the stress at $x \sim -\pi$ in Figure 2.17. Finally, more tests are required in the context of other non-Newtonian models in addition to the ones considered here.

The second section of part I of this dissertation addressed the hole pressure problem for Newtonian and Reiner-Rivlin fluids, as well as numerical stabilization for the latter. For the Newtonian case, direct comparison with Tong's [63] experimental data for ratios of $b/H = 1$ (b being the hole diameter and H the channel width) show good agreement with the computed results. Different ratios ($2b = H$) were also examined. The results show that the pressure disturbance is not confined to the near-hole region, as assumed in earlier studies. Moreover, our results verify the fitted tangent slope computed by Lodge & Vargas [4] and Tong [63] in the Stokes hole pressure vs Re plot (Figure 3.8). An improvement in future work would be the employment of longer computational meshes downstream. This can prove useful in the calculation of the dissipation pressure, as it can only be measured when the downstream pressure profile has reached far-field, steady slope conditions.

For the Reiner-Rivlin (R-R) fluid, we formulated different variants of the non-Newtonian part of the stress, ultimately employing the $\mathbf{C}$-tensor formulation of equation 3.24. The advantage in using this formulation is that $\nabla \cdot \mathbf{C}$ does not involve numerically computing $\nabla(\nabla \cdot \mathbf{V})$, thus making incompressibility indirectly satisfied without explicitly enforcing it. Moreover, this formulation uses lower spatial derivatives by one order, which proved beneficial for eliminating noise at elemental boundaries.

Convergence tests of section 3.5 provide the reader with a clear understanding of the accuracy limits with respect to the R-R parameter α. Polynomial over-integration with the three-halves rule efficiently addresses the quadratic non-linearity of the problem (see Figure 3.4). Moreover, the benchmark problem formulated by Kearsley [2] provides a fully three-dimensional configuration having all R-R velocity components *identical* to the Newtonian ones with the R-R effect present only in the pressure. The analytical comparison with the $r-$value in Figure 3.5 shows close agreement (1%) with the analytical result ($r = 1/2$). In addition, the effect of polynomial over-integration and spectral viscosity on the velocity components (Figure 3.6) shows advantages in using numerical filtering if one is willing to trade accuracy for stability. The R-R Stokes hole pressure is shown to scale roughly as $\sim (b/H)^3$, while $r \sim (b/H)^{-1/2}$. The Higashitani-Pritchard [57] value of $1/6$ in the limiting case of $b/H \to 0$ is recovered for a coarse mesh calculation of $b/H = 1/10$ which gave $r = 0.17$ (fine mesh calculation for this geometry proved extremely demanding in computing resources). Figure 3.18 summarizes the ratio dependence of r on α.

Part II

Mesoscopic Simulations

Chapter 5

Dissipative Particle Dynamics

5.1 Multiscale Modeling

The Molecular Dynamics (MD) method is suitable for simulating very small volumes of liquid flow, with linear dimensions of the order of $100\,nm$ or less and for time intervals of several tens of nanoseconds. It can deal effectively with nano-domains and is perhaps the only accurate approach in simulating flows involving very high shear where the continuum or the Newtonian hypotheses may not be valid. For dimensions less than approximately ten molecules the continuum hypothesis breaks down for liquids [66], and MD should be employed to simulate the atomistic behavior of such a system. For larger systems, however, multiscale approaches that rely on the efficiency of continuum-based discretizations have to be employed.

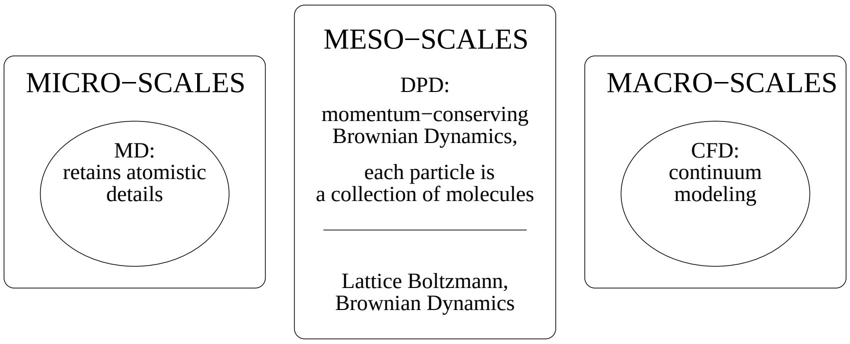

Figure 5.1: The task of the DPD simulation method.

To this end, the coupling of MD to Navier-Stokes equations can extend the range of applicability of both approaches and provide a unifying description of liquid flows from nano-scales to larger scales. Such efforts have been underway by many research groups; however, the proposed algorithms are rather complicated and no fully satisfactory schemes have been developed yet. An alternative, potentially very powerful and simple approach, is a new method developed in the mid 1990s primarily in Europe: the *dissipative particle dynamics* (DPD) method. It has features of both the MD and the lattice Boltzmann method (LBM) [67], and can be thought of as a *coarse-grained* version of MD, but it employs dissipative and stochastic forces to account for the eliminated degrees of freedom. The initial model was proposed by Hoogerbrugge and Koelman [24] as a simulation method to avoid the artifacts associated with traditional LBM simulations while capturing spatio-temporal hydrodynamic scales much larger than those achievable with MD, see Figure 5.1.

The dissipative particle dynamics (DPD) model consists of particles that correspond to *coarse-grained* entities, thus representing molecular clusters rather than individual atoms. The particles move off-lattice interacting with each other through a set of prescribed (conservative and stochastic) and velocity-dependent forces [24, 68]. Specifically, there are three types of forces acting on each dissipative particle: (a) a purely repulsive conservative force, (b) a dissipative force that reduces velocity differences between the particles, and (c) a stochastic force directed along the line connecting the center of the particles. The last two forces effectively implement a thermostat so that thermal equilibrium is achieved. Correspondingly, the amplitude of these forces is dictated by the fluctuation-dissipation theorem [68] that ensures that in thermodynamic equilibrium the system will have a *canonical* distribution. All three forces are modulated by a weight function which specifies the range of interaction or cut-off radius r_c between the particles and renders the interaction local.

A conceptual picture then of DPD is that of soft microspheres randomly moving around but following a preferred direction dictated by the conservative forces. DPD can be interpreted as a Lagrangian discretization of the equations of fluctuating hydrodynamics as the particles simultaneously follow the classical hydrodynamic flow while exhibiting thermal fluctuations. The consistency of the fluctuations is governed by the principles of statistical mechanics.

5.2 Complex Fluids at the Mesoscales

Several complex fluid systems in industrial and biological applications (DNA chains, polymer gels, lubrication problems) are characterized by inherent time and length scales that range from the atomistic level to a millimeter and beyond, often spanning several orders of magnitude. Traditional MD techniques attack the problem at the microscopic level, while continuum models often fail to capture smaller interactions because they resort to averaging techniques or pre-defined association rules. Dilute polymer solutions are a typical example, since individual polymer chains form a group of molecules large by atomic standards but still governed by forces similar to intermolecular ones. Therefore, they form large repeated units exhibiting slow dynamics with possible non-linear interactions (Figure 5.2).

The DPD method is very attractive for the computer simulation of polymer solutions, since by employing bead-spring representations of the polymer chains we can formulate and compare a variety of realistic conservative inter-monomer forces. The method has been used in several studies to simulate the behavior of complex fluids such as bead-spring chain models [69, 70, 71] or polymer drops [72] while many studies have also introduced or compared different time-stepping techniques for the DPD equations [7, 71, 73, 74, 75, 76]. This work focuses on using the basic DPD framework in order to formulate, implement and compare different types of bead-spring models for polymer chains in dilute solutions in periodic and confined geometries. In order to appreciate the potential and computational complexity of DPD we outline time-staggered integrating schemes that efficiently address the issue of different timescale resolution requirements for the monomer-monomer and solvent interactions. Using these integrators in micro-domains our goal is to examine realistic force combinations and map the DPD-computed quantities onto standard macroscopic

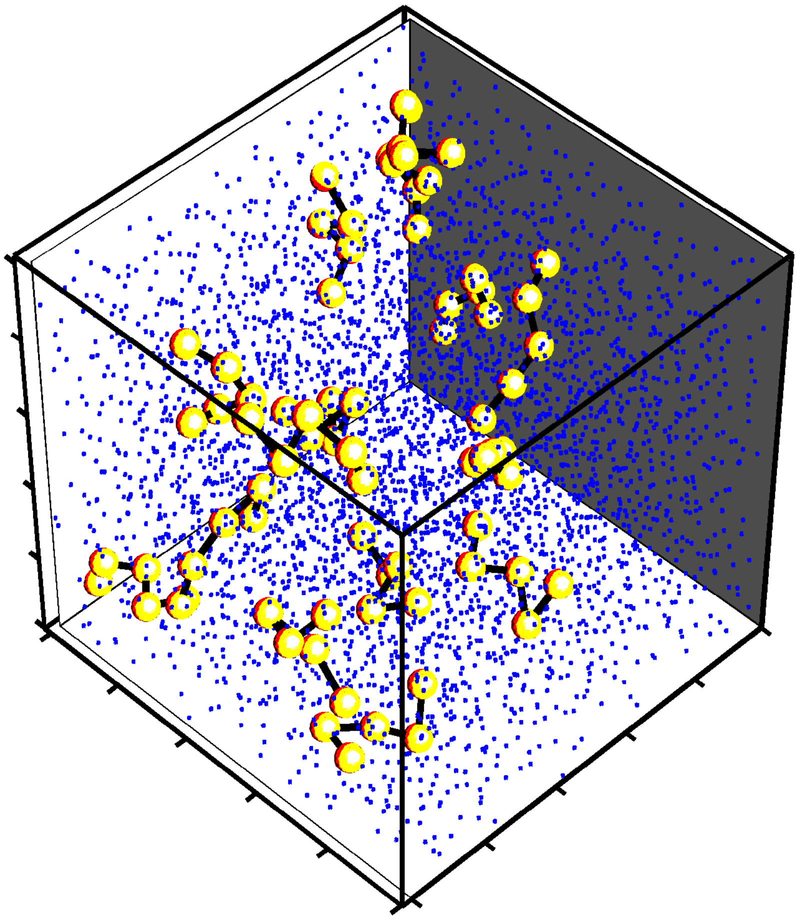

Figure 5.2: Polymer chains (tethered spheres) suspended in a solvent of DPD particles (smaller dots).

experimental and/or theoretical results.

5.3 Previous DPD Works on Polymeric Fluids

The first extended application of DPD for polymers was done by Schlijper, Hoogerbrugge and Manke [69] in 1995. The authors used stiff and Hookean linear springs of chain sizes $M \in [2, 30]$ in box sizes of length $L \in [2.17, 12.5]$, while the range of the number of particles N was 33 to 5889. The integration scheme was an Euler-type one and the work mapped static exponents to the Rouse model ($\nu \approx 0.52$) and computed the conformational time auto-correlation function. Kong *et al.* [77] in a later work also used stiff springs while at the same time the effect of solvent quality was investigated by use of different repulsion rules for unlike species and the static scaling exponent $\nu \approx 0.6$ was recovered. The simulation details were $M \in [5, 50]$, $L = 5R_g$ (as high as $20.5r_c$) and $M \leq 25,000$, where R_g is the radius of gyration of the chain and r_c the cut-off distance (explained later). The same authors [78] employed stiff springs but examined the shear-thinning behavior of the DPD fluids under steady shear. They computed first normal stress coefficients, while using the same philosophy for the repulsion rules [77]. Groot and Warren's 1997 paper [71] was a seminal one in the validation of DPD as a mesoscopic technique. While it provided an excellent analysis for the correct mapping of the DPD parameters to real water solvents, it also employed a modified velocity-Verlet scheme, using a time-step $\Delta t = 0.04$ in system sizes ranging from $8 \times 5 \times 5$ to $8 \times 8 \times 20$ and number densities $\rho \in [3, 5]$. The Flory-Huggins χ-parameter was obtained for polymer lengths $N \in [2, 30]$ subject to Hookean springs, while surface tension effects and some discussion on non-equilibrium simulations were presented. In a 1999 work [79], Groot *et al.* used DPD to simulate block co-polymer separation, employing the same Verlet scheme as in [71], with $\Delta t = 0.06$, in box sizes of $20 \times 20 \times 20$ and $30 \times 30 \times 30$ and polymer numbers in the range $[2400, 20250]$. Direct comparison with Brownian Dynamics (BD) was presented showing that hydrodynamic interactions are essential. A later work by Bosch [80] presented the extension of DPD for viscoelastic flow and showed the equivalence of the method to the macroscopic Navier-Stokes equation with added polymeric stress. It also shows a direct correspondence with known macroscopic models. In 2000, Spenley [81] used linear Hookean springs with chain sizes $M \in [2, 100]$ to recover excluded volume scalings for the polymer. The self-diffusion coefficient was shown to be in good agreement with the theoretical value. The time-step was $\Delta t = 0.05$, the scheme used was velocity-Verlet in boxes of size $L \in [10, 15]$ and density $\rho = 3$.

The DPD equations are stochastic ordinary differential equations, therefore special integrating rules should be developed and evaluated. Vattulainen *et al.* [82] examined the accuracy of several time-marching schemes as in [76] with the same fluid model systems in a box of $L = 16, \Delta t \in [0.01, 0.13]$ and $\rho \in [0.1, 0.7]$ while the value of the fluctuation parameter σ was varied in the ranges 1 to 200. In a very comprehensive work, Nikunen *et al.* [76] performed a series of accuracy tests for different integration schemes, the velocity-Verlet, the self-consistent velocity-Verlet, Lowe's and Shardlow's splitting scheme, concluding the time-step independence of Lowe's scheme for accurate $k_B T$ values. Fluids with and without conservative forcing were considered while polymer chains of $N = 20$ subject to Hookean springs and Lennard-Jones were present in a Newtonian solvent. The simulation details were $L = 10, \rho = 4$ while Δt ranged from 0.005 to 0.4. Fan *et al.* [70] used FENE forces to simulate suspensions with the velocity-Verlet scheme and $\Delta t = 0.06, \sigma = 3, \rho = 3, N = 11880$. The work features Poiseuille flow with frozen particles simulating the wall region. Simple DPD particles show Newtonian behavior, while the macromolecular results (using 135, 1350 and 2700 dumbbells) produce dilute suspension power-law curves. In a similar work Chen *et al.* [72] used FENE forces to simulate drops and shear-thinning is observed. Bead-spring chains are used, each with $M = 16$, making up 90% of the total $N = 157838$ particles in a box of size $40 \times 20 \times 20$. The velocity-Verlet scheme with $\Delta t = 0.06$ was used. Lowe, Bakker and Dreischor [83] used Hookean springs and the Lowe-Andersen scheme in 2004 to compute the center-of-mass velocity autocorrelation function for polymer chains of $M = 2, 4, 8, 16, 32$ beads in a solvent of $N = 10000$ particles. An exponent of $-3/2$ was recovered for the decay, showing consistency with results from hydrodynamic interactions between beads in the same chain. A comparative work by Horsch *et al.* [84] used MD, BD and DPD as a comparison for block co-polymers. The immiscibility for polymer beads was attained with different repulsion rules between different species (for the "soft" cases) and Lennard-Jones, Weeks-Chandler-Andersen for the "hard" cases. The spring laws were FENE and Hookean springs. The polymer lengths were $M = 5, 8, 10, 15$ in systems of $N = 8000, 13000, 20000$ particles, box sizes $18 \times 18.2 \times 28.7$ (MD units) and $\Delta t = 0.01, 0.04$ (MD units). A 2005 work by Chen *et al.* [85] compared the Lowe-Andersen thermostat with other integrating schemes (like the velocity-Verlet, Shardlow's scheme) for block co-polymers. Quantities like the order-disorder transition proved to be sensitive to the scheme. The timestep $\Delta t < 0.1$ and the system consisted of 3000 particles in a box of $L = 10$.

5.4 Timescale Disparity and Time-Integrators

In DPD, the solvent particles represent clusters of actual atoms that interact pairwise via simple soft potentials. The polymer beads are also represented by particles subject to standard DPD forces but in addition they exchange momentum with their neighbors according to an elastic spring force and through other repulsive forces corresponding to hard potentials [71]. In their original work, Schlijper *et al.* [69] reported a speed-up factor of 60 compared to the MD simulations reported in [86]. Since that work, however, several papers have appeared in the literature that present effective time integrators for DPD for single-phase systems as well as for solvent-polymer systems [71, 87, 88, 7, 74, 75]. A systematic evaluation of these time-integrators (with the exception of the new scheme in [75]) was presented in [76] where a hybrid model for polymers was also investigated. In DPD simulations the results are timestep-dependent for large values of the timestep but some models, such as Lowe's scheme [7] (also the scheme in [75]), perform much better than others. A specific result of interest to the current work reported in [76] is that for the hybrid solvent-polymer system involving soft-hard potentials the maximum timestep for good accuracy is a factor of 20 smaller than the timestep for simulating the solvent-only. For example, employing Lowe's approach, the maximum timestep for the hybrid system was $\Delta t_h \approx 0.02$ whereas for the solvent-only it was $\Delta t_s \approx 0.4$. Accuracy here is measured by deviations of the observed kinetic temperature $\langle k_B T \rangle$ from the imposed equilibrium temperature of the system. Moreover, an interesting result reported in [76] is that deviations in the polymer chain temperature dominate the deviations in the temperature of the *entire* solvent-polymer system even for the dilute system they examined with more than 99.5% of the DPD particles being solvent particles.

These findings suggest that the hybrid model can be further enhanced if the multirate dynamics of the polymer and solvent are treated separately, i.e., using different timesteps δt and Δt, respectively, to integrate the DPD governing equations. To this end, in this work we develop a staggered scheme, similar to the subcycling technique used in classical computational fluid dynamics time-integration methods (e.g., semi-Lagrangian method in advection-diffusion systems, see [89]). In particular, for the DPD equations we will integrate the solvent (soft potential) with a large timestep Δt while we will perform several substeps with timestep δt for the polymer (hard potential). In order to evaluate this approach, we consider two representative time-integrators: the DPD velocity-Verlet algorithm (vV) [76] which integrates the standard DPD equations, and also Lowe's algorithm which provides an alternative approach [7].

The standard time-integrators employed in MD simulations are not applicable to this system due to the random and dissipative forces, in addition to the conservative forces, present in the equations of motion. In particular, the dissipative forces depend on the velocity and this makes the equations of motion nonlinear. This, in turn, implies that a sub-iteration should be employed in order to produce a consistent time-integration scheme, see [87], otherwise numerical artifacts are produced. This problem is especially pronounced in the absence of conservative forces, e.g. in simulating the so-called dissipative gas. Here, we model the solvent as *liquid* throughout the work, so we will make use of a modified vV algorithm proposed by Groot and Warren that does not include a sub-iteration. Instead, it introduces a relaxation parameter, λ, which is used to minimize integration errors in the DPD system.

Motivated by the success of this approach, we introduce in the present work a family of new relaxation parameters in various sub-steps involving predicting-correcting action in the time-integration of the polymer-solvent system. We then perform systematic numerical simulations of the system shown in Figure 5.2 at equilibrium conditions in order to determine the best values of the relaxation parameters. After completion of such accuracy tests, we apply the new staggered algorithms in order to quantify the scaling of the radius of gyration of flexible polymer chains described by different polymer models and hard potentials. We also investigate the accuracy and robustness of the new time-integrators in simulating the response of $\lambda-$phage DNA molecules under shear, and we compare our findings with available experimental results.

5.5 The DPD Equations

We consider a system of N particles, each having mass m_i, whose momenta and position vectors are governed by Newton's equations of motions. In particular, for a typical particle i

$$\mathbf{v}_i = \dot{\mathbf{r}}_i, \tag{5.1}$$

$$\mathbf{F}_i = m_i \dot{\mathbf{v}}_i \tag{5.2}$$

where $\frac{d}{dt}$ is denoted by overdot, $\mathbf{v}_i$ is the particle velocity, $\mathbf{r}_i$ its position vector and $\mathbf{F}_i$ the net force. Throughout this work we choose $m_i = 1$. The interparticle force $\mathbf{F}_{ij}$ exerted on particle i by particle j is composed of conservative ($\mathbf{F}^c_{ij}$), dissipative ($\mathbf{F}^d_{ij}$) and random ($\mathbf{F}^r_{ij}$) components. Hence the total force on particle i is given by

$$\mathbf{F}_i = \sum_{i \neq j} \mathbf{F}^c_{ij} + \mathbf{F}^d_{ij} + \mathbf{F}^r_{ij}. \tag{5.3}$$

The above sum acts over all particles within a cutoff radius r_c above which the forces are considered negligible. This interaction radius is set to $r_c = 1$ and defines the length scale of the system. We use the notation $\mathbf{r}_{ij} = \mathbf{r}_i - \mathbf{r}_j$, $\mathbf{v}_{ij} = \mathbf{v}_i - \mathbf{v}_j$, $r_{ij} = |\mathbf{r}_{ij}|$ and the unit vector $\mathbf{e}_{ij} = \frac{\mathbf{r}_{ij}}{r_{ij}}$. We further define each of the forces to take the following form:

$$\mathbf{F}^c_{ij} = F^{(c)}(r_{ij})\mathbf{e}_{ij} \tag{5.4}$$

$$\mathbf{F}^d_{ij} = -\gamma\omega^d(r_{ij})(\mathbf{v}_{ij}\cdot\mathbf{e}_{ij})\mathbf{e}_{ij} \tag{5.5}$$

$$\mathbf{F}^r_{ij} = \sigma\omega^r(r_{ij})\xi_{ij}\mathbf{e}_{ij} \tag{5.6}$$

where ξ_{ij} are symmetric Gaussian random variables with zero mean and unit variance and σ, γ are *not* independent, as shown below. Newton's equations of motions govern each particle's motion through

$$d\mathbf{r}_i = \mathbf{v}_i\delta t \tag{5.7}$$

$$d\mathbf{v}_i = \frac{\mathbf{F}^c_i\delta t + \mathbf{F}^d_i\delta t + \mathbf{F}^r_i\sqrt{\delta t}}{m_i} \tag{5.8}$$

where the factor $\sqrt{\delta t}$ appears because the random forces are interpreted as Wiener processes.

The conservative force $\mathbf{F}^c_{ij}$ is similar to that in the MD formulation. It can be any force derivable from a predefined potential and can be tailored to each individual simulation problem. Possible choices include electrostatic forces, spring-type (Hookean, FENE), van der Waals, hard repulsions (Lennard-Jones) or soft repulsions (potential pre-averaged forces in the spirit of [90]). Hence, $\mathbf{F}^c_{ij}$ is not constrained or defined by the DPD equations. This force as well as the other two act within a sphere of radius r_c, which defines the length scale of the system; it corresponds to a *soft repulsive-only* interaction potential. By averaging the Lennard-Jones potentials or the corresponding molecular field over the *rapidly* fluctuating motions of atoms over short time intervals, an effective average potential is obtained of the form shown in Figure 5.3. A linear approximation of this is as follows [71]:

$$F^{(c)}(r_{ij}) = \begin{cases} a_{ij}(1 - \frac{r_{ij}}{r_c}) & \text{if } r_{ij} \leq r_c \\ 0 & \text{if } r_{ij} > r_c \end{cases} \tag{5.9}$$

Unlike the hard Lennard-Jones potential which is unbounded at $r = 0$, the *soft potential* employed in DPD has a finite value a_{ij} at $r = 0$. To find the value of a_{ij} we follow the process laid out by Groot and Warren [71] and Groot and Rabone [91], i.e. we match the dimensionless compressibility of the DPD system with that of the MD system, namely

$$\kappa^{-1}|_{\mathrm{DPD}} = \frac{1}{k_B T_{\mathrm{DPD}}}\left[\frac{\partial p_{\mathrm{DPD}}}{\partial \rho_{\mathrm{DPD}}}\right]_{\mathrm{T}} = \frac{1}{k_B T_{\mathrm{MD}}}\left[\frac{\partial \rho_{\mathrm{MD}}}{\partial \rho_{\mathrm{DPD}}}\right]\left[\frac{\partial p_{\mathrm{MD}}}{\partial \rho_{\mathrm{MD}}}\right]_{\mathrm{T}} = N_m \kappa^{-1}|_{\mathrm{MD}} \qquad (5.10)$$

where ρ is the number density, $N_m = \dfrac{(\partial\rho)_{\mathrm{MD}}}{(\partial\rho)_{\mathrm{DPD}}}$ is the coarse-graining parameter , k_B is the Boltzmann constant and T the temperature of the system. We note that "DPD" refers to simulation and that in MD we have $N_m = 1$. Then, from an empirical equation of state for DPD fluids, Groot & Warren [71] obtain $a_{ij} \equiv a$ through

$$\kappa^{-1}|_{\mathrm{DPD}} \approx 1 + 0.2\frac{a\rho_{\mathrm{DPD}}}{k_B T_{\mathrm{DPD}}}.$$

By matching the diffusion constant (D_{DPD}) in the DPD simulation with that of water (D_{water}) we find the DPD time scale as

$$\tau = \frac{N_m D_{\mathrm{DPD}} r_c^2}{D_{\mathrm{water}}} \propto N_m^{5/3}.$$

This time scale and the soft potential explain why the DPD method is several orders of magnitude faster than straightforward MD. With respect to the latter, the soft potential removes the "caging effect" of an atom so that the diffusivity of atoms is increased by a factor of 1000, depending on the thermostat. We note that Lowe's [7] approach, which employs an Andersen thermostat, does not decrease the Peclet number. The effect of the time scale is to decrease the corresponding CPU time in proportion to the coarse-graining parameter N_m; hence the *total speed-up* with respect to MD is $1000 \times N_m \times N_m^{5/3}$ for a given system volume. Thus, for $N_m = 5$ and 10 the speed-up factor is 73,000 and 464,000, respectively.

The dissipative and random forces, on the other hand, are characterized by strengths $\omega^d(r_{ij})$

and $\omega^r(r_{ij})$ coupled by the *Fluctuation-Dissipation* relations [68]

$$\omega^d(r_{ij}) = \left[\omega^r(r_{ij})\right]^2 = \begin{cases} (1-\frac{r_{ij}}{r_c})^2 & \text{if } r_{ij} \leq r_c \\ 0 & \text{if } r_{ij} > r_c \end{cases} \tag{5.11}$$

$$\sigma^2 = 2\gamma k_B T. \tag{5.12}$$

The above relation is necessary for thermodynamic equilibrium. The dissipative forces represent friction between the particles and account for energy loss; they depend on the relative velocities and relative position vectors within a pair of particles. However, the random (stochastic) ones are velocity independent; they compensate for lost degrees of freedom due to coarse-graining and heat up the system.

5.6 Models for Polymers

Unlike the MD equations, the DPD equations are stochastic and nonlinear since the dissipative force depends on the velocity. In particular, for complex fluids the presence of both soft and hard potentials suggests the use of time-staggered algorithms for integrating the DPD equations of motion. This allows the efficient study of polymeric physical quantities, such as the radius of gyration of the polymeric chain. The conservative forces present in the usual DPD equations can be tailored in such a way so as to describe a variety of interactions - e.g. Lennard-Jones (LJ), Hookean dumbells, Finitely Extensible Non-Linear Elastic (FENE) springs and van der Waals forces - as long as they are derivable from a given potential $V(r_{ij})$. Figure 5.3 illustrates the need for two different temporal resolutions: the LJ potential (for bead-bead pairs) is a hard repulsion that requires a time-step much smaller than the soft interaction forces of a typical DPD particle pair (which can be thought of as an *averaged* soft potential).

Figure 5.2 shows polymeric chains moving freely in a DPD solvent of N particles. These chains consist of beads (DPD particles) subject to the standard DPD forces: soft repulsive (conservative), dissipative and random. *In addition* to these forces, they are subject to intra-polymer forces,

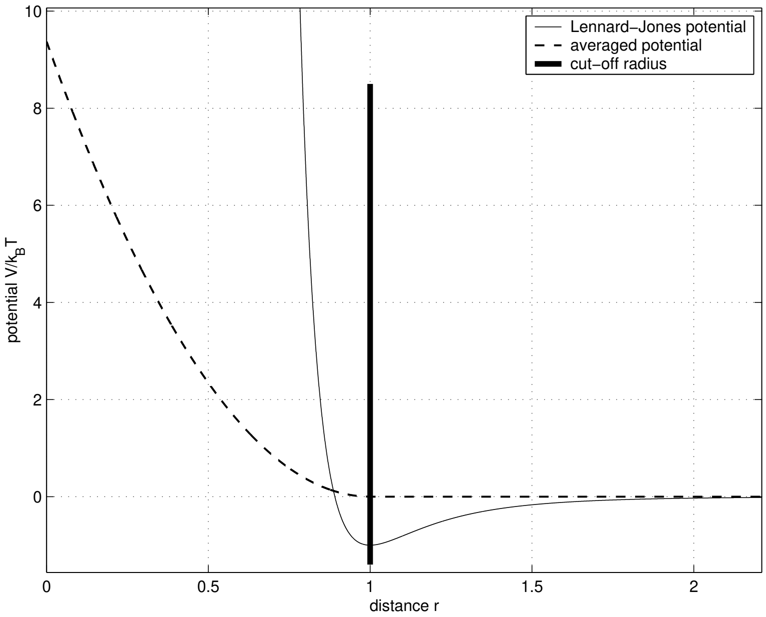

Figure 5.3: Lennard-Jones potential and the soft-repulsive potential which results after averaging.

arising from different combinations of the following types:

- **Lennard-Jones repulsion** The repulsion for each pair of bead particles is given by the shifted LJ potential

$$U_{\mathrm{LJ}} = 4\epsilon\big[(\frac{L}{r_{ij}})^{12} - (\frac{L}{r_{ij}})^{6} + \frac{1}{4}\big]$$

truncated to act *only* for pairs with $r_{ij} < r_c$. We set $\epsilon = k_B T$, $L = 2^{-1/6}$ and $r_c = L \times 2^{-1/6} = 1$. We note that the LJ potential used here is defined at the mesoscopic level to improve polymeric self-avoidance; softer repulsion rules is an alternative approach, see [92].

- **Hookean spring**: Within a chain of M beads each bead is subject to a pairwise harmonic potential

$$U_{\mathrm{HOOKE}} = \frac{\kappa}{2}|\vec{r}_i - \vec{r}_{i-1}|^2, \quad \text{where} \quad i = 2, 3, 4, ..., M$$

and κ is the spring constant.

- **Fraenkel (stiff) spring**: Within a chain of M beads each bead is subject to a pairwise Hookean spring. The spring is considered to be *stiff* since it has a finite equilibrium length r_{eq}. Stretched to a length greater than r_{eq} the spring exerts an attractive force, while pushed to one smaller than r_{eq} it exerts a repulsive one. Its potential follows the formula

$$U_{\mathrm{STIFF}} = \frac{\kappa}{2}(|\vec{r}_i - \vec{r}_{i-1}| - r_{\mathrm{eq}})^2, \qquad \text{where} \quad i = 2, 3, 4, ..., M$$

  and κ is the spring constant.

- **FENE spring**: Within a chain of M beads each bead is subject to a pairwise nonlinear spring force. The Finitely Extensible Non-linear Elastic (FENE) spring has a maximum extensibility $r_{\max}$ beyond which the force becomes infinite, and hence any length greater than $r_{\max}$ is considered unphysical and is not allowed. The potential is described by

$$U_{\mathrm{FENE}} = -\frac{\kappa}{2} r_{\max}^2 log\big[1 - \frac{|\vec{r}_i - \vec{r}_{i-1}|^2}{r_{\max}^2}\big], \qquad \text{where} \quad i = 2, 3, 4, ..., M$$

  and κ the spring constant.

- **Marko-Siggia worm-like chain**: Polymer models of biological importance (DNA, proteins) have been known to be governed by stiff interactions. The worm-like chain [93, 94, 95] can be thought of as a continuous curve in three-dimensional space. Of importance is the *persistence length* λ_p, which is a measure of the chain's stiffness and is the average length over which the orientation of a curve segment does not change ("persists"). We will focus on the bead-spring representation of the model, which approximates a portion of the worm-like chain with a force law given by the Marko-Siggia [25] expression

$$F^{(c)} = \frac{k_B T}{\lambda_p}\Big[\frac{1}{4(1-R)^2} - \frac{1}{4} + R\Big],$$

$$\text{where} \quad R = \frac{|\vec{r}_i - \vec{r}_{i-1}|}{L_{\mathrm{spring}}} = \frac{r}{L_{\mathrm{spring}}} \quad i = 2, 3, 4, ..., M$$

and L_{spring} is the maximum allowed length for each chain (spring) segment. The expression is accurate for large values of the ratio $\frac{L_{\text{spring}}}{\lambda_p}$ and exact as $r \to 0$ or $r \to L_{\text{spring}}$. However, in 1999 it was shown [96] that the Marko-Siggia expression can be better approximated by adding a seventh-order polynomial that leads to an accuracy better than 0.01%. The improved expression takes the form

$$F^{(c)} = \frac{k_B T}{\lambda_p}\Big[\frac{1}{4(1-R)^2} - \frac{1}{4} + R + \sum_{i=2}^{i\leq 7} \alpha_i R^i\Big],$$

where the constants α_i are fixed as follows:

α_2	-0.5164228	α_5	-38.87607
α_3	-2.737418	α_6	39.49944
α_4	16.07497	α_7	-14.17718

The inter-bead force in each case is $\mathbf{F}^p = -\nabla U$. Note that the bonded interactions (spring forces) are pairwise but act only between consecutive beads in a chain (i.e., bead number i exerts spring forces on beads $i-1, i+1$) only, whereas the non-bonded interactions, like the repulsive LJ force, act in a pairwise fashion that depends on the instantaneous relative position of the beads. This fundamental difference requires neighbor-search routines for the latter.

The Marko-Siggia spring law is an averaged quantity, locally approximating flexible rods. The derivation of the formula accounts for coarse-graining microscopic elements of a long chain (such as bead-rod), by use of statistical mechanics. However, in order to use the Marko-Siggia law in molecules with more than two beads (dumbbells), some authors [97] account for the different stiffness of the beaded counterparts by altering the persistence length λ_p of the sub-chains. Detailed analysis of such arguments [98] has shown that it is possible to minimize the errors arising by the introduction of beads and sub-chains. Throughout this work we will adopt the analysis presented in [98] for stained λ-phage DNA molecules assumed to have $L = 21.1\mu m$ (fully extended length) and $\lambda_p = 0.053\mu m$ (persistence length). The correction we will apply will linearly approximate the ratio of effective to true persistence length, for three different regions of the extension: low force, half-extended spring and high-force regimes. More specifically, we define the ratio

$$\lambda^{\star} = \frac{\lambda_p \left[\text{EFFECTIVE}\right]}{\lambda_p \left[\text{TRUE}\right]}$$

so that when $\lambda^{\star} = 1$ no correction is applied. The tables in [98] suggest a high, medium and zero correction for the low-force, half-extension and high-force regions respectively. We go one step further to introduce a linear fit to the suggested correction values for N-bead chains:

$$\lambda^{\star} \approx (1.0 - \hat{z}) \times 0.022 \times (N - 1) + 1, \quad \text{if} \quad N \leq 20$$

$$\lambda^{\star} \approx (1.0 - \hat{z}) \times 0.025 \times (N - 1) + 1, \quad \text{if} \quad N > 20,$$

where $0 \leq \hat{z} \leq 1$ is the instantaneous fractional extension of the whole molecule in the stretching direction. The above expressions approximate fairly accurately the values given in [98] and are implemented in all instances of $N > 2$ for the Marko-Siggia spring force in this work.

Chapter 6

Numerical Algorithms

6.1 Time-Staggered Schemes for Integrating Hybrid Polymeric DPD Models

The two basic DPD integrating schemes we will consider in this work are: A modified version of the classical velocity-Verlet [99] symplectic algorithm (vV) - as outlined by Groot and Warren [71] - and Lowe's algorithm [7, 76]. The vV scheme is characterized by explicit calculation of all forces $\mathbf{F}^c, \mathbf{F}^d, \mathbf{F}^r$ (conservative, dissipative and random) and is known to be timestep dependent, but at the same time straightforward and relatively accurate. Lowe's method, on the other hand, is a scheme based on the Andersen thermostat [100] with the particle velocities corrected every timestep using the Maxwell velocity distribution. In the absence of conservative forces, which are integrated in the vV manner, the scheme is shown to be independent of the chosen timestep Δt [76]. The core operation in Lowe's method involves re-equilibration of the particle momenta at one step with an updated inter-particle relative velocity drawn from a Gaussian distribution.

6.1.1 Time-Staggered Velocity-Verlet Scheme

We consider a modified version of the classical vV DPD integrator (first proposed by Groot and Warren [71]). The vV scheme is characterized by explicit calculation of all forces $\mathbf{F}^c, \mathbf{F}^d, \mathbf{F}^r$ (conservative, dissipative and random) and is known to be time-step dependent, but is straightforward and relatively accurate. It relies on a basic predictor-corrector approach, which uses provisional values of the velocities for the force calculations, which are corrected at the end of each timestep. It is important to keep in mind that the DPD dissipative forces depend on the relative velocities of the particles, hence this prediction is crucial. Below we outline the modified vV scheme with parameter λ. The theoretical value is $\lambda = 0.5$ but Groot and Warren [71] have shown empirically that for a certain range of Δt the optimal value is closer to $\lambda = 0.65$ when $k_B T = 1$. In this work all results presented use the latter, since our timestep is in the optimal range of $\mathcal{O}(10^{-2})$. Denoting the total forces by $\mathbf{F}_i = \sum_{j \neq i} \left[\mathbf{F}_{ij}{}^c + \mathbf{F}_{ij}{}^d + \frac{\mathbf{F}_{ij}{}^r}{\sqrt{\Delta t}} \right]$ and the extra polymeric forces by $\mathbf{F}_i^p = \sum_{j \neq i} \mathbf{F}_{ij}{}^p$, the basic (classical thermostat) vV scheme is outlined in Table 6.1. The subscripts $_{p}, _{s}$ correspond to polymer and solvent quantities, respectively.

To extend this algorithm for the simulation of complex fluids with soft/hard potentials, a large timestep, Δt, is employed for solvent particles and a smaller one, δt, for polymer particles belonging to a chain. To this end, we use provisional values not only for the velocity of the solvent and the polymer, but also for the position of the polymer. The CPU-expensive step of collective force computation is done only once. The velocity *and* the position of the polymer are corrected in the subsequent loop, in which we integrate the polymer particles $\mathbb{K} = \frac{\Delta t}{\delta t}$ times in a separate subcycle (using δt for the timestep). The varying polymeric force $\mathbf{F}_i^p$ is updated within the subcycle, following the change in $\mathbf{r}_{p_i}$, the position of the polymer particles. Hence, during the subcycle we update the intra-polymer forces, but not the inter-particle (total) ones. This would require CPU time for each subcycle equivalent to a standard one. Although we cannot expect exact agreement of the new scheme with the classical one, we can anticipate small differences if the ratio $\frac{\Delta t}{\delta t}$ is not too large and if the (outdated) forces are applied in the correct manner during the δt cycle. The

	λ: relaxation parameter	
▶	$\mathbf{r}_{s_i} \longleftarrow \mathbf{r}_{s_i} + (\Delta t)\mathbf{u}_{s_i} + \frac{(\Delta t)^2}{2m}\mathbf{F}_i$	: SOLVENT
▶	$\mathbf{r}_{p_i} \longleftarrow \mathbf{r}_{p_i} + (\Delta t)\mathbf{u}_{p_i} + \frac{(\Delta t)^2}{2m}(\mathbf{F}_i + \mathbf{F}_i^p)$	: POLYMER
▶	$\widehat{\mathbf{u}}_{s_i} \longleftarrow \mathbf{u}_{s_i} + \lambda(\Delta t)\mathbf{F}_i$	: SOLVENT
▶	$\widehat{\mathbf{u}}_{p_i} \longleftarrow \mathbf{u}_{p_i} + \lambda(\Delta t)(\mathbf{F}_i + \mathbf{F}_i^p)$	: POLYMER
▶	$\forall_{(i,j)} \quad \widehat{\mathbf{F}}_i \left(\begin{array}{c\|c} \mathbf{r}_s & \widehat{\mathbf{u}}_s \\ \mathbf{r}_p & \widehat{\mathbf{u}}_p \end{array} \right)$	: SOLVENT, POLYMER
▶	$\forall_{(i,j)} \quad \widehat{\mathbf{F}}_i^p(\mathbf{r}_p)$	: POLYMER
▶	$\mathbf{u}_{s_i} \longleftarrow \mathbf{u}_{s_i} + \frac{\Delta t}{2m}\left[\mathbf{F}_i + \widehat{\mathbf{F}}_i\right]$	: SOLVENT
▶	$\mathbf{u}_{p_i} \longleftarrow \mathbf{u}_{p_i} + \frac{\Delta t}{2m}\left[\left(\mathbf{F}_i + \mathbf{F}_i^p\right) + \left(\widehat{\mathbf{F}}_i + \widehat{\mathbf{F}}_i^p\right)\right]$	: POLYMER
▷	$\mathbf{F}_i \longleftarrow \widehat{\mathbf{F}}_i$	: SOLVENT, POLYMER
▷	$\mathbf{F}_i^p \longleftarrow \widehat{\mathbf{F}}_i^p$	: POLYMER
▷	Analyzer	

Table 6.1: Overview of the traditional velocity-Verlet approach for a polymer system.

algorithm is summarized in Table 6.2. The proposed scheme depends on the relaxation parameters μ, α, β and λ. In the next section, we will investigate numerically the optimal values for these parameters.

6.1.2 Time-Staggered Lowe's Scheme

Introduced in 1999, Lowe's method [7] is characterized by the explicit calculation of $\mathbf{F}^c$ and the subsequent re-equilibration of all the particle velocities through a Maxwell distribution. This is done using the *relative* velocities of the particles. The method conserves momentum and introduces an extra parameter Γ so that in the limiting case of $\Gamma \times \Delta t \approx 1$ thermalization/dissipation occurs every time-step. Peters [75] recently introduced a modification of Lowe's scheme by keeping the centroid velocity of a particle-pair unchanged before and after the re-equilibration. This results in an attractive scheme, still independent of the chosen time-step (as opposed to the Verlet approach) that also discretizes the original DPD equations. Here we outline the basic Lowe scheme in Table 6.3.

The fundamental difference between Lowe's and the vV scheme is that dissipative and random forces are not explictly calculated in the former. This feature poses constraints on the construc-

$\mathbb{K} = \frac{\Delta t}{\delta t}$,	$\mu, \alpha, \beta, \lambda$: relaxation parameters	
▶	$\mathbf{r}_{s_i} \longleftarrow \mathbf{r}_{s_i} + (\Delta t)\mathbf{u}_{s_i} + \frac{(\Delta t)^2}{2m}\mathbf{F}_i$	: SOLVENT
▶	$\widehat{\mathbf{r}}_{p_i} \longleftarrow \mathbf{r}_{p_i} + (\Delta t)\mathbf{u}_{p_i} + \frac{(\Delta t)^2}{2m}(\mathbf{F}_i + \mathbf{F}^p_i)$	: POLYMER
▷	$\widehat{\widehat{\mathbf{r}}}_{p_i} \longleftarrow \mu \mathbf{r}_{p_i} + (1-\mu)\widehat{\mathbf{r}}_{p_i}$	: POLYMER
▶	$\widehat{\mathbf{u}}_{s_i} \longleftarrow \mathbf{u}_{s_i} + \lambda(\Delta t)\mathbf{F}_i$	: SOLVENT
▶	$\widehat{\mathbf{u}}_{p_i} \longleftarrow \mathbf{u}_{p_i} + \lambda(\Delta t)(\mathbf{F}_i + \mathbf{F}^p_i)$	: POLYMER
▷	$\widehat{\widehat{\mathbf{u}}}_{p_i} \longleftarrow \alpha \mathbf{u}_{p_i} + (1-\alpha)\widehat{\mathbf{u}}_{p_i}$	: POLYMER
▶	$\forall_{(i,j)} \quad \widehat{\mathbf{F}}_i \left(\begin{array}{c\|c} \mathbf{r}_s & \widehat{\mathbf{u}}_s \\ \widehat{\widehat{\mathbf{r}}}_{p_i} & \widehat{\widehat{\mathbf{u}}}_{p_i} \end{array} \right)$	: SOLVENT, POLYMER
▷	$\widehat{\widehat{\mathbf{F}}}_i \longleftarrow \beta \mathbf{F}_i + (1-\beta)\widehat{\mathbf{F}}_i$	: POLYMER
for $k = 0, 1, \ldots, \mathbb{K}-1$	$\mathbf{r}_{p_i} \longleftarrow \mathbf{r}_{p_i} + (\delta t)\mathbf{u}_{p_i} + \frac{(\delta t)^2}{2m}(\widehat{\widehat{\mathbf{F}}}_i + \mathbf{F}^p_i)$ $\forall_{(i,j)} \quad \mathbf{F}^p_{\dagger i}(\mathbf{r}_p)$ $\mathbf{F}_{\mathrm{old}} = \frac{\mathbb{K}-k}{\mathbb{K}}\mathbf{F}_i + \frac{k}{\mathbb{K}}\widehat{\mathbf{F}}_i$ $\mathbf{F}_{\mathrm{new}} = \frac{\mathbb{K}-(k+1)}{\mathbb{K}}\mathbf{F}_i + \frac{k+1}{\mathbb{K}}\widehat{\mathbf{F}}_i$ $\mathbf{u}_{p_i} \longleftarrow \mathbf{u}_{p_i} + \frac{\delta t}{2}\left[\left(\mathbf{F}_{\mathrm{old}} + \mathbf{F}^p_i\right) + \left(\mathbf{F}_{\mathrm{new}} + \mathbf{F}^p_{\dagger i}\right)\right]$ $\mathbf{F}^p_i \longleftarrow \mathbf{F}^p_{\dagger i}$	: POLYMER
▶	$\mathbf{u}_{s_i} \longleftarrow \mathbf{u}_{s_i} + \frac{\Delta t}{2m}\left[\mathbf{F}_i + \widehat{\mathbf{F}}_i\right]$	: SOLVENT
▷	$\mathbf{F}_i \longleftarrow \widehat{\mathbf{F}}_i$	: SOLVENT
▷	Analyzer	

Table 6.2: Overview of the time-staggered velocity-Verlet approach for a polymer system.

tion of the inner δt subcycle. Therefore, we update the conservative solvent forces $\mathbf{F}^c$ once per cycle and the conservative polymeric forces $\mathbf{F}^p$ in every subcycle, following the vV approach. The thermalization is done *once* at the end of the Δt cycle as shown in Table 6.4.

6.2 Accuracy Tests

6.2.1 Metrics and Simulation Parameters

The accuracy of the methods can be measured by monitoring either the temperature of the thermostat or other physical quantities, specific to the polymer system, e.g. the polymeric radius of gyration, R_g, or chain temperature, $\langle k_B T \rangle$ (as was proposed in [76]), defined respectively as

Γ: thermalization parameter	
▶ $\mathbf{r}_{s_i} \longleftarrow \mathbf{r}_{s_i} + (\Delta t)\mathbf{u}_{s_i} + \frac{(\Delta t)^2}{2m}\mathbf{F}^c_i$	: SOLVENT
▶ $\mathbf{r}_{p_i} \longleftarrow \mathbf{r}_{p_i} + (\Delta t)\mathbf{u}_{p_i} + \frac{(\Delta t)^2}{2m}\left[\mathbf{F}^c_i + \mathbf{F}^p_i\right]$	: POLYMER
▶ $\forall_{(i,j)} \quad \widehat{\mathbf{F}}^c_i \begin{pmatrix} \mathbf{r}_s \\ \mathbf{r}_p \end{pmatrix}$	: SOLVENT, POLYMER
▶ $\forall_{(i,j)} \quad \widehat{\mathbf{F}}^p_i(\mathbf{r}_p)$	: POLYMER
▶ $\mathbf{u}_{s_i} \longleftarrow \mathbf{u}_{s_i} + \frac{\Delta t}{2m}\left[\mathbf{F}^c_i + \widehat{\mathbf{F}}^c_i\right]$	: SOLVENT
▶ $\mathbf{u}_{p_i} \longleftarrow \mathbf{u}_{p_i} + \frac{\Delta t}{2m}\left[\left(\mathbf{F}^c_i + \mathbf{F}^p_i\right) + \left(\widehat{\mathbf{F}}^c_i + \widehat{\mathbf{F}}^p_i\right)\right]$	: POLYMER
▶ $\forall$ N_p distinct pairs i, j such that $r_{ij} < r_c$	: SOLVENT, POLYMER
• Generate a Gaussian ξ_{ij} with $\mu = 0, \sigma^2 = 1$	
• Form $\mathbf{u}^\circ_{ij} \cdot \mathbf{e}_{ij} = \xi_{ij}\sqrt{\frac{2k_BT}{m}}$	
• Generate a uniform distribution ψ_{N_p}	
• If $\psi_{N_p} < \Gamma \times \Delta t \leq 1$:	
$2\mathbf{\Delta}_{ij} = \mathbf{e}_{ij}(\mathbf{u}^\circ_{ij} - \mathbf{u}_{ij}) \cdot \mathbf{e}_{ij}$	
$\mathbf{u}_i \longleftarrow \mathbf{u}_i + \mathbf{\Delta}_{ij}$	
$\mathbf{u}_j \longleftarrow \mathbf{u}_j - \mathbf{\Delta}_{ij}$	
▷ $\mathbf{F}^c_i \longleftarrow \widehat{\mathbf{F}}^c_i$	: SOLVENT, POLYMER
▷ $\mathbf{F}^p_i \longleftarrow \widehat{\mathbf{F}}^p_i$	: POLYMER
▷ Analyzer	

Table 6.3: Overview of the traditional Lowe's approach for a polymer system.

$$\langle {R_g}^2 \rangle = \Big\langle \frac{1}{M}\sum_{i=1}^{M}(R_i - R_{\text{cm}})^2 \Big\rangle, \qquad \langle k_B T\rangle_{\text{chain}} = \frac{m}{3M}\langle \sum_{i=1}^{M} \mathbf{u}_i^2 \rangle$$

for an M-bead chain. Here, R_i denotes the position of bead i, and R_{cm} the center of mass. The presented schemes depend on $\mu, \alpha, \beta, \lambda$ and Γ. Setting $\lambda = 0.65$ seems to be an appropriate choice [71] for timesteps $\delta t \approx 0.01$, while using the arbitrary value of $\Gamma = 4.5$ will only affect the convergence rate of Lowe's method and not the accuracy. Letting $\mathbb{K} = \frac{\Delta t}{\delta t}$, we adopt the choices outlined in table 6.5 for $\mathbf{F}_{\text{old}}$ and $\mathbf{F}_{\text{new}}$ of tables 6.2,6.4 in the k^{th} subcycle.

Clearly, the choice of $\mathbf{F}_{\text{old}}$, $\mathbf{F}_{\text{new}}$ determines how the subcycle treats the second velocity update. In the non-weighted case, we correct the predictions using static values of the old and newly computed total forces. However, the weighted approach accounts for a linear gradient of them, rendering the "old" and "new" total forces old and new *locally in time* within each subcycle δt.

$\mathbb{K} = \frac{\Delta t}{\delta t}$, μ, β: relaxation parameters, Γ: thermalization parameter

▶ $\mathbf{r}_{s_i} \longleftarrow \mathbf{r}_{s_i} + (\Delta t)\mathbf{u}_{s_i} + \frac{(\Delta t)^2}{2m}\mathbf{F}^c_i$: SOLVENT

▶ $\widehat{\mathbf{r}}_{p_i} \longleftarrow \mathbf{r}_{p_i} + (\Delta t)\mathbf{u}_{p_i} + \frac{(\Delta t)^2}{2m}\left[\mathbf{F}^c_i + \mathbf{F}^p_i\right]$: POLYMER

▷ $\widehat{\widehat{\mathbf{r}}}_{p_i} \longleftarrow \mu\mathbf{r}_{p_i} + (1-\mu)\widehat{\mathbf{r}}_{p_i}$: POLYMER

▶ $\forall_{(i,j)} \quad \widehat{\mathbf{F}}^c_i\begin{pmatrix}\mathbf{r}_s\\ \widehat{\widehat{\mathbf{r}}}_p\end{pmatrix}$: SOLVENT, POLYMER

▷ $\widehat{\widehat{\mathbf{F}}}^c_i \longleftarrow \beta\mathbf{F}^c_i + (1-\beta)\widehat{\mathbf{F}}^c_i$: POLYMER

for $k = 0, 1, \dots, \mathbb{K}-1$: POLYMER

$$\mathbf{r}_{p_i} \longleftarrow \mathbf{r}_{p_i} + (\delta t)\mathbf{u}_{p_i} + \frac{(\delta t)^2}{2m}(\widehat{\widehat{\mathbf{F}}}^c_i + \mathbf{F}^p_i)$$

$$\forall_{(i,j)} \quad \mathbf{F}^p_{\dagger i}(\mathbf{r}_p)$$

$$\mathbf{F}^c_{\text{old}} = \frac{\mathbb{K}-k}{\mathbb{K}}\mathbf{F}^c_i + \frac{k}{\mathbb{K}}\widehat{\mathbf{F}}^c_i$$

$$\mathbf{F}^c_{\text{new}} = \frac{\mathbb{K}-(k+1)}{\mathbb{K}}\mathbf{F}^c_i + \frac{k+1}{\mathbb{K}}\widehat{\mathbf{F}}^c_i$$

$$\mathbf{u}_{p_i} \longleftarrow \mathbf{u}_{p_i} + \frac{\delta t}{2}\left[\left(\mathbf{F}^c_{\text{old}} + \mathbf{F}^p_i\right) + \left(\mathbf{F}^c_{\text{new}} + \mathbf{F}^p_{\dagger i}\right)\right]$$

$$\mathbf{F}^p_i \longleftarrow \mathbf{F}^p_{\dagger i}$$

▶ $\forall\ N_p$ distinct pairs i, j such that $r_{ij} < r_c$: SOLVENT, POLYMER

- Generate a Gaussian ξ_{ij} with $\mu = 0, \sigma^2 = 1$
- Form $\mathbf{u}^\circ_{ij} \cdot \mathbf{e}_{ij} = \xi_{ij}\sqrt{\frac{2k_B T}{m}}$
- Generate a uniform distribution ψ_{N_p}
- If $\psi_{N_p} < \Gamma \times \Delta t \leq 1$:

$$2\boldsymbol{\Delta}_{ij} = \mathbf{e}_{ij}(\mathbf{u}^\circ_{ij} - \mathbf{u}_{ij}) \cdot \mathbf{e}_{ij}$$

$$\mathbf{u}_i \longleftarrow \mathbf{u}_i + \boldsymbol{\Delta}_{ij}$$

$$\mathbf{u}_j \longleftarrow \mathbf{u}_j - \boldsymbol{\Delta}_{ij}$$

▷ $\mathbf{F}^c_i \longleftarrow \widehat{\mathbf{F}}^c_i$: SOLVENT, POLYMER

▷ $\mathbf{F}^p_i \longleftarrow \widehat{\mathbf{F}}^p_i$: POLYMER

▷ Analyzer

Table 6.4: Overview of the time-staggered Lowe's approach for a polymer system.

	$\mathbf{F}_{\text{old}}$	$\mathbf{F}_{\text{new}}$
Non-weighted staggering	$\mathbf{F}_i$	$\widehat{\mathbf{F}}_i$
Weighted staggering	$\frac{\mathbb{K}-k}{\mathbb{K}}\mathbf{F}_i + \frac{k}{\mathbb{K}}\widehat{\mathbf{F}}_i$	$\frac{\mathbb{K}-(k+1)}{\mathbb{K}}\mathbf{F}_i + \frac{k+1}{\mathbb{K}}\widehat{\mathbf{F}}_i$

Table 6.5: Choices for old and new forces acting on polymer beads.

We consider a 4000-DPD particle fluid in equilibrium in a periodic simulation box of dimensions $L_x = L_y = L_z = 10$, thus fixing the number density $\rho = 4$, with 80 of these DPD particles belonging to 4 different chains, 20-beads each, subject to additional FENE and LJ forcing. The different parameters of the simulation take the following values: The thermal energy level $k_BT = 1$, the mass of each particle $m = 1$, the cutoff distance $r_c = 1$, Lowe's thermalization parameter $\Gamma = 4.5$, the conservative force amplitude $a_{ij} = \frac{75k_BT}{\rho}$ for both vV and Lowe's schemes, the random force amplitude $\sigma = 3$ (this fixes the dissipative force amplitude to $\gamma = 4.5$), the FENE parameters $r_{\max} = 3r_c, \kappa = 7$ and the LJ parameters $\epsilon = k_BT, L = 2^{-1/6}, r_c = L \times 2^{-1/6} = 1$. We note that the resulting system of polymer forces is relatively stiff, with a time-step $\delta t \approx 0.02$ being close to the upper limit for stability of the simulation (if we use a non-staggered integrator). However, using the proposed schemes, we will examine the maximum absolute error for the chain and total k_BT in two regimes: A *safe* one ($\Delta t \in [10^{-3}, 10^{-2}], \delta t = 10^{-3}$) and a more *ambitious* one ($\Delta t \in [10^{-2}, 10^{-1}], \delta t = 10^{-2}$).

6.2.2 The Baseline Case of $\mu = 0, \alpha = 0, \beta = 0$

We compare the accuracy of the vV and Lowe's schemes in figure 6.1 for the safe range, while figure 6.2 shows the maximum temperature error for large Δt. The former can be used as a guideline for the effect of the time-staggering as the error does not exceed 7×10^{-3} even for ratios of $\mathbb{K} = 10$. The latter shows realistic error values for practical applications of the proposed schemes, reaching values two orders of magnitude larger. These are precisely the errors we will attempt to minimize in the following sections. Another quantity we will monitor is the mean radius of gyration $\langle R_g \rangle$ for both schemes. Using the weighted approach, in table 6.6 we show the effect of the time-step ratio on $\langle R_g \rangle$ in the ambitious range for 5-bead chains. The disagreement between the $\mathbb{K} = 1$ values and the staggered never exceeds 2% for the studied range.

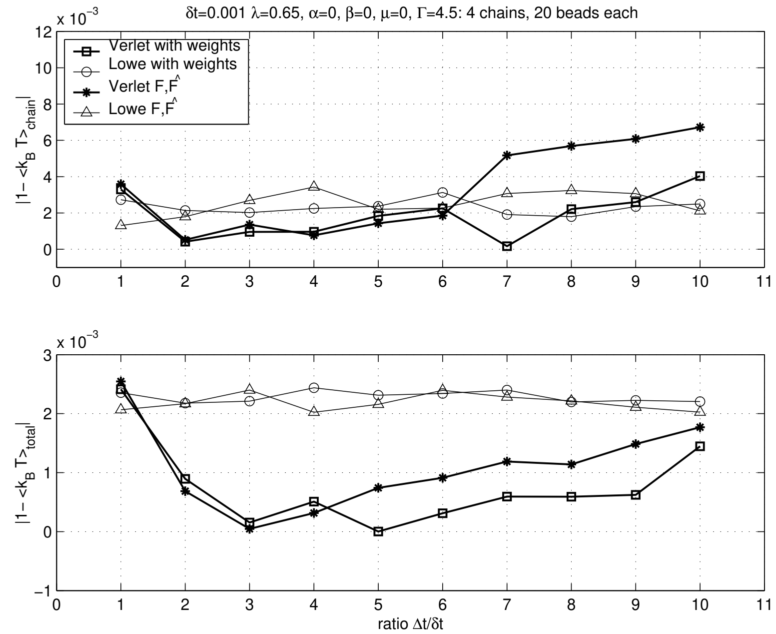

Figure 6.1: Baseline case: Maximum absolute error in total (upper) and chain (lower) $k_B T$ versus $\frac{\Delta t}{\delta t}$ for the vV and Lowe's methods for the *safe* range of Δt. The results also compare the non-weighted schemes with the weighted ones.

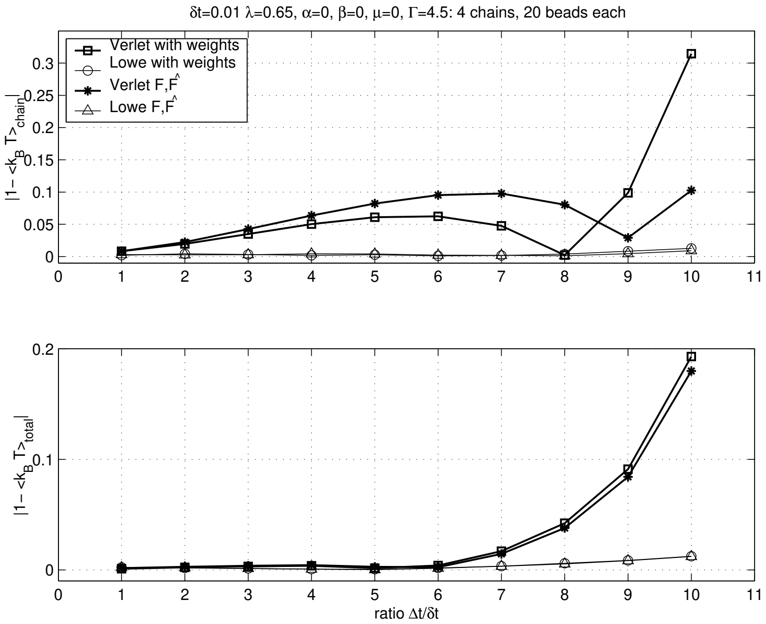

Figure 6.2: Baseline case: Maximum absolute error in total (upper) and chain (lower) $k_B T$ versus $\frac{\Delta t}{\delta t}$ for the vV and Lowe's methods for the *ambitious* range of Δt. The results also compare the non-weighted schemes with the weighted ones.

$\Delta t/\delta t$	1	2	4	6	8	10
Verlet	1.0434	1.0410	1.0352	1.0311	1.0345	1.0521
Lowe	1.0449	1.0459	1.0389	1.0435	1.0479	1.0531

Table 6.6: $\langle R_g \rangle$ dependence on $\frac{\Delta t}{\delta t}$ for 5 beads (baseline case with $\delta t = 10^{-2}$).

6.2.3 Investigating Other Choices for μ, α and β

The relaxation parameters λ, μ, α and β of the schemes provide some flexibility in manipulating the prediction of $\widehat{\mathbf{u}}$, $\widehat{\widehat{\mathbf{r}}}_p$, $\widehat{\widehat{\mathbf{u}}}_p$ and $\widehat{\widehat{\widehat{\mathbf{F}}}}$ respectively. Groot and Warren [71] have already shown that for a range of timesteps ($\Delta t < 0.06$) the optimal value for λ is close to 0.65, when using the straightforward Verlet scheme. We will stick to this value for all the accuracy tests presented here. Moreover, for simplicity the following tests will use the non-weighted time-staggering. Since the timestep dependence in Lowe's method comes from the conservative forces, we anticipate any optimal value findings to be directly applicable to the time-staggered Lowe scheme.

We attempt varying μ, α and β in the range $[-1, 1]$. By using values in the open interval $(0, 1)$ we essentially take a weighted average of the quantity between the prediction at the $(n+1)^{th}$ step and the old value at the n^{th} step. In the limiting cases, 0 uses *only* the prediction while 1 uses *only* the n^{th} step value. As an additional test, we also investigate negative values, thus numerically favoring the prediction up to a coefficient of 2. This *dis*favors the n^{th} step value, by introducing a negative coefficient. Wider ranges are intuitively unphysical and will not be considered.

Figure 6.3 shows the absolute error in $k_B T$ for the chains and the whole system (polymer and solvent particles) for the system described earlier, i.e. a 4000-DPD fluid with four 20-bead chains governed by FENE and LJ forces. The error is plotted against the parameter range $[-1, 1]$. We note that the variation is done with *one* parameter at a time, that is, while varying one parameter, the two other parameters are fixed to 0. The ratio $\frac{\Delta t}{\delta t}$ is fixed to 5, with $\Delta t = 0.005, \delta t = 0.001$, rendering the timestep value safe (recall that stability for the chosen parameters requires $\delta t < 0.03$).

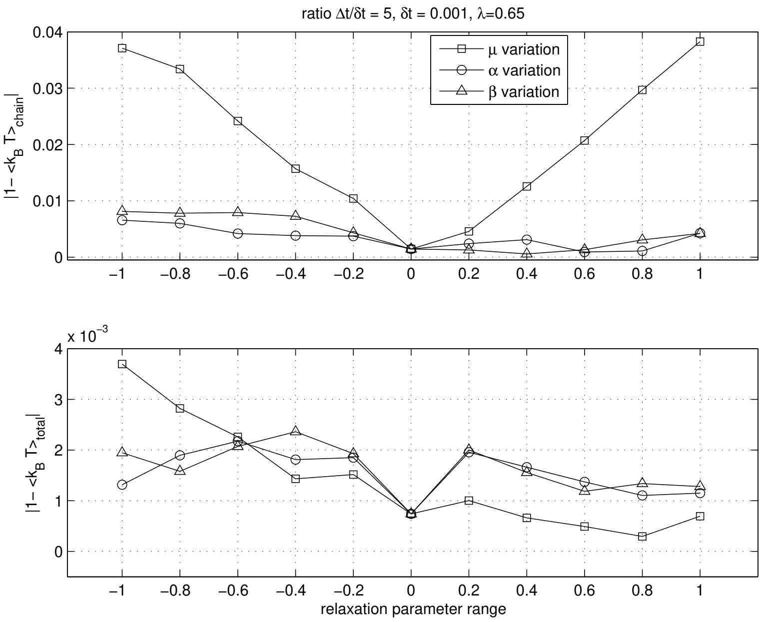

Figure 6.3: Maximum absolute error in total (upper) and chain (lower) $k_B T$ versus individual relaxation parameter variation. Optimal parameters prove to be $\mu \approx 0, \alpha \approx 0.6, \beta \approx 0.4$ when perturbed from 0, one parameter at a time.

Accuracy in the negative parameter range proves to be worse than the positive one. Moreover, the sensitivity of the system on the variation of μ is extremely pronounced. As far as the optimal values are concerned, the three separate curves indicate that reasonable choices would be either

$$\begin{aligned} (\mu, \alpha, \beta) &= (0, 0.6, 0) \quad \text{or} \\ (\mu, \alpha, \beta) &= (0, 0, 0.4), \end{aligned}$$

and these will be separately investigated in the following sections. The total temperature shows an error range of $[0, 2] \times 10^{-3}$ for all positive values. Hence, error in the polymer chains *alone* will be the optimal parameter choice guideline.

Another way of investigating optimal parameter choices would be simultaneous variation of μ, α, β in the same range. Figure 6.4 shows that simultaneous variation is a bad choice. Also, setting $(\mu, \alpha, \beta) = (0, 0.6, 0.4)$ simultaneously, still proved to produce an error larger than the baseline

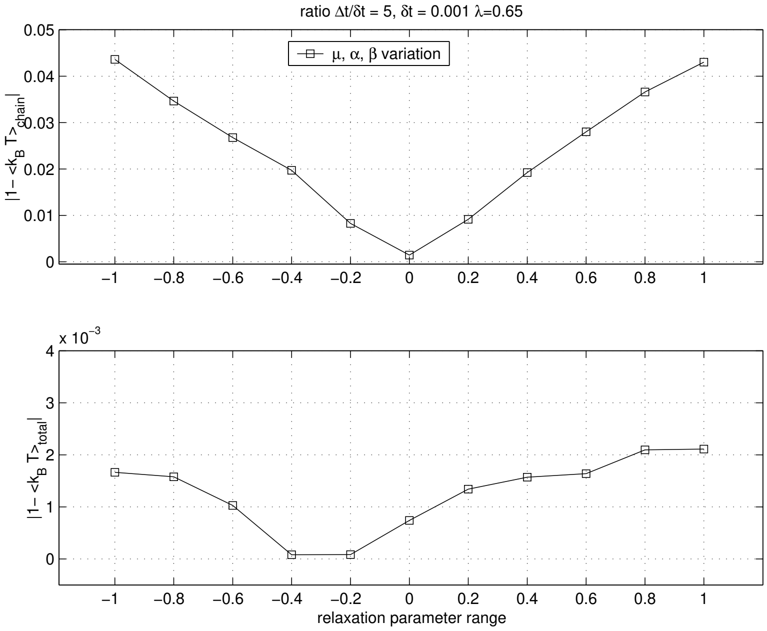

Figure 6.4: Simultaneous relaxation parameter variation: a bad approach. (The quantities plotted are the same as in the previous figure).

$(\mu, \alpha, \beta) = (0, 0, 0)$ case.

Equipped with the above indications, we perform the definitive investigative test in the safe range of $\Delta t \in [10^{-3}, 10^{-2}], \delta t = 10^{-3}$ for the vV scheme, comparing results for the triplets $(\mu, \alpha, \beta) = (0, 0.6, 0), (0, 0, 0.4)$.

Summarizing the results for this section, figure 6.5 shows a mild advantage of $\beta = 0.4$ for timestep ratios $\frac{\Delta t}{\delta t} \in [2, 7]$ but $\alpha = 0.6$ performs better for ratios $\in [8, 10]$. Moreover, $\beta = 0.4$ depicts a more erratic behavior in the observed range; a 1:1 ratio is favored by $\alpha = 0.6$. Both perturbations from 0 perform in general better than the baseline case. However, the parameter α does not appear in Lowe's method, which entails that Lowe's method can only benefit from $\beta = 0.4$. Given all of the above, we conclude that the optimal choice is

$$\boxed{(\mu, \alpha, \beta) = (0, 0.6, 0), \text{ weighted staggering: Verlet}}$$

$$\boxed{(\mu, \alpha, \beta) = (0, 0, 0.4), \text{ weighted staggering: Lowe}}$$

and the convergence under these parameters will be investigated in the following section for the vV and Lowe's staggered methods.

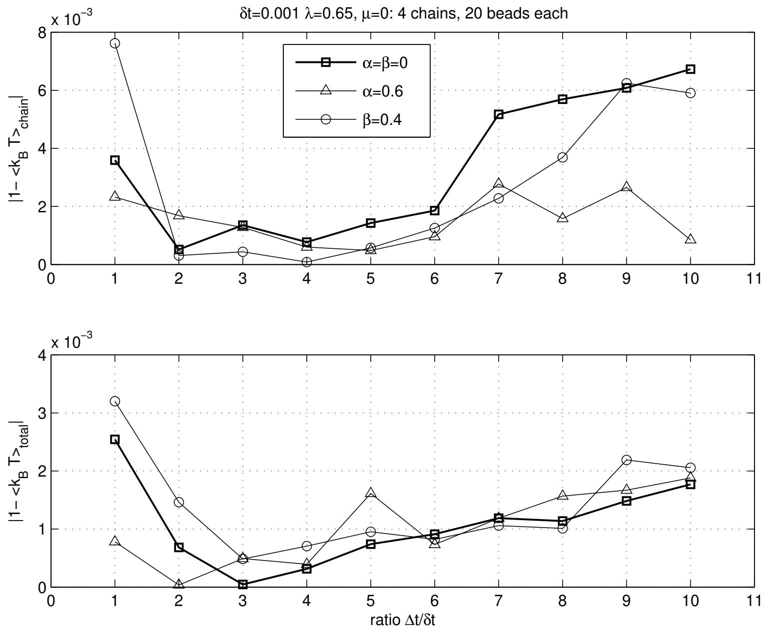

Figure 6.5: Maximum absolute error in total and chain $k_B T$ versus $\mathbb{K}$ for the optimal parameters compared to the baseline case of $\alpha = \beta = \mu = 0$. Results from the vV scheme are shown.

6.2.4 Optimal Cases with Weighted Staggering: Safe and Ambitious Ranges

Revisiting the safe and ambitious timestep ranges, figure 6.6 summarizes accuracy results for both methods with weighted time-staggering for the chain and total kinetic temperature in the safe range. It serves as a guideline on the effect of the time-staggering *alone*. Both methods prove to perform well even for ratios $\mathbb{K} = \frac{\Delta t}{\delta t} = \frac{10}{1}$. The vV scheme shows a more erratic dependence on $\mathbb{K}$ on individual polymer chains, but proves to be more accurate in this δt regime than Lowe's method as a whole (i.e., for $k_B T_{\text{total}}$).

The accuracy tests in the ambitious range with the optimal parameters show a clear advantage of the proposed schemes compared to the baseline case. Even for $\mathbb{K} = 4$, vV and Lowe's methods produce an error of $\{1.9, 4.1\} \times 10^{-3}$ respectively, while the baseline case values are $\{50.3, 1.8\} \times 10^{-3}$. Clear advantage therefore is achieved in the vV case for $\mathbb{K} \in [1, 6]$ while Lowe's method shows almost the same accuracy for both the baseline and the optimal cases. Moreover, the dependence on $\mathbb{K}$ is now *monotonic*, an attractive improvement from the baseline case.

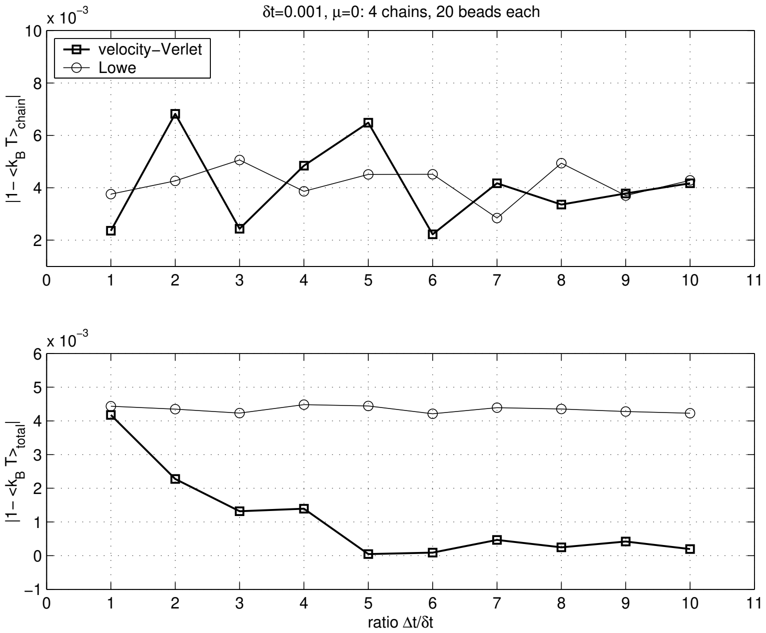

Figure 6.6: Comparison of the vV ($\alpha = 0.6$) and Lowe's ($\beta = 0.4$) schemes using the optimal relaxation parameters and weighted time-staggering for the *safe* range.

6.3 Computational Complexity

CPU-time savings is the basic motivation for using a time-staggered scheme with two different time-steps. Figure 6.8 summarizes results for four different chains in a 4000 DPD-particle simulation, each having 20, 50 and 100 beads. Efficiency depends (among other factors) on how the intra-polymer pairwise interactions are handled. Since all the forces are pairwise, it is customary not to explicitly compute all the pairs in the domain, but to introduce *neighbor* (or *cell*) lists or boxes and search only in them [101]. This dramatically reduces the computational cost, which would be quadratic in N (the total number of DPD particles). Although we use a brute-force method for searching through all the pairs in a chain, an $\mathcal{O}(M^2)$ operation for M beads, further improvement can be achieved by using a linked-list method for the polymer chain, as is done for the solvent. This would be beneficial only for large chains. If we consider a staggered simulation of $\{\Delta t, \delta t\}$

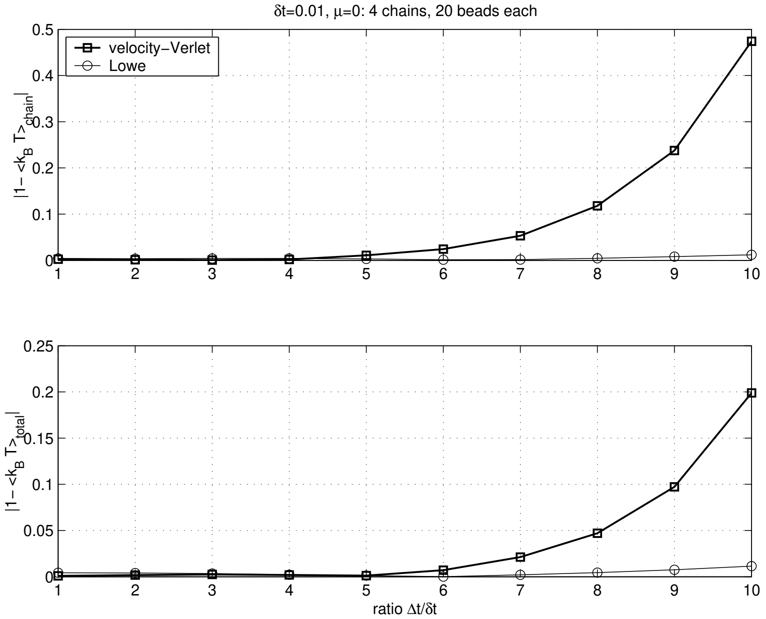

Figure 6.7: Comparison of the vV ($\alpha = 0.6$) and Lowe's ($\beta = 0.4$) schemes using the optimal relaxation parameters and weighted time-staggering for the *ambitious* range.

time-steps, the speed-up of the method is defined as the ratio

$$\text{speed-up} = \frac{[\text{total CPU-time for a } \delta t \text{ simulation}]}{\left[\begin{array}{c}\text{total CPU-time to advance to the same solution} \\ \text{time for a hybrid staggered } \{\Delta t,\, \delta t\} \text{ simulation}\end{array}\right]}$$

The chosen polymer force largely influences the speed-up, since LJ interactions require calculations of all possible pair combinations, while spring forces alone do not. Figure 6.8 shows small differences in the speed-up between the two methods. The speed-up is almost linear in dilute solutions with polymers formed by shorter chains. Larger chains show reduced (sub-linear) speed-up. In our example of brute-force pair searching for 100-bead chains, we still achieve a speed-up of 8 for $\frac{\Delta t}{\delta t} = 10$. We expect the schemes to show reduced efficiency *only* for the special case of non-dilute solutions of large polymer chains. In that case results could be further improved by introducing an extra neighbor list for bead-bead force calculations. If non-bonded interactions are present, the latter might not even be necessary.

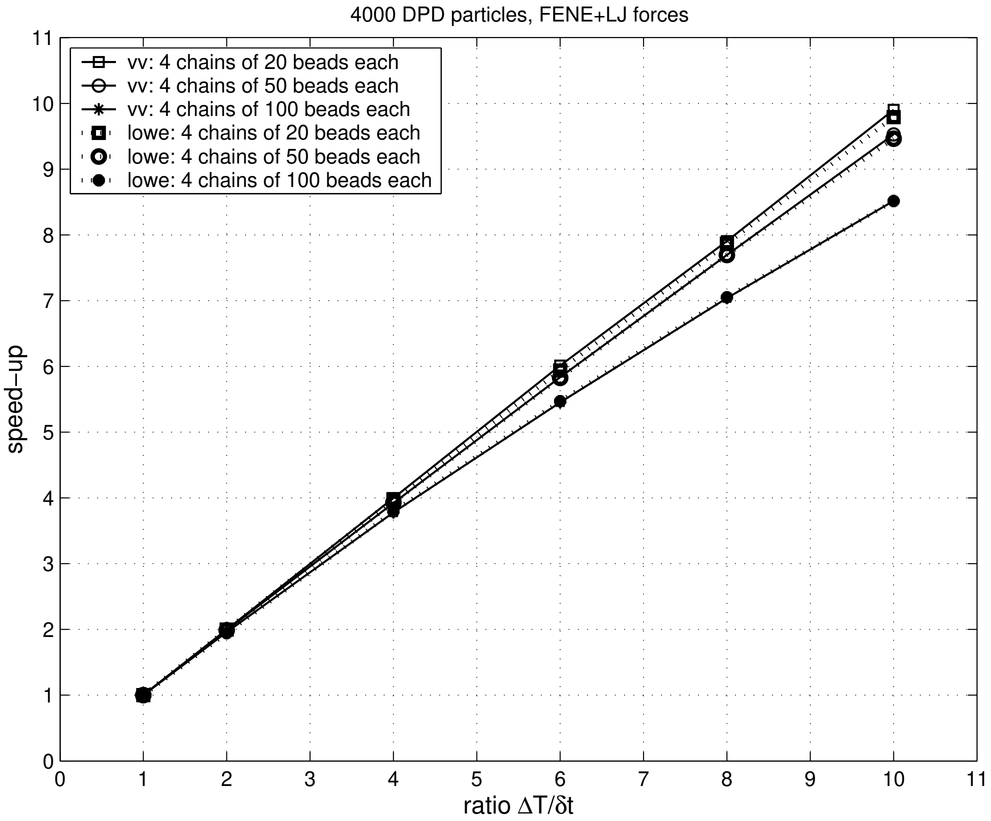

Figure 6.8: Speed-up results versus $\frac{\Delta t}{\delta t}$ for the vV and Lowe's methods for a 4000 DPD-particle fluid. The polymer beads interact with each other through a FENE force and a pairwise LJ hard repulsion.

Chapter 7

Applications to Complex Fluids

7.1 Scaling Laws in Polymers

7.1.1 The Static Exponent ν

Since our DPD models represent, in effect, dilute polymer solutions, the dynamics of a single flexible polymer chain is of great importance for validation and physical understanding of the DPD methods. An early work by Schlijper et al. [69] has used stiff (Fraenkel) and weak (Hooke) springs, without hard LJ potentials, to map polymer-chain scaling exponents to the DPD results. Our work introduces more complex (non-linear) forces combined with hard repulsions for various spring laws. This serves the double objective of validating the DPD simulation method as well as introducing novel combinations of interactions (such as the Fraenkel spring coupled with bead-bead repulsions).

It has been known that ideal chains are characterized by a linear relation between force and elongation, and exhibit the phenomenon of *phantom collisions*, i.e. polymeric bonds are not restricted from passing through each other. On the other hand, real chains in good solvents behave like self-avoiding walks on a lattice and do not exhibit phantom collisions. In simulations this can be achieved by introducing a repulsive force between beads i, j of the form

$$\mathbf{F}_i^{\mathrm{EV}} = -\sum_j \frac{\partial}{\partial \mathbf{r}_i} U^{\mathrm{EV}}(\mathbf{r}_i - \mathbf{r}_j)$$

for excluded volume, given by the gradient of a potential $U^{\mathrm{EV}}(\mathbf{r}_{ij})$. We define the mean-square end-to-end distance of a chain of M beads as

$$\langle S^2 \rangle = \Big\langle \big(\sum_{i=1}^{M-1} \mathbf{l}_i \big) \cdot \big(\sum_{j=1}^{M-1} \mathbf{l}_j \big) \Big\rangle,$$

where $\mathbf{l}_i$ is the vector joining the i^{th} and $(i+1)^{th}$ bead, and the mean-square radius of gyration as

$$\langle {R_g}^2 \rangle = \Big\langle \frac{1}{M} \sum_{i=1}^{M} (R_i - R_{\mathrm{cm}})^2 \Big\rangle,$$

where R_i is the position vector of each bead, R_{cm} the position vector of the center of mass of the chain and $\langle \cdot \rangle$ denotes time averaging. Pierre de Gennes [102] considered two critical exponents for a single chain: γ, relating to chain entropy, and ν, relating to chain size. An ideal chain has a scaling law of $\nu = 0.5$, while a real chain with excluded volume follows the Flory formula $\nu = \frac{3}{d+2} = 0.6$, for three dimensions. The Flory formula can be considered *exact* for all practical purposes. DPD simulations of linear chains [69] have shown a close mapping to the 0.5 exponent, which in turn relates to the continuum Zimm model of harmonic springs [13], while some works, [77], have recovered $\nu \approx 0.6$ by manipulating solvent characteristics. In other words, R_g for ideal chains scales as

$$R_g \propto (M-1)^{0.5},$$

while measurements of scattered light intensity versus angle verify [102] the chain size power law to be

$$R_g \propto (M-1)^{0.6}.$$

7.1.2 Non-Staggered Schemes

Polymer Scaling

Our simulations aim to accurately describe real chains. We have performed a series of equilibrium simulations using combinations of the different polymeric forces outlined in section 5.6. We investigated the effect of linear and non-linear spring forces, and the effect of a pairwise LJ repulsion. The chain sizes vary from 5 to 100 beads,with $r_{\text{max}} = 2r_c, 3r_c, \kappa = \frac{1}{\lambda_p} = 7, r_{\text{eq}} = r_c, L_{\text{sp}} = 2r_c$. Integration time is 10,000 units with time-step $\Delta t = 0.01$.

Figure 7.1 summarizes results for different spring laws with and without bead-bead repulsions. The corresponding static exponent values (ν) of the radius of gyration are computed for each case, using 5-, 10-, 20-, 50- and 100-bead chains. The LJ repulsion seems to be mostly responsible for capturing *self-avoidance* while the underlying spring force (Hookean or FENE) appears to have a secondary effect on the scaling exponent, when coupled with hard repulsions. However, FENE forces alone scale close to the Flory exponent, rendering the model realistic without any additional repulsions. The FENE parameter r_{max} was also varied, with the values $2r_c$ and $3r_c$ giving very similar scaling laws (figure 7.1). The parameters for the Marko-Siggia spring were consistent with the rest of the models. However, different parameters, taken from DNA molecules, produced $\nu = \frac{1}{2}$ - indicative that the DNA-wormlike model in equilibrium operates mostly in the linear regime.

Comparison with the Random Flight Chain Model

The simplest possible polymer model consists of a backbone of bonds, consisting of fully flexible joints. Although this is an over-simplified concept, with the bonds lacking volume and mass, it usually serves as a good reference for more complicated association rules. The discrete version of this *random flight* model is based on the idea that each bead can only move on a regular three-dimensional lattice and there is no inherent restriction on the number of times it can visit a particular point on the lattice. This simplistic model features polymer back-folding and other

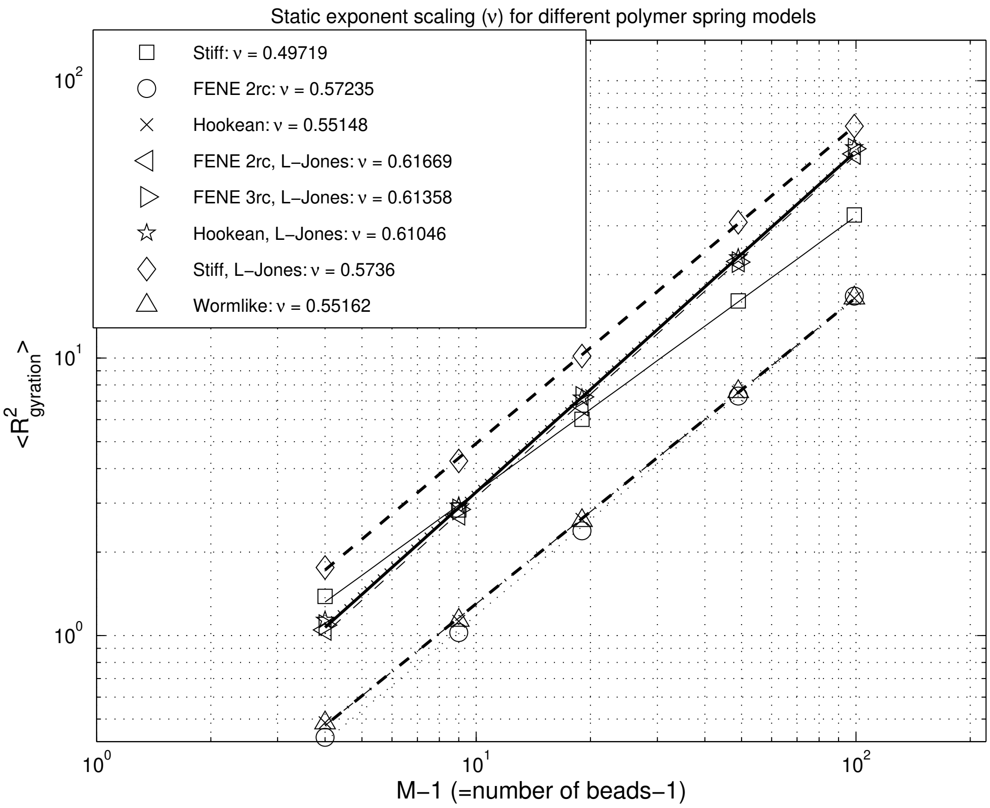

Figure 7.1: Scaling of the radius of gyration of a single polymer chain governed by linear, WLC and FENE forces and the effect of hard LJ potentials.

unphysical repercussions not exhibiting excluded volume effects.

Although random flight chains are three dimensional entities, each direction essentially behaves as a one-dimensional *random walk*. For a chain of M beads, it can be shown [103] that in the limit $M \longrightarrow \infty$ the distribution function $P(\mathbf{S})$ of the end-to-end distance vector $\mathbf{S}$ asymptotically obeys the Gaussian distribution. In that limit, it can also be shown that the mean-square end-to-end distance and the mean-square radius of gyration are related by

$$\frac{\langle S^2 \rangle}{\langle {R_g}^2 \rangle} = 6.$$

Figure 7.2 shows how the value of this ratio compares with a random flight chain for all the bead-spring models studied above.

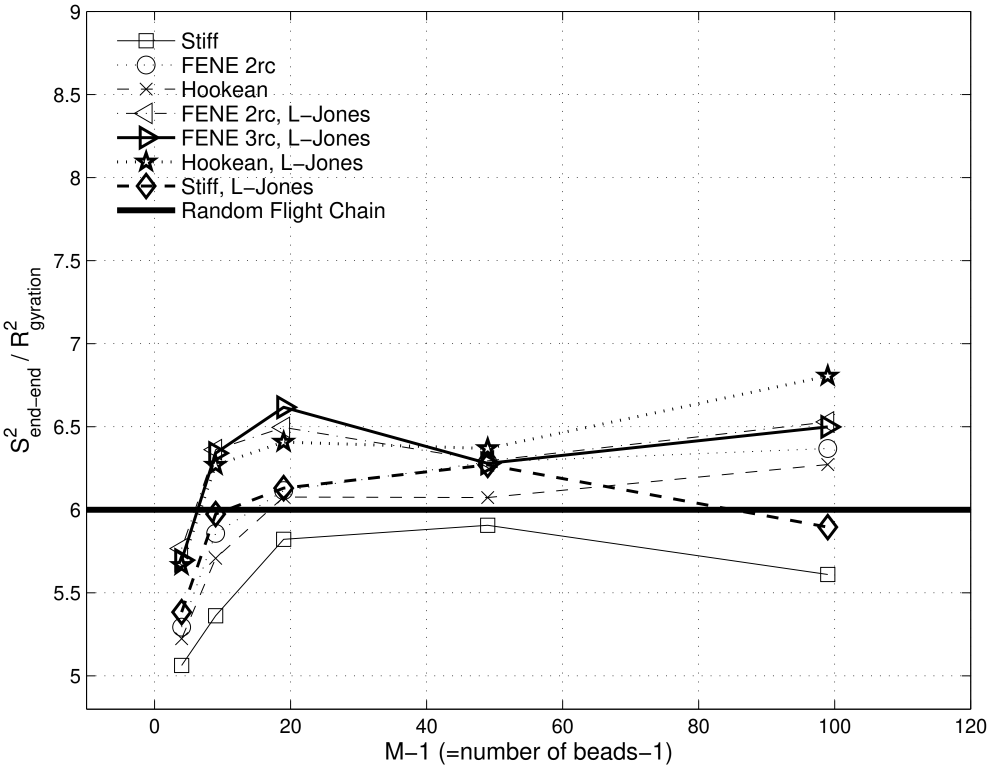

Figure 7.2: Ratio $\frac{\langle S^2 \rangle}{\langle {R_g}^2 \rangle}$ for various chain sizes (5, 10, 20, 50 and 100 beads). The simulation parameters are the same as in figure 7.1.

7.1.3 Staggered Schemes

To appreciate the practical potential of both the vV and Lowe time-staggered schemes in equilibrium we compute the static scaling law for $\mathbb{K} = \frac{\Delta t}{\delta t} = \{1, 6, 10, 20\}$ in the ambitious range $\Delta t = \{0.01, 0.06, 0.1, 0.2\}, \delta t = 0.01$ for one of the models of figure 7.1, namely FENE and LJ with $r_{\max} = 3r_c$. We note that the degenerate case of $\mathbb{K} = 1$ does *not* fully reduce to the classical, non-staggered schemes and therefore we cannot expect exact agreement of the staggered $\mathbb{K} = 1$ results with the results of section 7.1.2. The close agreement of ν depicted in figure 7.3 for this sample stiff polymeric system demonstrates the advantages in using such an algorithm: We obtain an almost linear speed-up (depending on the number of polymer chains present) in CPU-time, with negligible accuracy degradation in a time-step regime up to $\Delta t = 0.06$, i.e., twice the maximum possible ($\Delta t \approx 0.02$) if we had used a traditional integrator.

For the vV scheme $\mathbb{K} = 20$ is not an attainable value, since the scheme is inherently dependent on the chosen timestep and $\Delta t = 0.2$ is already large, even for non-polymer, non-staggered systems. Hence the maximum ratio we examine is $\mathbb{K} = 10$. For this value the observed solvent temperature is 23% higher than the set value, thus over-heating the polymer chain, rendering the radius of gyration larger. However, the static exponent still scales reasonably compared to the most accurate values of $\mathbb{K} = \{1, 6\}$. Lowe's scheme, on the other hand, shows smaller sensitivity to Δt; $\mathbb{K} = 10$ produces a $k_B T$ error $\sim 1\%$, but reaching $\mathbb{K} = 20$ is enough to show a significant deviation of 31% from the set temperature; similar effects on the polymer chain are observed.

Simulations in the absence of conservative forces were also performed in order to demonstrate their effect on the overall performance of the proposed schemes. Setting $a_{ij} = 0$ results in an ideal gas DPD fluid which Nikunen *et al.* [76] classified as a more challenging numerical problem. Figure 7.4 demonstrates a close agreement of the static scaling exponent for $\mathbb{K} = 1, 10$; the shifted difference between the curves being only the effect of $\Delta t = 0.1$ which drives the temperature up with an error of 8%.

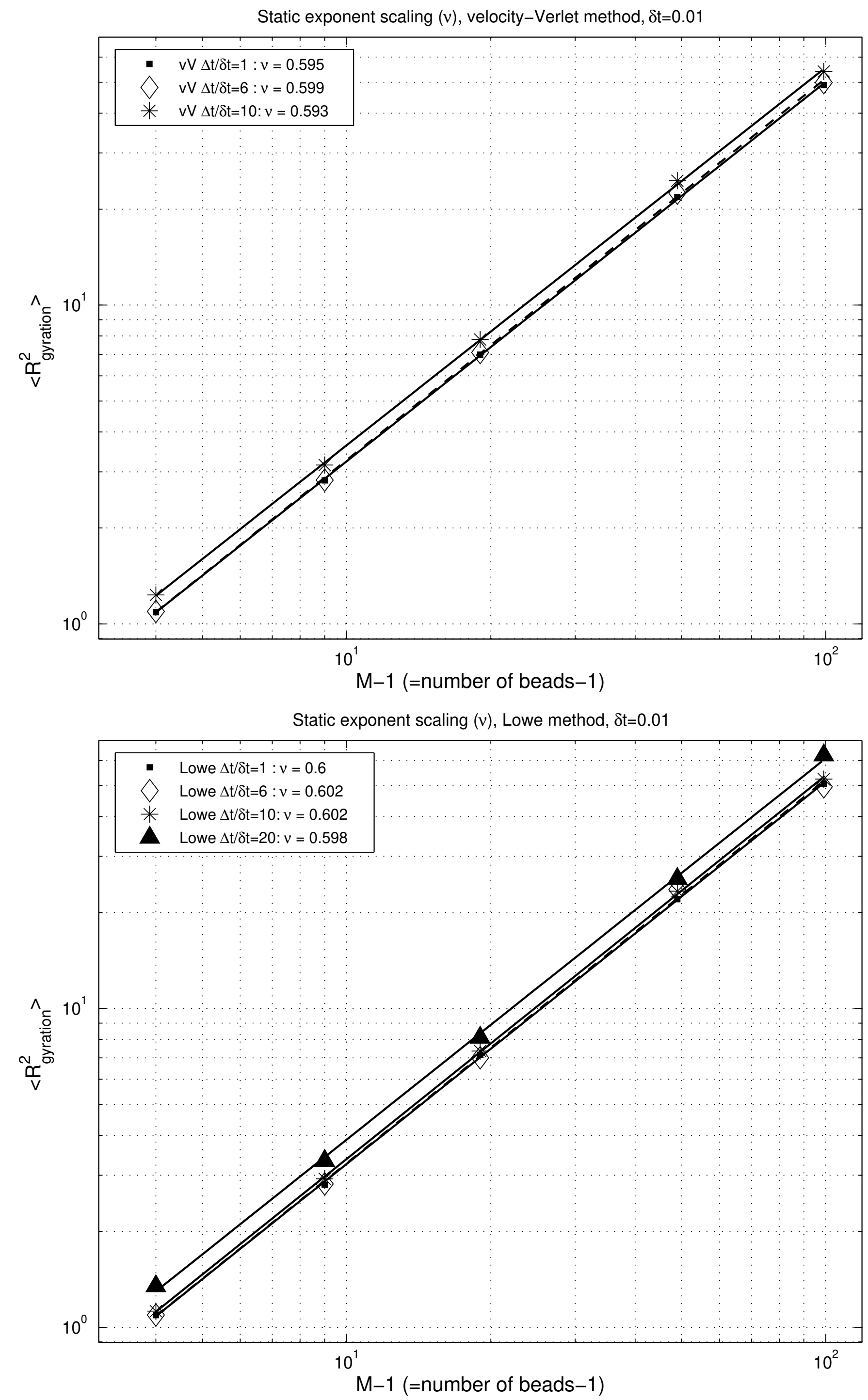

Figure 7.3: The effect of time-staggering on the scaling exponent ν of the radius of gyration of a single polymer chain governed by FENE and hard LJ potentials for the vV (upper) and Lowe's (lower) scheme.

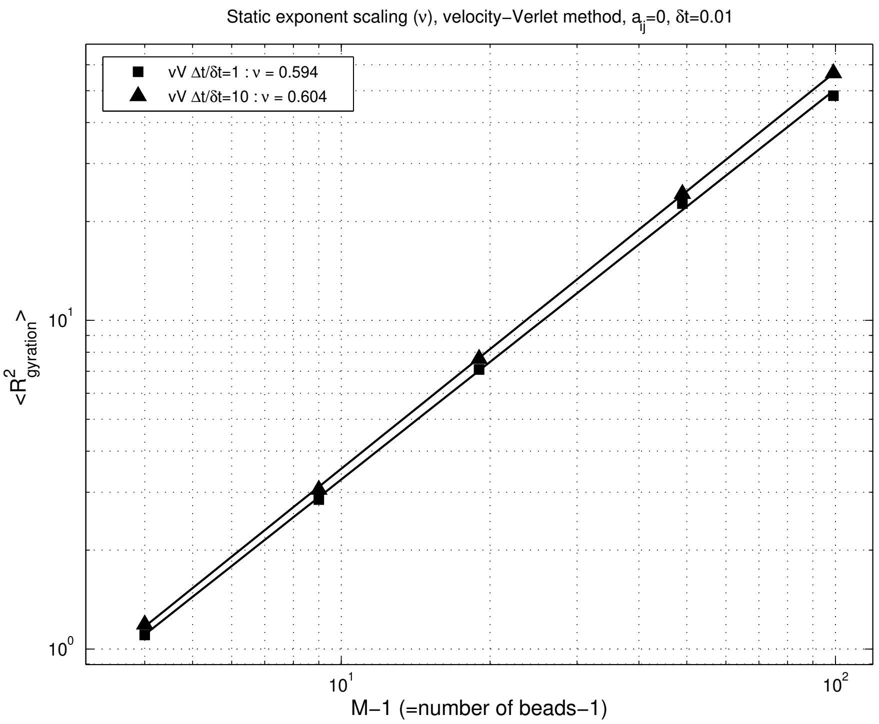

Figure 7.4: The performance of the staggered vV scheme in ideal gas conditions ($a_{ij} = 0$). The parameters are otherwise the same as in Figure 7.3 (top).

7.2 Shear Response of Wormlike Chains

The results presented in this section aim to simulate the response of λ-phage DNA molecules under steady shear, and compare the DPD results with corresponding results from Brownian Dynamics (BD) and experimental data. The wormlike chain (WLC) described in section 5.6 is used for all DNA simulations and Underhill and Doyle's [98] persistence length (λ_p) correction always applies to our results for $M > 2$. Bouchiat's [96] correction for the dumbbell case produced statistically similar results to the original Marko-Siggia (M-S) model. Since the λ_p correction studies in [98] were done with the M-S formula, we do not use Bouchiat's version.

DNA molecules under steady shear have been extensively studied in experimental [3] and computational [5, 92] works. In 1999, Smith *et al.* [3] performed a benchmark study of λ-DNA molecules in uniform shear flow of shear rates $\dot{\gamma} < 4.0s^{-1}$ employing a $\sim 50\mu m$ channel in solvents with viscosities $\mu = 60, 220cP$. These stained bacteriophage molecules have a contour length

$L \sim 21\mu m$ and longest relaxation times of $6.3s$ (in the $60cP$ solution) and $19s$ (in the $220cP$ solution). A typical molecule contains roughly 400 persistence lengths and hence can be considered *flexible*. Using DPD we investigated the dynamics of a single WLC. The moving boundaries at $y = 0, y = L_y$ are modeled using Lees-Edwards boundary conditions [104]: particles leaving the domain at $y = 0, L_y$ are advanced/retarded by an increment of $\Delta r = U_x t, -U_x t$ respectively in the $x-$direction, where t is the time elapsed from an appropriate origin of times and U_x denotes twice the shear velocity of each boundary. Moreover, the velocity of the particle is increased/decreased by $U_x, -U_x$, accounting for both the imposed boundary condition and the velocity discontinuity between the two walls. This correction is essential, since the dissipative forces depend on the relative pairwise velocities. The rest of the boundaries are treated periodically for all the solvent DPD particles. To avoid unphysical periodicity artifacts, polymer beads *only* undergo an elastic collision in the y-direction: $(u, v, w)_{\text{BEAD}} \rightarrow (u, -v, w)_{\text{BEAD}}$ and $r_y \rightarrow r_y - (\Delta t)v_{\text{BEAD}}$. Different chain sizes were accommodated by storing the polymer coordinates without mapping them back in the original domain. This allowed the intra-polymer forces to be calculated properly, while the collective solvent-solvent and polymer-solvent interactions were calculated with the mapped (periodic) images. The effect of the simulation box size $L_x \times L_y \times L_z$ for the presented results was investigated and proved to be negligible. For the results shown, a periodic box of dimensions $10 \times 20 \times 5$ was used in a fluid of 4000 DPD particles. The conservative force amplitude was fixed to $a_{ij} = 75k_B T/\rho$, as in [71].

In order to properly simulate λ-phage DNA molecules under steady shear, we define the dimensionless Weissenberg number of the flow as $We = \dot{\gamma}\tau$, for a shear rate $\dot{\gamma}$. Here, τ is the polymer's longest relaxation time, which is computed by fitting an exponential analytical curve to the average mean-square extension; this is *not* necessarily the end-to-end value. In particular, we define the maximum projected average molecular extension $\langle x \rangle$ of a polymer chain under shear in the x-direction as the maximum absolute difference of the x-coordinates of all the beads averaged in time, i.e., $\langle x \rangle := \langle |\min(\mathbf{r}_x) - \max(\mathbf{r}_x)| \rangle$ for all $\mathbf{r}$ belonging to a chain. The exponential fitting approach provides a relaxation time nearly the same (within 10%) as that obtained by fitting the late-time tail of the mean-square radius of gyration $\langle {R_g}^2 \rangle$. Figure 7.5 shows the fitted results. The calculated mean-square extension of an initially 30%-extended chain was fitted with $\langle x^2 \rangle = \langle x^2 \rangle_0 + {x_i}^2 e^{-t/\tau}$ to obtain the chain relaxation time τ. Here, ${x_i}^2$ is the initial stretch and $\langle x^2 \rangle_0$ is the equilibrium value. Equating the area under both curves fixed the free parameter of the fit.

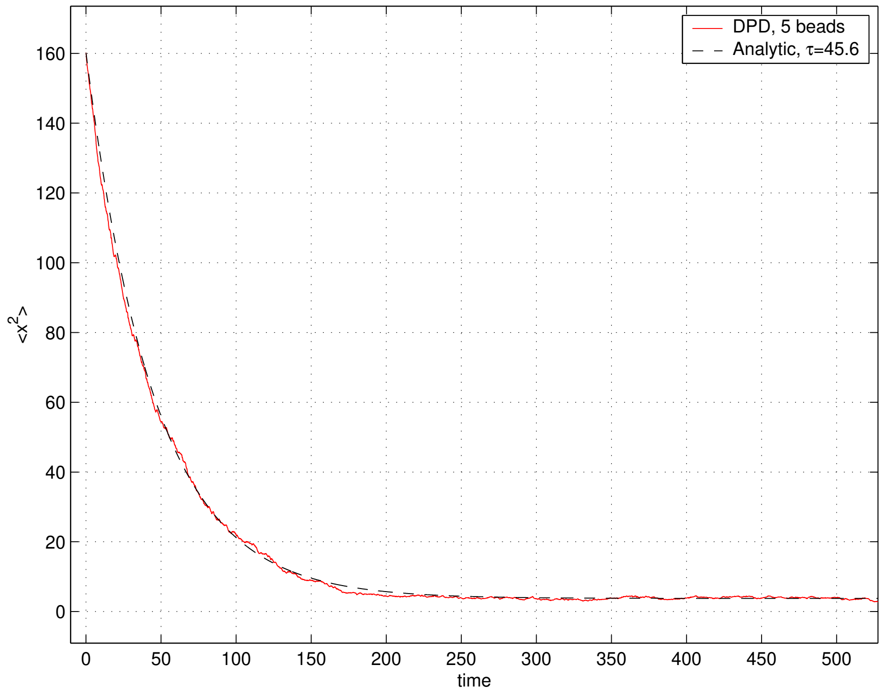

Figure 7.5: Decay of the average mean-square extension $\langle x^2 \rangle$ and the corresponding exponential fit for a wormlike chain of 5 beads in a Newtonian solvent using Lowe's non-staggered method ($\Gamma = 4.5$).

7.2.1 Non-Staggered Schemes

Figure 7.6 shows the calculated maximum projected average molecular extension $\langle x \rangle$ and the experimental data [3] versus We, with varying bead numbers and corresponding relaxation times. The asymptotic value for 20 beads (≈ 0.51) is in agreement with the corresponding one (0.47) from BD calculations [5]. Remarkably, the results for the average extension are not so sensitive to coarse-graining, i.e. the number of beads used for constant L, in the tested range. The self-

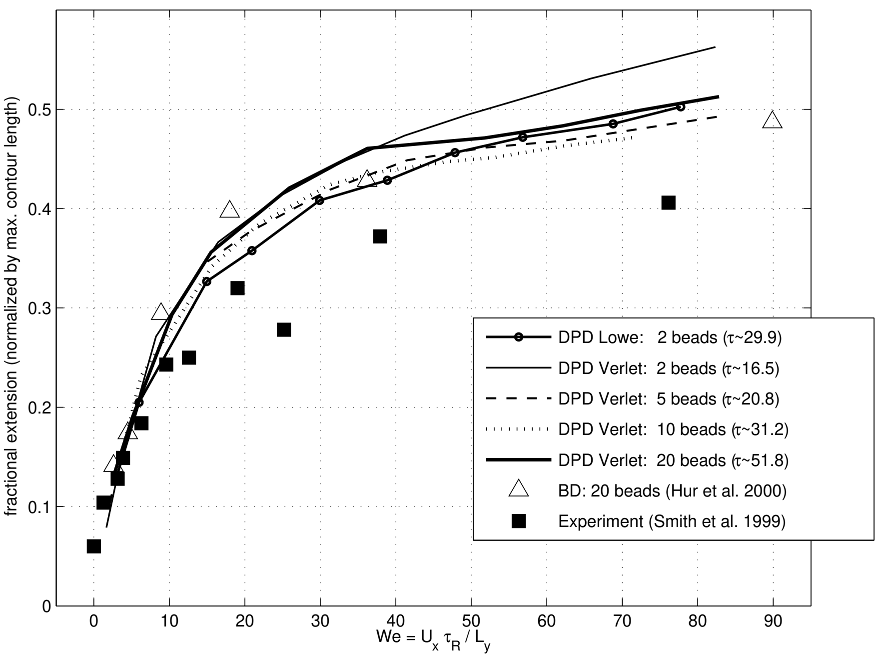

Figure 7.6: Mean WLC fractional extension versus We compared to BD [5] and DNA experiments [3] data. The results presented use the non-staggered vV ($\sigma = 3$) and Lowe schemes ($\Gamma = 4.5$).

consistency of the parameters was verified from the equilibrium mean-square end-to-end distance of a 2-bead dumbbell, computed as $\langle S^2 \rangle \approx 8.56$, in close agreement with the theoretical value of 8.92 given by [95] $\langle S^2 \rangle = 2L_{\text{sp}}\lambda_p \left(1 - \frac{\lambda_p}{L_{\text{sp}}}(1 - e^{-L_{\text{sp}}/\lambda_p})\right)$. While most results presented in this work employ the widely used velocity-Verlet scheme for time integration, in figure 7.6 we have also included results for 2 beads using Lowe's method. Figure 7.7 compares the calculated normalized autocorrelation function $\langle \Delta x(t) \Delta x(t+T) \rangle, \Delta x(t) = x(t) - \langle x(t) \rangle$ for 2-, 5- and 20-bead chains, with experimental data [3]. The products for each pair were collected from single-chain simulations in time bins with $\frac{\tau[\text{DPD}]}{\tau[\text{EXP}]} \times \frac{1}{\Delta t}$ sample points, $\tau[\text{DPD}]$ being the longest relaxation time in DPD units for each case, $\tau[\text{EXP}]$ typically fixed to 6.3 and Δt the simulation timestep, as done in [3]. The figure demonstrates the sensitivity of the autocorrelation to coarse-graining of the M-S force-extension formula. Significant degradation in the agreement with experiments appears for more than 5 beads. This shows the limits of the coarse-graining of a mesoscopic relation such as M-S. The M-S formula gives the average end force of a chain consisting of a large number of micro-elements (bead-rods freely rotating at fixed bond angles). The coarse-grained counterparts of the M-S chains rotate about their beads with any bond angle.We have compensated for this freedom by altering λ_p in the M-S formula for the sub-chains in the spirit of [98]. Clearly, a 2-bead dumbbell cannot describe the instantaneous configurations of DNA observed by [3]. If their capture is the objective of simulation, then the model needs to consist of a large number of micro-elements such as the 220 freely-rotating, bead-rod chains of [5]. With fixed bond angle these become the micro-elements of the WLC, widely considered to be an appropriate model for DNA. To date their simulation has not been attempted.

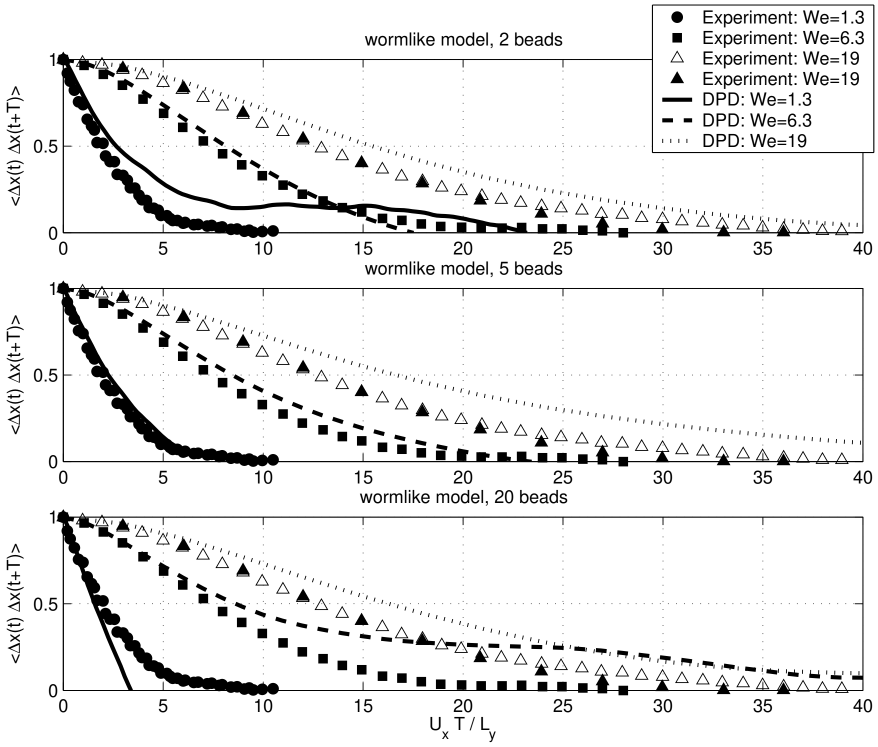

Figure 7.7: Autocorrelation of molecular extension x versus $\dot{\gamma}T$, compared with experimental DNA [3] data, for various We using the non-staggered vV scheme.

7.2.2 Staggered Schemes

Non-equilibrium configurations present an additional challenge on the performance of the integrating schemes. In order to demonstrate the accuracy of the proposed algorithms, we examine the effect of two different time-steps on physical quantities such as the mean maximum projected molecular extension under steady shear. Having established a satisfactory performance of Lowe's method with $\mathbb{K} = 6, 10$ in equilibrium, Figure 7.8 demonstrates the performance of the method for the same time-step ratios under shear for a 5-bead WLC, and compares the results with BD [5] and experimental data [3]. The time-staggered scheme produces a slightly larger molecular extension $\langle x \rangle$ for $\mathbb{K} = 6$ with a maximum disagreement not more than 10^{-2}, an extremely attractive result for all practical purposes, given the (almost linear) CPU savings. However, $\mathbb{K} = 10$ shows some degradation of the monitored averaged quantity, with a 7% disagreement at the high Weissenberg number regimes. The effect of the different Schmidt number ($Sc = \frac{\text{VISCOSITY}}{\text{DIFFUSIVITY}}$) is almost certainly excluded as a possible reason since $Sc \sim \Gamma^2$ and does not depend on Δt; indeed, a systematic calculation gives $Sc = 35, 28$ for $\mathbb{K} = 1, 10$, respectively, under these conditions. The limitations of the proposed schemes under shear are clear; non-equilibrium configurations impose extra constraints on the value of $\mathbb{K}$ while the errors become apparent at high shear rates. We will revisit the topic but we digress in the next section to discuss diffusion and the effect of Schmidt number (Sc) in the DPD simulations.

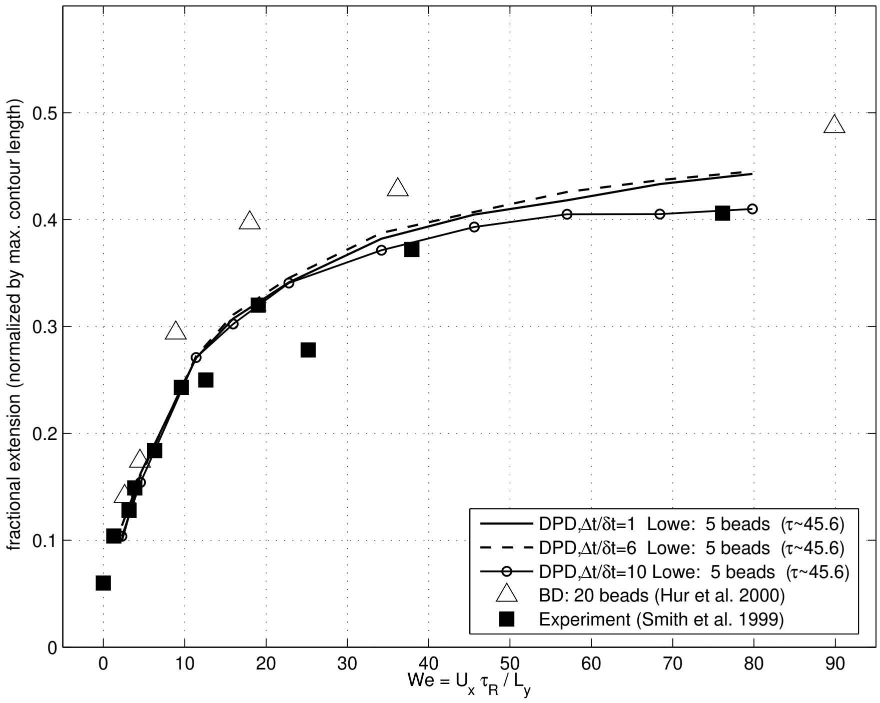

Figure 7.8: Effect of $\mathbb{K} = 1, 6, 10$ under shear. Maximum projected average extension of a 5-bead DNA molecule modeled by the M-S formula versus We. Here $\delta t = 0.01$, $\Gamma = 4.5$.

7.3 Dynamics: Diffusion and Viscosity

The characterization of the simulated fluid in DPD is of major importance for the understanding of the strengths and weaknesses of the method. In this section we examine fundamental quantities, such as kinematic viscosity $\nu = \frac{\mu}{\rho}$ and diffusion coefficient D_T and their dependence on the specific parameters of each DPD integrating scheme.

The peculiar velocity $\widetilde{\mathbf{u}}_i$ of particle i is defined as $\widetilde{\mathbf{u}}_i = \mathbf{u}_i - \bar{\mathbf{u}}(\mathbf{x})$, where $\bar{\mathbf{u}}(\mathbf{x})$ is the stream velocity at position $\mathbf{x}$. For a system of N particles of mass m_i each (in our simulations all particles are assumed to have unit mass), we define the $\alpha\beta$-component of the stress tensor through the Irving-Kirkwood formula [105]

$$S_{\alpha\beta} = -\frac{1}{L_x L_y L_z}\langle \sum_{i=1}^{N} m_i \widetilde{u}_{i\alpha}\widetilde{u}_{i\beta} + \sum_{i=1}^{N}\sum_{j>i}^{N} r_{ij\alpha}F_{ij\beta}\rangle, \tag{7.1}$$

where $F_{ij\beta}$ is the β-component of the net force acting on particle i due to particle j, and $r_{ij\alpha}$ is the α-component of their relative position vector. It is interesting to note here that equation 7.1 is directly applicable in its current form to the velocity-Verlet method but *not* Lowe's scheme, which lacks explicit calculation of dissipative/random forces. To this end, we propose a modification of equation 7.1 to incorporate the velocity re-equilibration $\mathbf{\Delta}_{ij}$ in Lowe's scheme interpreted as an additional force term:

$$S_{\alpha\beta} = -\frac{1}{L_x L_y L_z}\langle \sum_{i=1}^{N} m_i \widetilde{u}_{i\alpha}\widetilde{u}_{i\beta} + \sum_{i=1}^{N}\sum_{j>i}^{N} r_{ij\alpha}F_{ij\beta} + \sum_{i=1}^{N}\sum_{j>i}^{N} m_i r_{ij\alpha}\frac{\Delta_{ij\beta}}{\Delta t}\rangle, \tag{7.2}$$

where Δt is the timestep for the solvent (in the staggered scheme this would correspond to the maximum of $\{\Delta t, \delta t\}$). The dynamic viscosity μ of the fluid is determined under shear through the total shear stress S_{xy} (x is the direction of the shear and y the wall-normal direction) through

$$\mu = \frac{S_{xy}}{\dot{\gamma}}, \qquad \dot{\gamma} = \frac{U_x}{L_y},$$

and therefore the kinematic viscosity is $\nu = \frac{\mu}{\rho} = \frac{\mu L_x L_y L_z}{N}$. Here, $\dot{\gamma}$ is not to be confused with the dissipative force coefficient γ.

In this work we will, however, use a different approach for calculating the viscosity. Backer *et al.* [106] suggested the *periodic Poiseuille flow* method, which consists of simply superimposing a constant force $g_x, -g_x$ in the x-direction for all particles i with $\mathbf{r}_{i_y} > \frac{L_y}{2}$, $\mathbf{r}_{i_y} < \frac{L_y}{2}$ respectively. Then, for a periodic simulation box of length L_y in the $y-$direction, number density ρ, velocity profile $U(y)$ in the x-direction and dynamic viscosity μ the following formula holds:

$$\frac{\rho g_x (\frac{L_y}{2})^2}{12\mu} = \frac{2}{L_y} \int_{y=0}^{y=\frac{L_y}{2}} U(y) dy$$

Regarding the Poiseuille profile method, it is interesting to note that:

1. It eliminates possible artificial side-effects from imposition of other types of boundary conditions, since it results in a fully periodic flow with all the advantages spatial periodicity has to offer combined with a Poiseuille profile.

2. Both opposite Poiseuille profiles can be used to obtain better ensemble averages.

3. Backer *et al.* [106] have demonstrated that it is more accurate than other already existing methods.

4. Our studies for both vV and Lowe's methods indicate a negligible disagreement of $\mathcal{O}(10^{-4})$ between the computed viscosity values via the shear stress and Poiseuille flow methods, rendering both methods *equivalent* for all practical purposes.

Figure 7.9 shows such a profile with the corresponding averaged one, together with the parabolic least-squares fit. The area under the right curve can be calculated either by directly integrating the fitted quadratic or by standard integration rules. All results presented here use analytic integration of the fitted quadratic.

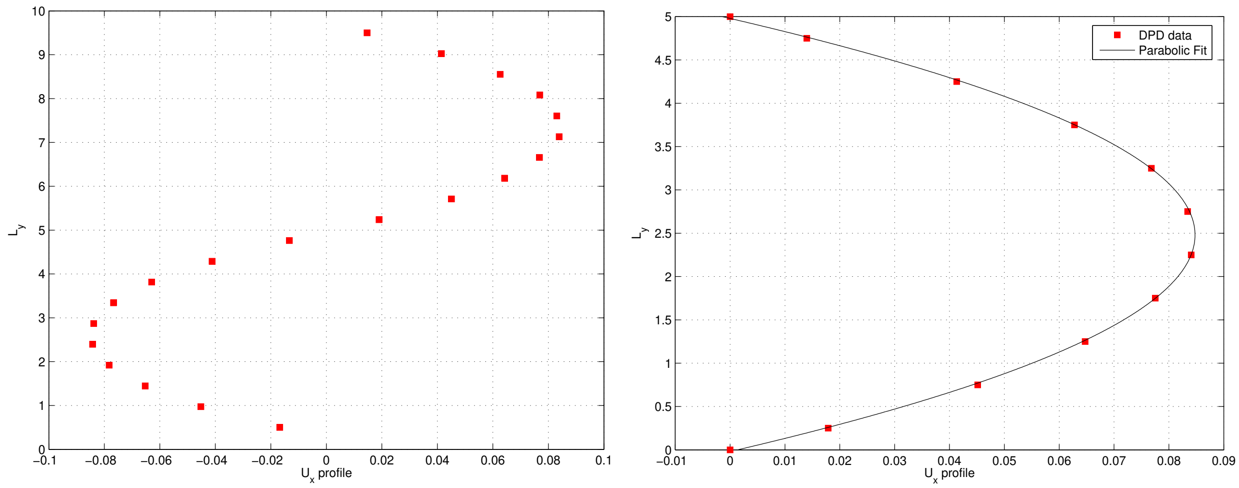

Figure 7.9: Sample dual parabolic (left) and reflected and fitted (right) profiles.

The velocity autocorrelation function (VAF) can reveal information for the underlying nature of a dynamical process. We construct it as follows: Given an appropriate origin of time, we denote the value of all three components of the velocity vector as $\mathbf{u}|_{t=0} = \{u|_{t=0}, v|_{t=0}, w|_{t=0}\}$. The velocity components at an arbitrary instant $0 \leq t = T$ are recorded, and the scalar quantity

$$C_u|_{t=T} = \frac{1}{N}\sum_{i=1}^{N} \mathbf{u}|_{t=0} \cdot \mathbf{u}|_{t=T}$$

is the VAF; for short, we write $C_u(t) = \langle \mathbf{u}_i(0) \cdot \mathbf{u}_i(t) \rangle$. The VAF provides valuable information about the system's underlying frequencies, and when it decays to zero as $t \to \infty$, it can be integrated to calculate the diffusion coefficient D_T:

$$D_T = \frac{1}{3}\int_{t=0}^{t=\infty} C_u(t) \quad dt.$$

This type of definition of a transport coefficient (such as D_T) through an integral of a correlation function is a *Green-Kubo* relation [107]. D_T may also be calculated through the mean-square displacement of each DPD particle. In practice, the initial value $\mathbf{u}|_{t=0}$ is reset during a simulation numerous times in order to collect meaningful ensemble averages that can be easily integrated. If the timestep is relatively small ($\delta t \approx 0.01$) the integral can be accurately calculated using a standard trapezoidal or midpoint rule.

The fundamental differences between the vV and Lowe's scheme manifest themselves in the values of the diffusion coefficient D_T, the viscosity ν and eventually the Schmidt number $Sc = \frac{\nu}{D_T}$ characterizing the simulated fluid. Groot and Warren [71] showed that the vV method for a number density $\rho = 3$ and a dissipation amplitude $\gamma = 6.75$ produced Schmidt number values close to those predicted by the theory, but extremely small compared to real fluids (three orders of magnitude smaller). We investigate this issue next.

7.3.1 The Schmidt Number for the Velocity-Verlet Scheme ($\delta t = 0.01$)

In order to investigate the effect of the dissipative and random coefficients γ, σ on the fluid, we compute D_T, ν and Sc for a wide range of values. Figure 7.10 shows the computed diffusion coefficient, viscosity and Schmidt numbers for a 4000-particle fluid, in a $10 \times 10 \times 10$ sized box with a time-step $\delta t = 0.01$ and a conservative force coefficient $a_{ij} = 75 k_B T/\rho$. For the viscosity calculations we apply a constant force of magnitude $g_x = 1$ as previously described to obtain a periodic Poiseuille profile. Groot and Warren [71] correctly argue that the vV scheme produces unrealistic values for Sc. The calculated value of $Sc = 1.00 \pm 0.03$ for $\sigma = 3.67, \rho = 3$ provided in [71] is in reasonable agreement with the one shown here ($Sc \sim 1.3$ for $\sigma = 3.5, \rho = 4$). The main point here is that the Schmidt number is $\mathcal{O}(1)$ for the vV method.

Marsh's [6, 108, 106] theoretical estimate on the kinematic viscosity $\nu(\sigma)$ for an ideal gas consists of a dissipative term that transfers momentum through particle collisions ($\sim \sigma^2$) and a kinetic contribution that transfers momentum through particle motion and displacement ($\sim \sigma^{-2}$), namely

$$\nu(\sigma) = \frac{45(k_B T)^2}{2\pi\sigma^2 r_c^3 \rho} + \frac{\pi\rho\sigma^2 r_c^5}{1575 k_B T}. \tag{7.3}$$

Figure 7.11 shows a reasonable agreement of the ideal gas prediction with the computed results. We compare the analytical expression (7.3) with the DPD values for conditions corresponding to

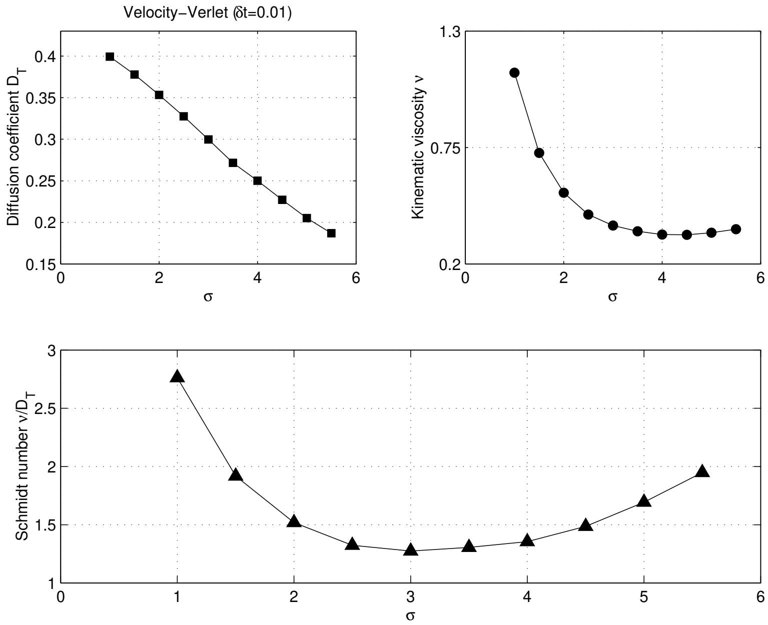

Figure 7.10: Diffusion coefficient D_T (upper left), kinematic viscosity ν (upper right), and Schmidt number Sc (lower) plotted against σ for vV. The Schmidt number is $\mathcal{O}(1)$. Here $k_BT = 1$.

ideal gas ($a_{ij} = 0$) and water ($a_{ij} = 75k_BT/\rho$). Next, we examine similar quantities for Lowe's scheme.

7.3.2 The Schmidt Number for Lowe's Scheme ($\delta t = 0.001, 0.01$)

For Lowe's scheme we investigate the same system and its dependence on the parameter Γ. To this end, we perform one series of simulations with $\delta t = 0.001$ and one with $\delta t = 0.01$. However, Γ is varied so that $\Gamma \times \delta t \in [1, 1000] \times 0.001 = [0.001, 1]$ and $\Gamma \times \delta t \in [1, 100] \times 0.01 = [0.01, 1]$, respectively. Although both vV and Lowe's schemes show a clear, monotonic dependence of D_T on the respective parameters σ and Γ, $D_T(\sigma)$ of vV is linear and larger in value compared to $D_T(\Gamma)$ of Lowe's scheme, which shows an asymptotic and non-linear trend, see Figures 7.12, 7.14.

For an ideal dissipative gas, Lowe's thermostat is governed by two distinct timescales, as shown in [7]; a typical time t_1 it takes a particle to travel a distance r_c with a given velocity, and a typical time t_2 it takes the velocity correlations to decay. Assuming the latter to be dependent only on Γ, we have

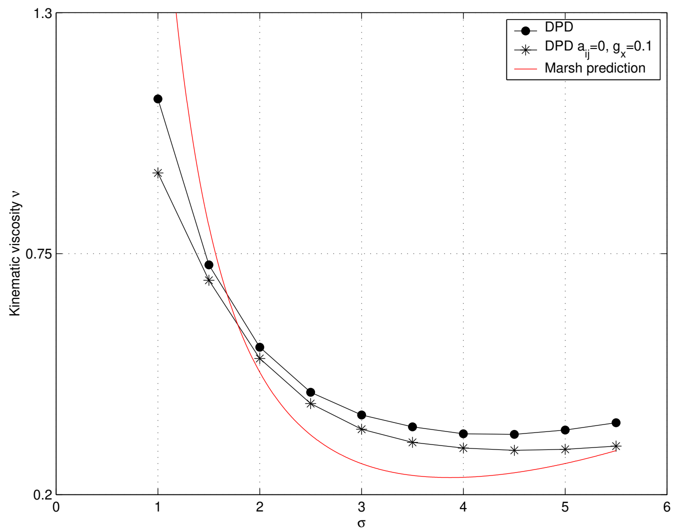

Figure 7.11: Kinematic viscosity ν plotted against σ for ideal gas and water repulsion parameters; the solid line corresponds to the theoretical ideal gas expression [6].

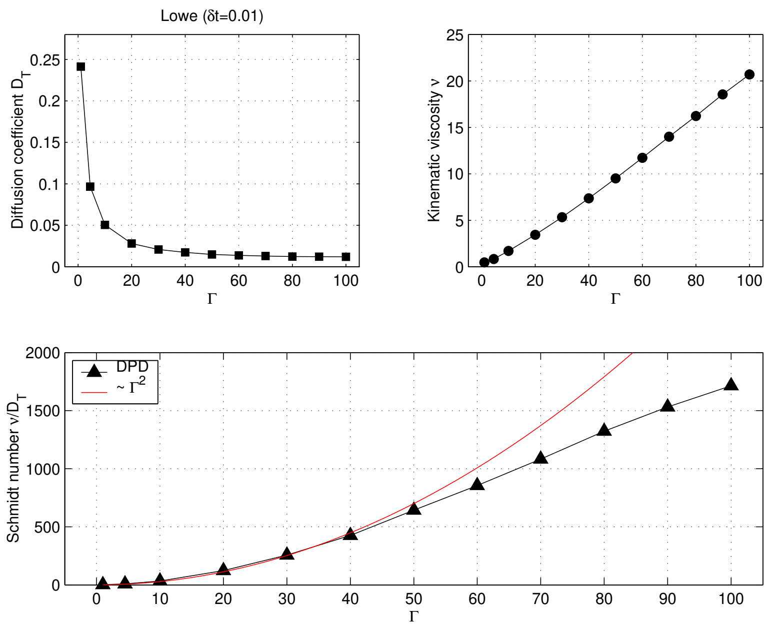

Figure 7.12: Diffusion coefficient D_T (upper left), kinematic viscosity ν (upper right), and Schmidt number Sc (lower) plotted against Γ for Lowe's scheme with $\delta t = 0.01$. The Schmidt number is $\mathcal{O}(10^3)$. Here $k_B T = 1$.

$$t_1 = \sqrt{\frac{mr_c^2}{k_B T}}, \quad t_2 = \frac{1}{\Gamma} \quad \Rightarrow \quad \Lambda = \frac{t_2}{t_1} = \sqrt{\frac{k_B T}{mr_c^2 \Gamma^2}}.$$

Hence, under the assumption that the velocity correlations decay in time is $\tau_D \sim \frac{1}{\Gamma}$, Lowe's scaling for the kinematic viscosity $\nu = \pi\rho\Gamma r_c^5/75m$ can be used to show that the Schmidt number

$$Sc = \frac{\text{VISCOSITY}}{\text{DIFFUSIVITY}} = \frac{\nu}{D_T} = \frac{\pi\rho\Gamma r_c^5/75m}{k_B T \tau_D/m} \sim \frac{1}{\Lambda^2} \sim \frac{\Gamma^2}{k_B T}.$$

Lowe, in his original paper [7] derives the above scaling, and our results in both figures 7.12, 7.14 verify this trend to be true for Γ values satisfying $0 \leq \Gamma \times \delta t \leq 0.5$. We anticipate the disagreement for large Γ values to improve if indeed an ideal gas ($a_{ij} = 0$) is simulated; in our simulations $a_{ij} = 75 k_B T/\rho$. Indeed, an ideal gas calculation of the above quantities was carried out and the quadratic dependence of the Schmidt number on Γ when $a_{ij} = 0$ is more pronounced - the results are shown in Figure 7.13. Lowe's method shows great potential in addressing the issue of realistic Sc values, since for the examined range of parameters the maximum Sc reaches values of $\mathcal{O}(10^5)$, i.e. five orders of magnitude larger than those of vV. Figures 7.12 and 7.14 show the dependence of the computed D_T, ν and Sc on Γ.

In the vV algorithm, the value of Schmidt number is around one for the studied parameters [71]. It is also worth mentioning that the Schmidt number for vV is estimated [108, 71] to follow $Sc \sim \frac{1}{2} + \frac{(2\pi\gamma\rho r_c^4)^2}{70875 k_B T}$. This expression makes it clear that the corresponding achievable values are not in the same order of magnitude as Lowe's scheme for comparable CPU requirements. We note, however, that in time-staggered algorithms the value of the parameter Γ should be kept the same as in the standard time-integrators in order to achieve the same value of Schmidt number in both cases. This is due to the fact that the diffusion coefficient scales as $\frac{1}{\Gamma}$ and it is approximately independent of the size of the timestep despite the fact that the product $\Gamma \times \Delta t$ controls the thermalization process in Lowe's method. Figure 7.15 shows that the relaxation time for a 5-bead

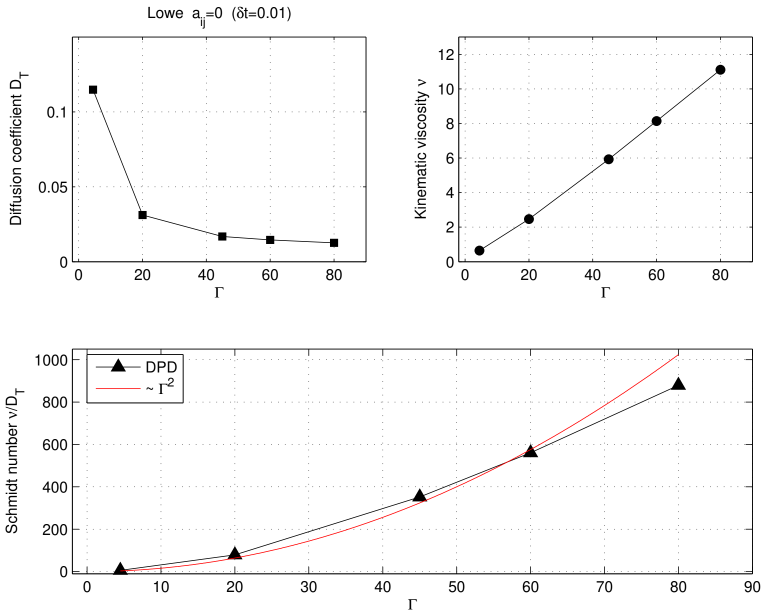

Figure 7.13: Diffusion coefficient D_T (upper left), kinematic viscosity ν (upper right), and Schmidt number Sc (lower) plotted against Γ for Lowe's scheme with $a_{ij} = 0$ and $\delta t = 0.01$. The Schmidt number is $\mathcal{O}(10^3)$. Here $k_B T = 1$.

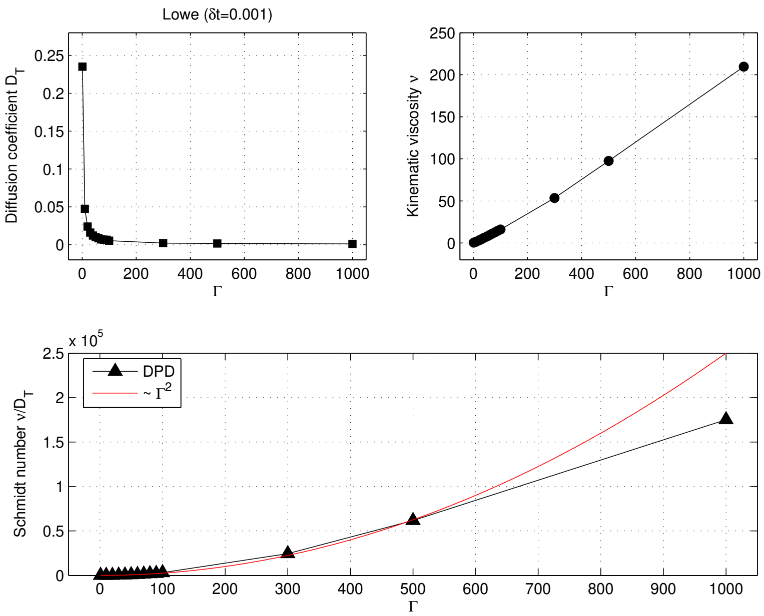

Figure 7.14: Diffusion coefficient D_T (upper left), kinematic viscosity ν (upper right), and Schmidt number Sc (lower) plotted against Γ for Lowe's scheme with $\delta t = 0.001$. The Schmidt number is $\mathcal{O}(10^5)$. Here $k_B T = 1$.

WLC scales roughly as $\sim \Gamma$ for Lowe's method. Intuition supports this, since viscosity scales linearly with Γ as well.

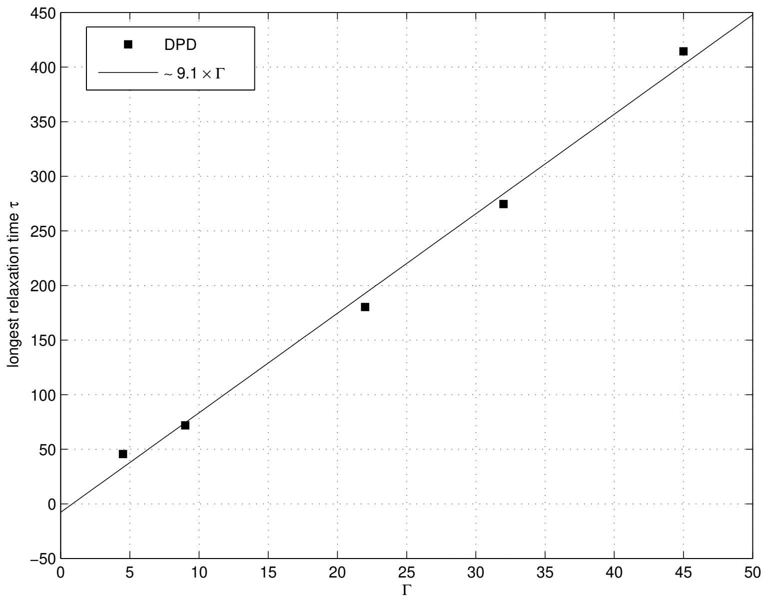

Figure 7.15: Longest relaxation time τ for the wormlike chain (5 beads) plotted against Γ for $k_BT = 0.2$.

7.4 Wormlike Chain and Lowe's Scheme: $\Gamma = 4.5, 22$ and 45.0

The Schmidt number results presented in Figure 7.12 motivate the re-calculation of the mean fractional extension of a wormlike chain molecule under shear. More specifically, since the parameter Γ controls the Schmidt number, and all the calculations in section 7.2 were done with $\Gamma = 4.5$ ($Sc \approx 35$), we repeat one case (the 5-bead chain) for $\Gamma = 22$ and 45. These values correspond to the more realistic $Sc \approx 690$ and 2574, respectively, at $k_BT = 0.2$. Figure 7.16 shows a much better agreement of the averaged values with the experimental data, verifying the consistency of the viscosity and diffusion calculations that the powerful alternative Lowe's scheme provides through the adjustment of Γ. Moreover, of interest is the monotonic dependence of the curves on Sc.

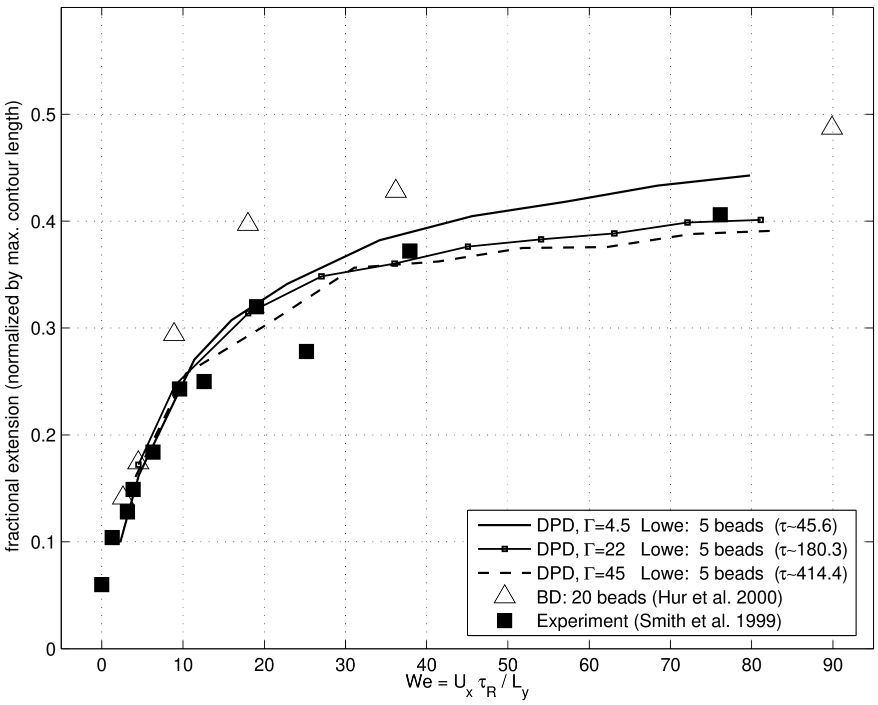

Figure 7.16: Time-averaged mean fractional extension of a 5-beaded wormlike chain under shear versus We for $\Gamma = 4.5$ ($Sc \approx 35$), $\Gamma = 22$ ($Sc \approx 690$) and $\Gamma = 45$ ($Sc \approx 2574$). Here $k_B T = 0.2$. An empirical approximate formula would be $Sc \approx 1.4 \times \Gamma^2$, in agreement with Lowe's arguments [7].

7.5 Effect of Schmidt Number on Polymeric Quantities

In this section we investigate the effect of Sc on the size of polymeric chains (measured through $\langle R_g^2 \rangle$) in equilibrium and steady shear, as well as their longest relaxation time τ. To this end, we refer to equation 7.3.2 to verify $Sc \sim \frac{\Gamma^2}{k_B T}$. Table 7.1 summarizes ν, D_T, Sc values for different combinations of $\Gamma, k_B T$. We include column IV as a baseline vV case for comparison. We use polymeric chains subject to FENE springs, with maximum extensibility $r_{\max} = 5r_c$, spring constant $\kappa = 30k_B T$ and number of beads per chain $M = 5$. The relaxation times for cases $Sc = \mathcal{O}(1)$ (columns IV, V) are crude approximations, since the corresponding relaxation curves do not follow exponential ones at such low values of Sc. Several conclusions can be drawn from the entries of Table 7.1:

- Columns I,II verify Lowe's prediction of equation 7.3.2, since the Schmidt numbers agree. More specifically, $Sc \sim \frac{\Gamma^2}{k_B T} = \frac{1^2}{0.01} = \frac{10^2}{1}$.

- Columns IV,V correspond to two distinct cases (vV, Lowe) having $Sc \sim 1$. It is, therefore, possible to tune Lowe's parameter Γ so that the vV fluid is properly simulated. Most values $(\nu, D_T, Sc, \tau, \langle R_g^2 \rangle)$ show reasonable agreement.

- All columns suggest that the effect of Sc on a FENE chain in equilibrium is minimal, as far as the static properties are concerned; here $\langle R_g^2 \rangle$. In other words, a flexible chain in a solvent of DPD particles assumes more or less the same size in equilibrium, regardless of the fluid surrounding it.

- Columns I,II suggest that agreement in Schmidt number of the solvent does not imply agreement in the longest relaxation time τ.

- Columns II,III,IV,V suggest that the size of the chain under steady shear is directly affected by the Schmidt number of the solvent at constant temperature; the disagreement between columns I,II for the shear $\langle R_g^2 \rangle$ values might be due to the difference in the root-mean-square velocity of the solvent particles ($\sqrt{\overline{v^2}} = \sqrt{\frac{3k_B T}{m}}$) and the shear velocity (constant for all

COLUMN	I	II	III	IV	V
	Lowe $\Gamma = 1$, $k_BT = 0.01$	Lowe $\Gamma = 10$, $k_BT = 1$	Lowe $\Gamma = 50$, $k_BT = 1$	vV $\sigma = 3$, $k_BT = 1$	Lowe $\Gamma = 0.45$, $k_BT = 1$
ν	0.1700	1.7240	9.5370	0.2784	0.2866
D_T	0.0046	0.0497	0.0149	0.2915	0.3100
Sc	~37	~35	~642	~0.96	~0.93
FENE: $\langle R_g^2 \rangle$	0.2244	0.2245	0.2250	0.2241	0.2241
FENE: τ	11.1	0.770	4.75	~0.262	~0.318
FENE: $\langle R_g^2 \rangle$ under shear with $\dot{\gamma} = \frac{1}{2}$	0.9486	0.2488	0.3809	0.2264	0.2270
We	5.550	0.385	2.375	0.131	0.159

Table 7.1: Dependence of different static and dynamic quantities on Lowe's parameter Γ, vV parameter σ and temperature k_BT ($\kappa = 30k_BT$, $r_{\max} = 5r_c$).

columns), since the former is a function of k_BT. Indeed, a rough calculation of the absolute values of the velocity components gives $\overline{|v|} \approx 0.08$ for $k_BT = 0.01$ and $\overline{|v|} \approx 0.8$ for $k_BT = 1$.

Chapter 8

Part II: Summary and Future Work

In part II of this dissertation we have introduced the basic Dissipative Particle Dynamics framework as an emerging method for mesoscopic simulations of fluids with complex microstructure. We outlined the need for a mesoscopic technique that addresses the different length- and time-scales of the solvent particles and the particles belonging to a polymer chain (beads), and we formulated the fundamental equations governing DPD simulations.

The main, novel contribution of this work to the numerical aspect of time-integration of the DPD equations is the new family of time-staggered schemes that can be readily employed as a small additional modification in existing DPD simulation codes. Irrespective of the specific intra-polymer conservative interactions (e.g., spring forces, excluded volume repulsions such as Lennard-Jones), the employment of two distinct timesteps $\{\Delta t, \delta t\}$ for solvent and polymer particles respectively, in certain systems involving stiff forces, greatly improves CPU-time efficiency. The widely-used velocity-Verlet method [71], together with Lowe's [7] alternative scheme, are the two integrators this work addresses. A new family of time-staggered schemes for both the velocity-Verlet and Lowe's methods are introduced, together with a set of relaxation parameters μ, α and β. Systematic analysis of the desired system and polymeric chain temperature k_BT under FENE and Lennard-Jones forcing shows that one can adjust these parameters to optimal ones; in our case these correspond to $(\mu, \alpha, \beta) = (0, 0.6, 0)$ for velocity-Verlet and $(\mu, \alpha, \beta) = (0, 0, 0.4)$ for Lowe's scheme. Another aspect of the advantage of the polymeric sub-cycling is the *weighted-staggering*, which, in effect, favors each sub-step accordingly taking into account the ratio of the current sub-step to the total number of sub-steps. The speed-up of the method depends on the number of beads per chain, the number of total chains and the way the pairwise search for non-bonded interactions is handled (neighbor list or brute-force pair searching). Under dilute solution conditions with relatively short- and medium-sized chains the speed-up is almost linear.

Physical applications of the polymer solutions DPD is able to describe include the scaling of the static exponent ν for various spring laws, and the effect of excluded volume interactions. The Marko-Siggia [25] wormlike chain is heavily used in this work as a mesoscopic, averaged model, able to describe the force-extension behavior of λ-phage DNA molecules. Assuming persistence and contour length values taken from real, stained molecules, we show good agreement of the mean fractional extension $\langle x \rangle$ of the WLC under shear for both the velocity-Verlet and Lowe's schemes. Furthermore, the aspect of diffusivity and viscosity (and eventually the Schmidt number, Sc, for each fluid) is addressed. For the range of parameters σ, Γ examined, the velocity-Verlet method is able to reach Sc values of $\mathcal{O}(1)$, while Lowe's scheme reaches values of $\mathcal{O}(10^5)$ by simply adjusting the thermalization parameter Γ; the Schmidt number for the velocity-Verlet method is not as sensitive on the choice of σ. Revisiting the comparison of $\langle x \rangle$ of the WLC under shear with experimental data from [3] we recover a much better agreement when we increase the Sc values to realistic ones for Lowe's scheme. Since $Sc \sim \Gamma^2$, there seems to be no theoretical limit to the range of attainable Sc values for Lowe's scheme - an attractive aspect worth considering.

The great potential and advantage of DPD as a mesoscopic simulation method for complex fluids certainly lies in aspects that other methods, such as Brownian Dynamics, fail to address; complex geometry flows being one of them. As a relatively new technique, several DPD issues still remain open: high-order integrators, validation with experimental results and correct implementation of boundary conditions for complex geometries (some attempts have already appeared in [70, 109]). This work has performed direct comparison with some experimental and Brownian Dynamics results with good agreement. Issues of immediate research interest would also include:

- Computational efficiency compared with Brownian Dynamics
- Formal derivation of the integration order for the available DPD time-marching schemes
- A dual, coupled comparison of DPD with Molecular Dynamics and continuum hydrodynamics to verify the validity of the method at both limits
- Coarse-graining issues and how the parameter $N_m = \dfrac{(\partial\rho)_{\mathrm{MD}}}{(\partial\rho)_{\mathrm{DPD}}}$ can adjusted to achieve these limits
- Experimentation with conservative forces for the solvent other than the popular choice of $a_{ij}\left(1 - \frac{r_{ij}}{r_c}\right)$
- The implementation and comparison of existing, widely-used integrators with emerging ones, such as the extended Lowe's scheme suggested by Peters [75] and the recently proposed Nosé-Hoover-Lowe-Andersen thermostat [110]
- The simulation of macromolecules subject to extensional flow.

Appendix A

The Components of the Reiner-Rivlin Stress

In Cartesian coordinates $\{x, y, z\}$ the velocity field has components $\{u, v, w\}$, and with subscripts to denote the spatial derivatives the components of $\mathbf{B}$ can be arrayed as,

$$\mathbf{B} = \begin{pmatrix} u_x - v_y - w_z & u_y + v_x & u_z + w_x \\ * & v_y - u_x - w_z & v_z + w_y \\ * & * & w_z - u_x - v_y \end{pmatrix} \tag{A.1}$$

The components of $\mathbf{B}^2$ are then

$$\begin{aligned} B^2_{\langle xx \rangle} &= (u_x - v_y - w_z)^2 + (u_y + v_x)^2 + (u_z + w_x)^2, \\ B^2_{\langle xy \rangle} &= (u_z + w_x)(v_z + w_y) - 2w_z(u_y + v_x), \\ B^2_{\langle xz \rangle} &= (u_y + v_x)(v_z + w_y) - 2v_y(u_z + w_x), \\ B^2_{\langle yy \rangle} &= (u_y + v_x)^2 + (v_y - u_x - w_z)^2 + (v_z + w_y)^2, \\ B^2_{\langle yz \rangle} &= (u_y + v_x)(u_z + w_x) - 2u_x(v_z + w_y), \end{aligned} \tag{A.2}$$

$$B^2_{\langle zz\rangle} = (u_z + w_x)^2 + (v_z + w_y)^2 + (w_z - u_x - v_y)^2.$$

It can be shown that

$$\frac{1}{2}\left[tr\mathbf{B}^2 - (tr\mathbf{B})^2\right] = (\nabla\cdot\mathbf{V})^2 + \omega^2 - 4\left[\frac{\partial(u,w)}{\partial(x,z)} + \frac{\partial(u,v)}{\partial(x,y)} + \frac{\partial(v,w)}{\partial(y,z)}\right], \tag{A.3}$$

where ω is the magnitude of the vorticity vector

$$\omega = \{\omega_{\langle x\rangle}, \omega_{\langle y\rangle}, \omega_{\langle z\rangle}\} = \{w_y - v_z, u_z - w_x, v_x - u_y\}. \tag{A.4}$$

From equation 3.24 the components of $\mathbf{C}$ can now be written as

$$\begin{aligned}
C_{\langle xx\rangle} &= -\omega^2_{\langle x\rangle} + 4\frac{\partial(v,w)}{\partial(y,z)},\\
C_{\langle xy\rangle} &= -\omega_{\langle x\rangle}\omega_{\langle y\rangle} + 2\frac{\partial(w,v)}{\partial(x,z)} + 2\frac{\partial(w,u)}{\partial(y,z)},\\
C_{\langle xz\rangle} &= -\omega_{\langle x\rangle}\omega_{\langle z\rangle} + 2\frac{\partial(v,w)}{\partial(x,y)} + 2\frac{\partial(u,v)}{\partial(y,z)},\\
C_{\langle yy\rangle} &= -\omega^2_{\langle y\rangle} + 4\frac{\partial(u,w)}{\partial(x,z)},\\
C_{\langle yz\rangle} &= -\omega_{\langle y\rangle}\omega_{\langle z\rangle} + 2\frac{\partial(v,u)}{\partial(x,z)} + 2\frac{\partial(w,u)}{\partial(x,y)},\\
C_{\langle zz\rangle} &= -\omega^2_{\langle z\rangle} + 4\frac{\partial(u,v)}{\partial(x,y)}.
\end{aligned} \tag{A.5}$$

If the three-dimensional field contains embedded, two-dimensional regions such as a plane of symmetry, where $w = 0$, and all derivatives $\frac{\partial(*)}{\partial z} = 0$, then inspection of equations A.5 confirms that all components of $\mathbf{C}$ are identically zero, except

$$C_{\langle zz\rangle} = -\omega^2_{\langle z\rangle} + 4\frac{\partial(u,v)}{\partial(x,y)}. \tag{A.6}$$

With the cross-plane gradient $\frac{\partial(C_{\langle zz\rangle})}{\partial z}$ being zero, $C_{\langle zz\rangle}$ has no dynamic effect. This result is independent of the magnitude of $(\nabla\cdot\mathbf{V})$. Equations A.5 are the same as they would be in the **A**-formulation with exact incompressibility.

Bibliography

[1] C. Chauvière. *Stabilized spectral element methods for the simulation of viscoelastic flows.* Ph.D. Thesis, EPFL, Lausanne, 2002.

[2] E. A. Kearsley. Intrinsic errors for pressure measurements in a slot along a flow. *Trans. Soc. Rheol.*, 14(3):419–424, 1970.

[3] D. E. Smith, H. P. Babcock, and S. Chu. Single polymer dynamics in steady shear flow. *Science*, 283:1724, 1999.

[4] A.S. Lodge and L. de Vargas. Positive hole pressures and negative exit pressures generated by molten polyethylene flowing through a slit die. *Rheol. Acta*, 22:151–170, 1983.

[5] J. S. Hur, E. S. G. Shaqfeh, and R. G. Larson. Brownian dynamics simulations of single DNA molecules in shear flow. *J. Rheol.*, 44(4):713–742, 2000.

[6] C.A. Marsh, G. Backx, and M.H. Ernst. Static and dynamic properties of dissipative particle dynamics. *Phys.Rev.E*, 56(2):1676–1691, 1997.

[7] C. P. Lowe. An alternative approach to dissipative particle dynamics. *Europhys. Lett.*, 47(2):145–151, 1999.

[8] D. N. Ku. Blood flow in arteries. *Annu. Rev. Fluid. Mech.*, 29:399–434, 1997.

[9] S. Chien. Shear dependence of effective cell volume as a determinant of blood viscosity. *Science*, 168(934):977, 1970.

[10] C.M. Rodkiewicz, P. Sinha, and J.S. Kennedy. On the application of a constitutive equation for whole human blood. *J. Biomech. Eng.*, 112(2):198–206, 1990.

[11] A.N. Beris and B.J. Edwards. *Thermodynamics of flowing systems with internal microstructure.* Oxford University Press, New York, 1994.

[12] R.G. Owens and T.N. Phillips. *Computational Rheology.* Imperial College Press, 2002.

[13] R. G. Larson. *The structure and rheology of complex fluids.* Oxford University Press, 1999.

[14] R. Larson. The rheology of dilute solutions of flexible polymers: Progress and problems. *J. Rheol.*, 49(1):1–70, 2005.

[15] A. Peterlin. Hydrodynamics of macromolecules in a velocity field with longitudinal gradient. *J. Polym. Sci. B*, 4:287–291, 1966.

[16] C.V. Chaubal and L.G. Leal. A closure approximation for liquid-crystalline polymer models based on parametric density estimation. *J. Rheol.*, 42(1):177–201, 1998.

[17] E.J. Hinch and L.G. Leal. Constitutive equations in suspension mechanics. Part 1. General formulation. *J. Fluid Mech.*, 71:481–495, 1975.

[18] E.J. Hinch and L.G. Leal. Constitutive equations in a suspension mechanics. Part 2. Approximate forms for a suspension of rigid particles affected by brownian rotations. *J. Fluid Mech.*, 76:187–208, 1976.

[19] J. Fang, M. Kröger, and H. C. Öttinger. A thermodynamically admissible reptation model for fast flows of entangled polymers. II. Model predictions for shear and extensional flows. *J. Rheol.*, 44(6):1293–1317, 2000.

[20] J. Fang and R. G. Owens. New constitutive equations derived from a kinetic model for melts and concentrated solutions of linear polymers. *Rheol. Acta*, 44:577–590, 2005.

[21] S. Chen and G. D. Doolen. Lattice Boltzmann method for fluid flows. *Ann. Rev. Fluid Mech.*, 30:329, 1998.

[22] D. R. Noble, S. Chen, J. G. Georgiadis, and R. O. Buckius. A consistent hydrodynamic boundary condition for the lattice Boltzmann method. *Phys. Fluids*, 7:203–209, 1995.

[23] P. A. Skordos. Initial and boundary conditions for the lattice Boltzmann method. *Phys. Rev. E*, 48:4823–42, 1993.

[24] P. J. Hoogerbrugge and J. M. Koelman. Simulating microscopic hydrodynamic phenomena with dissipative particle dynamics. *Europhys. Lett.*, 19(3):155–160, 1992.

[25] J. F. Marko and E. D. Siggia. Stretching DNA. *Macromolecules*, 28:8759–8770, 1995.

[26] A.N. Beris, R.C. Armstrong, and R.A. Brown. Spectral/finite-element calculations of the flow of a Maxwell fluid between eccentric rotating cylinders. *J. Non-Newtonian Fluid Mech.*, 22:129–167, 1987.

[27] J. Petera. A new finite element scheme using the Lagrangian framework for simulation of viscoelastic fluid flows. *J. Non-Newtonian Fluid Mech.*, 103:1–43, 2002.

[28] R.M. Phillips and T.N. Phillips. Flow past a cylinder using a semi-Lagrangian spectral element method. *Appl. Num. Math.*, 33:251–257, 2000.

[29] Y. Fan, R.I. Tanner, and N. Phan-Thien. Galerkin/least-square finite element methods for steady viscoelastic flows. *J. Non-Newtonian Fluid Mech.*, 84:233–256, 1999.

[30] C. Chauvière and R.G. Owens. A new spectral element method for the reliable computation of viscoelastic flow. *Comput. Methods Appl. Mech. Engrg.*, 190:3999–4018, 2001.

[31] M.A. Hulsen, A.P.G. van Heel, and B. H.A.A. van den Brule. Simulation of viscoelastic flows using brownian configuration fields. *J. Non-Newtonian Fluid Mech.*, 70:79–101, 1997.

[32] H.R. Warner. Kinetic theory and rheology of dilute suspensions of finitely extensible dumbbells. *Ind. End. Chem. Fundam.*, 11:379–387, 1972.

[33] A.P.G. van Heel, M.A. Hulsen, and B.H.A.A. van den Brule. On the selection of parameters in the FENE-P model. *J. Non-Newtonian Fluid Mech.*, 75:253–271, 1998.

[34] R. Sureshkumar, A.N. Beris, and R.A. Handler. Direct numerical simulation of turbulent channel flow of a polymer solution. *Phys. Fluids*, 9:743–755, 1997.

[35] C.D. Dimitropoulos, R. Sureshkumar, and A.N. Beris. Direct numerical simulation of viscoelastic turbulent channel flow exhibiting drag reduction: effect of the variation of rheological parameters. *J. Non-Newtonian Fluid Mech.*, 79:433–468, 1998.

[36] G.E. Karniadakis and S.J. Sherwin. *Spectral/hp Element Methods for CFD.* Oxford University Press, 1999.

[37] E. Tadmor. Convergence of spectral methods for nonlinear conservation laws. *SIAM J. Numer. Anal.*, 26(1):30, 1989.

[38] G.-S. Karamanos and G.E. Karniadakis. A spectral vanishing viscosity method for large-eddy simulations. *Journal of Computational Physics*, 162:22–50, 2000.

[39] S.M. Ould Kaber. A Legendre pseudospectral viscosity method. *Journal of Computational Physics*, 128:165, 1996.

[40] ∅. Andreassen, I. Lie, and C.E. Wasberg. The spectral viscosity method applied to simulation of waves in a stratified atmosphere. *Journal of Computational Physics*, 110:257, 1994.

[41] E. Tadmor. Super viscosity and spectral approximations of nonlinear conservation laws. In *Numerical Methods for Fluid Dynamics, IV. M.J. Baines and K.W. Morton, eds., Clarendon Press, Oxford*, page 69, 1993.

[42] H.-P. Ma. Chebyschev-Legendre spectral viscosity method for nonlinear conservation laws. *SIAM J. Numer. Anal.*, 35(3):901, 1998.

[43] H.-P. Ma. Chebyschev-Legendre super spectral viscosity method for nonlinear conservation laws. *SIAM J. Numer. Anal.*, 35(3):903, 1998.

[44] G.E. Karniadakis, M. Israeli, and S.A. Orszag. High-order splitting methods for incompressible Navier-Stokes equations. *Journal of Computational Physics*, 97:414, 1991.

[45] G.-S. Karamanos, C. Evangelinos, R.M. Kirby, and G.E. Karniadakis. DNS of turbulence on a PC/Linux cluster: Fact or fiction? In *Proc. SuperComputing*, 1999.

[46] M.G. Crandall and P.L. Lions. Viscosity solutions of Hamilton-Jacobi equations. *Trans. Amer. Math. Soc.*, 61:629, 1983.

[47] Y. Maday, S.M. Ould Kaber, and E. Tadmor. Legendre pseudospectral viscosity method for nonlinear conservation laws. *SIAM J. Numer. Anal.*, 30:321, 1993.

[48] E. Tadmor. Total variation and error estimates for spectral viscosity approximations. *Math. Comp.*, 60:245, 1993.

[49] R.M. Kirby. *Toward dynamic spectral/hp refinement: Algorithms and applications to flow-structure interactions.* Ph.D. Thesis, Brown University, 2003.

[50] R.H. Kraichnan. Eddy viscosity in two and three dimensions. *J. Atmos. Sci.*, 33:1521, 1976.

[51] M. Lesieur and O. Metais. New trends in large-eddy simulation. *Ann. Rev. Fluid Mech.*, 28:45, 1996.

[52] J.P. Chollet. Two-point closures as a subgrid scale modelling for large eddy simulations. In *Turbulent Shear Flows IV, ed. F. Durst and B. Launder, Lecure notes in Physics, Springer-Verlag*, 1984.

[53] C. Chauvière and R.G. Owens. A robust spectral element method for simulations of time-dependent viscoelastic flows. *J. Sci. Comput.*, 17:191–199, 2002.

[54] P. M. Coelho and F. T. Pinho. Vortex shedding in cylinder flow of shear-thinning fluids: I. identification and demarcation of flow regimes. *J. Non-Newtonian Fluid Mech.*, 110(2–3):143–176, 2003.

[55] B. Caswell. Non-Newtonian flow at lowest order: The role of the Reiner-Rivlin stress. *J. Non-Newtonian Fluid Mech., to appear.*

[56] R. Tanner and A. Pipkin. Intrinsic errors in pressure-hole measurements. *Trans. Soc. Rheol.*, 14:471, 1969.

[57] K. Higashitani and W. G. Pritchard. A kinematic calculation of intrinsic errors in pressure measurements made with holes. *Trans. Soc. Rheol.*, 16(4):687–696, 1972.

[58] W. O. Criminale Jr., J. L. Ericksen, and G. Filbey Jr. Steady flow of non-Newtonian fluids. *Arch. Ration. Mech.*, 1:410–417, 1958.

[59] M. W. Johnson Jr. Some variational theorems for non-Newtonian flow. *Phys. Fluids*, 3:871–878, 1961.

[60] R. Tanner. Some extended Giesekus-type theorems for non-Newtonian fluids. *Rheol. Acta*, 28:449–452, 1989.

[61] H. Giesekus. Die Simultane Translations - und Rotationsbewegung einer Kugel in einer Elastoviskosen Flüssigkeit. *Rheol. Acta*, 3:59–71, 1963.

[62] R. Tanner. Plane creeping flows of incompressible second order fluids. *Phys. Fluids*, 9:1246, 1966.

[63] P.P-L.Tong. *Fundamental studies on a laboratory stressmeter.* PhD thesis, University of Wisconsin-Madison, 1980.

[64] X. Ma, G.-S. Karamanos, and G.E. Karniadakis. Dynamics and low-dimensionality of the turbulent near-wake. *J. Fluid Mech.*, 410:29–65, 2000.

[65] M.V. Apostolakis, V.G. Mavrantzas, and A.N. Beris. Stress gradient-induced migration effects in the Taylor-Couette flow of a dilute polymer solution. *J. Non-Newtonian Fluid Mech.*, 102(2):409–445, 2002.

[66] G.E. Karniadakis and A. Beskok. *Microflows: Fundamentals and Simulation.* Springer, New York, 2001.

[67] S. Succi. *The Lattice Boltzmann Equation for Fluid Dynamics and Beyond.* Oxford University Press, 2001.

[68] P. Español and P. Warren. Statistical mechanics of dissipative particle dynamics. *Europhys. Lett.*, 30(4):191–196, 1995.

[69] A.G. Schlijper, P.J. Hoogerbrugge, and C.W. Manke. Computer simulation of dilute polymer solutions with the Dissipative Particle Dynamics method. *J. Rheol.*, 39(3):567, 1995.

[70] Xijun Fan, Nhan Phan-Thien, Ng Teng Yong, Xuhong Wu, and Diao Xu. Microchannel flow of a macromolecular suspension. *Phys. Fluids*, 15(1):11, 2003.

[71] R. D. Groot and P. B. Warren. Dissipative particle dynamics: Bridging the gap between atomistic and mesoscopic simulation. *J. Chem. Phys.*, 107(11):4423–4435, 1997.

[72] S. Chen, N. Phan-Thien, X.-J. Fan, and B.C. Khoo. Dissipative Particle Dynamics simulation of polymer drops in a periodic shear flow. *Journal of Non-Newtonian Fluid Mechanics*, 118:65–81, 2004.

[73] W.K. Den Otter and J.H.R. Clarke. Simulation of polymers by dissipative particle dynamics. In *Simulation Methods for Polymers, edited by M. J. Kotelyanskii and D. N. Theodorou.* Marcel Dekker, 2004.

[74] T. Shardlow. Splitting for dissipative particle dynamics. *SIAM J. Sci. Comput.*, 24(4):1267–1282, 2003.

[75] E.A.J.F. Peters. Elimination of time step effects in DPD. *Europhys. Lett.*, 66(3):311–317, 2004.

[76] P. Nikunen, M. Karttunen, and I. Vattulainen. How would you integrate the equations of motion in dissipative particle dynamic simulations? *Computer Physics Communications*, 153:407–423, 2003.

[77] Y. Kong, C. W. Manke, and W. G. Maddenand A. G. Schlijper. Effect of solvent quality on the conformation and relaxation of polymers via dissipative particle dynamics. *J. Chem. Phys.*, 107(2):592–602, 1997.

[78] Y. Kong, C. W. Manke, W. G. Madden, and A. G. Schlijper. Modeling the rheology of polymer solutions by dissipative particle dynamics. *Tribology Lett.*, 3:133–138, 1997.

[79] R. D. Groot, T. J. Madden, and D. J. Tildesley. On the role of hydrodynamic interactions in block copolymer microphase separation. *J. Chem. Phys.*, 110(19):9739–9749, 1999.

[80] B. I. M. ten Bosch. On an extension of dissipative particle dynamics for viscoelastic flow modelling. *J. Non-Newtonian Fluid Mech.*, 83:231–248, 1999.

[81] N. A. Spenley. Scaling laws for polymers in dissipative particle dynamics. *Europhys. Lett.*, 49(4):534–540, 2000.

[82] I. Vattulainen, M. Karttunen, G. Besold, and J. Polson. Testing the quality of integration schemes for Dissipative Particle Dynamics simulations: From softly interacting systems towards hybrid models. *J. Chem. Phys.*, 116:3967–3979, 2002.

[83] C. P. Lowe, A. F. Bakker, and M. W. Dreischor. The influence of time-dependent hydrodynamics on polymer centre-of-mass motion. *Europhys. Lett.*, 67(3):397–403, 2004.

[84] M.A. Horsch, Z-L Zhang, C.R. Iacovella, and S.C. Glotzer. Hydrodynamics and microphase ordering in blockcopolymers: Are hydrodynamics required for ordered phases with periodicity in more than one dimension? *J. Chem. Phys.*, 121(22):11455–11462, 2004.

[85] Li-Jun Chen, Zhong-Yuan Lu, Hu-Jun Qian, Ze-Sheng Li, and Chia-Chung Sun. The effects of Lowe-Andersen temperature controlling method on the polymer properties in mesoscopic simulations. *J. Chem. Phys.*, 122:104907, 2005.

[86] C. Pierleoni and J-P. Ryckaert. Molecular dynamics investigation of dynamic scaling for dilute polymer solutions in good solvent conditions. *J. Chem. Phys.*, 96(11):8539–8551, 1992.

[87] I. Pagonabarraga, M. H. J. Hagen, and D. Frenkel. Self-consistent dissipative particle dynamics algorithm. *Europhys. Lett.*, 42:377, 1998.

[88] W.K. den Otter and J.H.R. Clarke. The temperature in dissipative particle dynamics. *Europhys. Lett.*, 53:426–431, 2001.

[89] G.E. Karniadakis and S.J. Sherwin. *Spectral/hp Element Methods For Computational Fluid Dynamics.* Oxford University Press (2^{nd}*ed.*), 2005.

[90] B. M. Forrest and U. W. Suter. Accelerated equilibration of polymer melts by time-coarse-graining. *J. Chem. Phys.*, 102(18):7256–7266, 1995.

[91] R. D. Groot and K. L. Rabone. Mesoscopic simulation of cell membrane damage, morphology change and rupture by nonionic surfactants. *Biophys. J.*, 81:725–736, 2001.

[92] R. M. Jendrejack, J. J. de Pablo, and M. D. Graham. Stochastic simulations of DNA in flow: dynamics and the effects of hydrodynamic interactions. *J. Chem. Phys.*, 116:7752–7759, 2002.

[93] O. Kratky and G. Porod. Röntgenuntersuchung gelöster fadenmoleküle. *Rec. Trav. Chim.*, 68:1106–1115, 1949.

[94] H. Yamakawa. *Modern theory of polymer solutions.* Harper and Row, New York, 1971.

[95] S. F. Sun. *Physical chemistry of macromolecules.* John Wiley & sons, 1994.

[96] C. Bouchiat, M. D. Wang, J.-F. Allemand, T. Strick, S. M. Block, and V. Croquette. Estimating the persistence length of a worm-like-chain molecule from force-extension measurements. *Biophys. J.*, 76:409–413, 1999.

[97] R. G. Larson, T. T. Perkins, D. E. Smith, and S. Chu. Hydrodynamics of a DNA molecule in a flow field. *Phys. Rev. E*, 55(2):1794–1797, 1997.

[98] P. T. Underhill and P. S. Doyle. On the coarse-graining of polymers into bead-spring chains. *J. Non-Newtonian Fluid Mech.*, 122(1):3–31, 2004.

[99] L. Verlet. Computer 'experiments' on classical fluids. I: Thermodynamical properties of Lennard-Jones molecules. *Phys. Rev.*, 159:98–103, 1967.

[100] H. C. Andersen. Molecular dynamics simulations at constant pressure and/or temperature. *J. Chem. Phys.*, 72(4):2384–2396, 1980.

[101] M. P. Allen and D. J. Tildesley. *Computer Simulation of Liquids*. Oxford University Press, 1989.

[102] P.-G. de Gennes. *Scaling concepts in polymer physics*. Cornell University Press, 1979.

[103] W. C. Forsman. *Polymers in Solution: Theoretical considerations and newer methods of characterization,*. Plenum Press, New York, 1986.

[104] A. W. Lees and S. F. Edwards. The computer study of transport processes under extreme conditions. *J. Phys. C*, 5:1921, 1972.

[105] J.H. Irving and J.G. Kirkwood. The statistical mechanical theory of transport processes. IV. The equations of hydrodynamics. *J. Chem. Phys.*, 18:817–829, 1950.

[106] J. A. Backer, C. P. Lowe, H. C. J. Hoefsloot, and P. D. Iedema. Poiseuille flow to measure the viscosity of particle model fluids. *J. Chem. Phys.*, 122:154503, 2005.

[107] G.E. Karniadakis, A. Beskok, and N. Aluru. *Microflows and Nanoflows: Fundamentals and Simulation*. Springer, New York, 2005.

[108] C.A. Marsh. *Theoretical aspects of dissipative particle dynamics*. PhD thesis, University of Oxford, 1998.

[109] I. Pivkin and G.E. Karniadakis. A new method to impose no-slip boundary conditions in Dissipative Particle Dynamics. *J. Comp. Phys.*, 207(1):114–128, 2005.

[110] S. D. Stoyanov and R. D. Groot. From molecular dynamics to hydrodynamics: A novel Galilean invariant thermostat. *J. Chem. Phys.*, 122(11):114112, 2005.